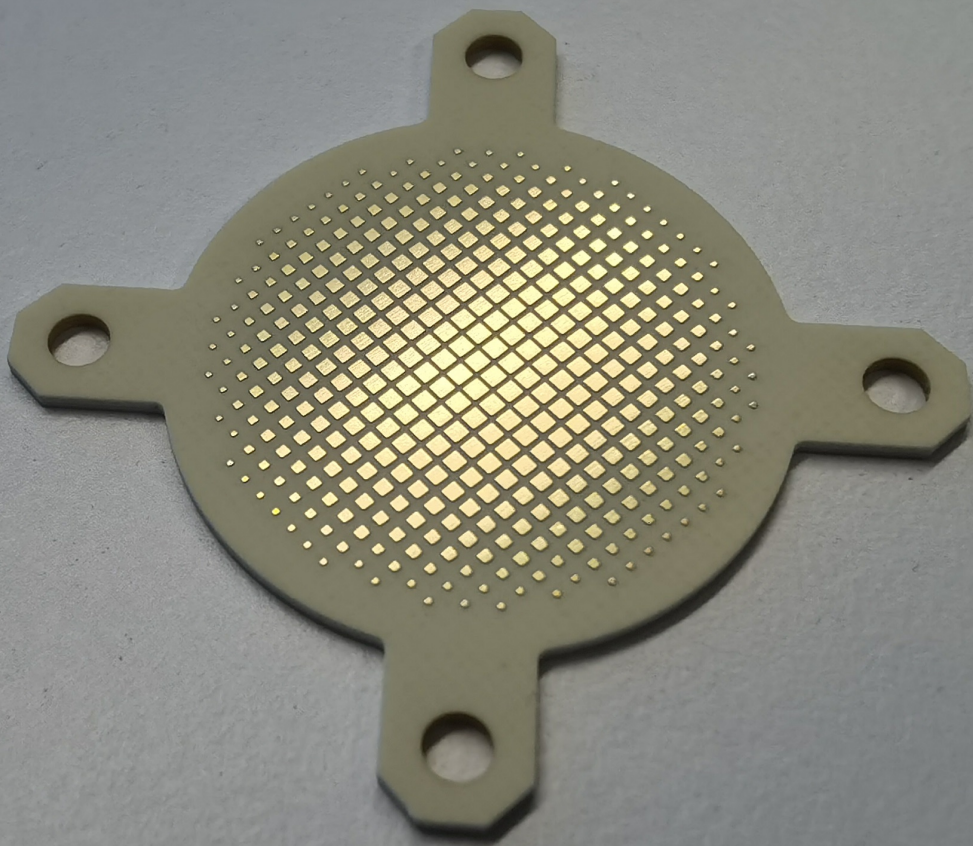


Artificial Dielectric Flat Lenses

Analysis, Design, Simulations & Measurements

Master Thesis - Electrical Engineering

Weiya Hu



Artificial Dielectric Flat Lenses

**Analysis, Design, Simulations and
Measurements**

by

Weiya Hu

Supervised by: dr. Daniele Cavallo
Caspar Coco Martin

to obtain the degree of Master of Science
at the Delft University of Technology,
to be defended publicly on Tuesday August 29, 2023 at 10:00 AM.

Student number: 5515599
Project duration: September 5, 2022 – August 29, 2023
Thesis committee: dr. Daniele Cavallo
Prof. dr. Andrea Neto
dr. Marco Spirito

An electronic version of this thesis is available at <http://repository.tudelft.nl/>.

Artificial Dielectric Flat Lenses: Analysis, Design, Simulations & Measurements.

Cover: Image of the metal layer board of the artificial dielectric flat lens prototype.

Copyright © 2023 Weiya Hu

All rights reserved.



Abstract

Flat lens antennas are convenient solutions to realize highly directive antennas for millimeter wave and terahertz frequencies. Unlike the traditional three-dimensional bulky lens antennas, flat lenses are compact, low profile, and planar structures that can be manufactured with standard multi-layer technology, e.g. printed circuit board (PCB) or low temperature cofired ceramic (LTCC).

A common tradeoff in the design of flat lenses is between bandwidth and thickness. Electrically thin lenses are characterized by narrow frequency bandwidth, resulting from the phase wrapping adopted in the design. On the other hand, a wide bandwidth can be achieved by avoiding phase wrapping and using true-time-delay phase delay, but this is achieved at the cost of increased electrical thickness.

In this thesis, artificial dielectric layers (ADLs), consisting of periodic metal patches within a dielectric substrate, are proposed to realize flat lenses with large effective refractive index, which is a key property for reducing the thickness of wideband true-time-delay flat lenses. As such, ADLs are promising solution to achieve a good compromise between bandwidth and thickness.

Different aspects of ADL flat lenses are investigated in this thesis, going from the analysis to the design and experimental validation. For the analysis, a general procedure to find the permittivity profile of a gradient index (GRIN) lens is introduced. The method allows to design GRIN lenses that manipulate the phase front in different ways, by using a Geometrical Optics (GO) approach. Different cases are studied, including collimating lenses with on-axis and off-axis feeds; lenses that transform spherical wavefronts across different media; lenses changing the focal number of a quasi-optical system and Fresnel zone lenses. The design equations are validated by ray-tracing simulations in non-homogeneous media, implemented by numerical solution of the Eikonal equation.

Once the permittivity profile is defined, the continuous variation of refractive index is discretized into unit cells. Each unit cell is then implemented as an ADL stack, using ADL synthesis models developed earlier in the THz sensing group.

To validate the design procedure, an ADL flat lens with an operation band from 30 to 60 GHz is designed and fabricated using an eight-layer print circuit board (PCB) stackup. The measurement results reach good agreements with the simulation results and validate the design. The achieved performance demonstrate wideband operation, with a high taper efficiency ($> 90\%$) and a maximum directivity of 25.5 dB. The lens is thinner than 1 wavelength within the band of operation.

The lens performance is demonstrated with a simple open-end waveguide as feed, which has high spillover losses. Diverse feeding antennas that can achieve higher aperture efficiency are also analysed by means of simulations.

Additionally, other types of GRIN lens, that manipulates the wavefront in distinct ways for different applications are investigate, to highlight the flexibility of the concept.

Acknowledgements

With this opportunity, I would like to express my sincere thanks to my supervisor dr. Daniele Cavallo. Thanks for the immense of time you have spent on me for helping me debug codes, check simulation results, and even review my thesis during your holiday. This thesis can never be finished without your insights, guidance, and patience. Thanks!

I am also deeply grateful to my daily supervisor, Caspar Coco Martin, for always being willing to help me no matter how busy you were. I really appreciate the knowledge and experience you shared, which have saved me a lot of time and effort. The discussions with you are always fruitful and the chats with you are always fun. I am so happy to have you as my daily supervisor.

I would also like to thank Prof. Andrea Neto for giving me the chance to build this flat lens prototype and for all the interesting stories you shared during lunch and coffee time. Moreover, thank you to all the other professors of the Terahertz Sensing group for the inspiring and lively lectures you gave. My special thanks go to dr. Juan Bueno for your kind help in the lab throughout the measurements.

I want to give my heartfelt thanks to all my colleagues. It is my honor to work with you. The past year wouldn't have been so fantastic to me without any of you. I will definitely cherish all the good moments shared with you. Once again, thank you!

Finally, my greatest gratitude goes to my family, especially my parents. Your unconditional love and continuous encouragement are the inexhaustible motivation that helps me overcome difficulties. The daily video calls with you are the best remedy for easing my tiredness. Thanks for everything you have done for me. This is for you.

胡偉亞

Weiya Hu
Delft, August 2023

DELFT UNIVERSITY OF TECHNOLOGY

ELECTRICAL ENGINEERING

MASTER THESIS

ARTIFICIAL DIELECTRIC FLAT LENSES
ANALYSIS, DESIGN, SIMULATIONS &
MEASUREMENTS

Weiya Hu

August 31, 2023

Terahertz Sensing Group
Department of Microelectronics
Faculty of Electrical Engineering Mathematics and Computer Science
Delft University of Technology

List of Figures

1.1	(a) Luneburg lens (Image credit: Wikipedia). (b) A flat lens example. . .	2
2.1	Geometry of the flat lens.	8
2.2	Geometry for the collimating lens case.	11
2.3	Result of ray-tracing simulation for lenses with different F/D ratios. . . .	12
2.4	(a) Relative permittivity distribution and (b) transmitted angle of three F/D lenses.	13
2.5	(a) Geometry of spherical wavefront lens; (b) definition of range for θ_{in} . .	15
2.6	Examples of lenses maintaining spherical wave across media.	15
2.7	Transmitted angle for feed shifting.	16
2.8	Ray tracing simulations for scanning lenses	17
2.9	Permittivity Distribution and θ_{out} of each lens	18
2.10	Example of GRIN lenses for transforming focal length.	19
2.11	Fresnel zone lens.	20
2.12	(a) Ray tracing simulations and (b) permittivity distribution for the example design.	21
3.1	(a) Reflection coefficients at center and edge of the lens, assuming the ideal materials are used. (b) The distribution of relative permittivity of core and inner matching layer. (c) The transmitted angle of the shrank lens. (d) The ray paths through the lens.	24
3.2	Realized effective permittivity of the ADL as a function of the gap width for different frequencies.	25
3.3	Cross section of (a) the center unit cell, (b) the last unit cell with metal, and (c) the entire lens.	25
3.4	(a) S_{11} for all unit cells and (b) phase variations of ADL synthesized lens and ideal GRIN lens.	26
3.5	Two different unit cell geometries for the outer matching layer.	28
3.6	CST models of the two considered perforated unit cells.	29
3.7	(a) Effective permittivity variation across the band. Effective permittivity versus perforation diameter of (b) aligned holes (c) shifted holes. . .	29
3.8	Prototype stack-up.	30
3.9	The schematic of (a) the core layer with metal, (b) the matching layer with perforations, and (c) the spacer between two multi-layer PCBs. . .	31

4.1	The simulation results of (a) the normalized patterns for three waveguides in the E- and H-planes (b) far field patterns in the E- and H-plane; (c) transmitted phase of the lens illuminated by WR22 at 45 GHz, where the lens aperture is shown as dashed line and (d) the calculated efficiencies across the band.	34
4.2	Comparison between two scan curves.	35
4.3	Simulated patterns for scanning in the E- and H-planes.	35
4.4	The 2D E-field for scanning to (a) 10° (b) 20° (c) 30°.	36
4.5	Prototype pictures of (a) the core layer with metal (b) the outer matching layer with perforations to achieve $\varepsilon_r = 2$ (c) the assembled prototype (the metal plate is for demonstration only, not the real size).	36
4.6	Measurement setup.	37
4.7	Two dimensional near field scan results for (a) Co-pol and (b) Cx-pol at 30 GHz.	38
4.8	Measured broadside patterns in comparison with simulated results at (a) 30 GHz (b) 40 GHz (c) 50 GHz (d) 60 GHz. The solid curves represents the measured results and dashed ones are for simulations.	39
4.9	Measured results for different scan angles and frequencies.	40
4.10	The comparisons of measured gains with typical values of (a) WR28 from 30 GHz to 40 GHz and (b) WR15 from 50 GHz to 60 GHz.	41
4.11	(a) The original measured transmitted phase, (b) the measured transmitted phase with misalignment correction at 60 GHz and (c) the directivity decreasing of 1° tilting simulations.	42
4.12	Measured and simulated directivity and gain.	43
4.13	(a) The primary patterns of the conical horn. (b) The secondary patterns of lens illuminated by the horn.	44
4.14	(a) Conical horn feed (b) 4 by 4 connected array.	45
4.15	(a) The primary patterns and (b) secondary patterns of E and H plane for lens illuminated by the 4x4 connected array	46
4.16	Efficiencies for the conical horn and 4x4 connected array, where the dashed curves represent η_{so} ; dotted curves stand for η_t ; solid curves refer to η_{ap}	47
5.1	(a) Geometry of original core-shell lens and (b) geometry of flat-core shell lens.	49
5.2	Ray tracing simulations for flat core lens of (a) initial design, (b) adjusted design and (c) design with the outer shell lens.	50
5.3	(a) Maximum relative permittivity realizable and (b) variation of permittivity across the band.	50
5.4	(a) GRIN lens core permittivity discretization and (b) cross-section of the ADL realized GRIN lens.	51
5.5	Reflection coefficients S_{11} of (a) the center unit cell and (b) all unit cells.	51
5.6	Flat core lens structure.	52
5.7	Pattern Comparisons.	53

5.8	(a) Far field patterns of flat core lens and (b) simulated E field at 155 GHz.	53
5.9	Flat core lens stackup design based on LTCC.	54
5.10	(a) A graphic illustration of Fresnel zone lens. (b) Phase variation on the lens with respect to incident angle.	55
5.11	Zone lens structure.	56
5.12	(a) Distribution of permittivity. (b) Ray tracing simulations.	56
5.13	The top view of the central row of metal patches for the (a) matching layer (b) non-shifted core layer (c) shifted core layer of the Fresnel zone lens.	57
5.14	(a) Phase distribution and (b) far-field pattern simulated at 7 THz with periodical boundary conditions.	57
6.1	(a) Cross section of the corrugated conical horn antenna. (Image credit: GrabCAD Community) (b) the 3D-printed double-ridges horn	60
A.1	Optical path inside the lens.	63
B.1	A small arc on the ray trajectory.	66
C.1	Layout of the GUI	68

List of Tables

1.1	Comparison of state of the art flat lens designs (λ is the wavelength at the highest frequency of operation).	4
3.1	Depolarization factors.	27
4.1	Open-ended waveguide used in simulations and measurements.	33
5.1	DuPont TM green tape TM 951 specifications.	54

Contents

Abstract	i
1 Introduction	1
1.1 Dielectric Lens Antenna	1
1.2 Gradient Index Lenses	2
1.3 Flat Gradient Index Lenses	2
1.3.1 Flat GRIN Lenses Design Approaches	3
1.4 Artificial Dielectric Layers	3
1.5 State of the Art of Flat GRIN Lens	4
1.6 Objective of the Thesis	5
1.7 Outline	5
2 GRIN Lens Design	7
2.1 Fermat's Principle	7
2.2 Lens Design Equations	8
2.2.1 Closed-form Expression for OPL Integration	9
2.3 Collimating Lens Design	10
2.3.1 Fixed n_{\max}	10
2.3.2 Fixed T	11
2.3.3 Examples of Collimating Lens Design	12
2.4 Spherical Wavefront	13
2.4.1 Examples of Lens Design	15
2.5 Other Scenarios	16
2.5.1 Scanning Lens	16
2.5.2 Focal Length Transformation	18
2.5.3 Fresnel Zone Lens	19
3 Flat Lens Prototype Design	22
3.1 Lens Geometry	22
3.2 Core Unit Cell Design	23
3.3 Matching Layer Design and Synthesis	24
3.3.1 Inner Matching Layer	25
3.3.2 Outer Matching Layer	26

3.4	Detailed Design	30
4	Prototype Simulations and Measurements	32
4.1	Full-Wave Simulations	32
4.1.1	Efficiencies	32
4.1.2	Open-Ended Waveguide Feeds	33
4.1.3	Broadside Simulated Performance	34
4.2	Prototype and Measurement	36
4.2.1	Measurement Setup	36
4.2.2	Radiation Pattern Measurement	37
4.3	Gain Measurement	40
4.3.1	Alignment	41
4.3.2	Limited Distance in the Setup	42
4.3.3	Metal Surface Roughness	43
4.3.4	Comparison Between Measurements and Simulations	43
4.4	Alternative Feeds	44
4.4.1	Conical Horn	44
4.4.2	4x4 Connected Array	45
5	Other GRIN Lens Designs	48
5.1	Flat Lens for 140-170 GHz Core-Shell Lens System	48
5.1.1	Lens Design	49
5.1.2	ADL Synthesis	50
5.1.3	Simulation Results	52
5.1.4	LTCC Realization	53
5.2	Flat Fresnel Zoned Lens at 7 THz	54
5.2.1	Lens Design	55
5.2.2	ADL Synthesis and Simulation Results	56
6	Conclusion and Future Work	58
6.1	Conclusion	58
6.2	Future Work	59
A	Steps for Finding Optical Path Integration	62
B	Derivation of the Eikonal Equation	65
B.1	Eikonal Equation from Wave Equation	65
B.2	Ray Equation from Eikonal Equation	66
C	Graphic User Interface for GRIN lens design and ray tracing simulation	68
	Bibliography	71

Chapter 1

Introduction

1.1 Dielectric Lens Antenna

The rapid evolution of wireless communication systems has attracted significant research efforts aimed at enhancing antenna performance to meet the ever-growing demand for higher data rates and improved signal quality. Dielectric lens antennas (DLAs) have gained remarkable attention due to their unique ability to provide enhanced gain, reduced side lobes, low-cost beamforming capabilities and efficient electromagnetic wave manipulation.

As wireless communication systems continue to evolve towards millimeter-wave (mm-Wave) and terahertz (THz) frequencies, DLAs have emerged as promising candidates for addressing the challenges posed by these higher frequency ranges. While lens antenna provides multiple advantages, there exist some disadvantages that limit the use of lens antennas from more applications:

- **Complexity of Manufacturing**

Since DLAs rely on their convex shape to delay the phase, they need to be accurately shaped to achieve the desired electromagnetic radiation. The tolerance of manufacturing such a curved surface become more crucial at higher frequency. This can significantly increase the fabrication costs and make the manufacturing process more complex. Especially challenging is the realization of matching layers, which are needed for achieving low reflection at the lens dielectric-air interface over large frequency bands.

- **Bulkiness and Size**

DLAs are generally bulky. The size of the lens is directly related to the operating wavelength, which means that lenses for lower frequency applications can become impractically large. Even if at mmWave and THz frequencies, although the dimension of the lens become relatively small, a few centimeters in height can still be quite large for highly integrated and compact sensors.

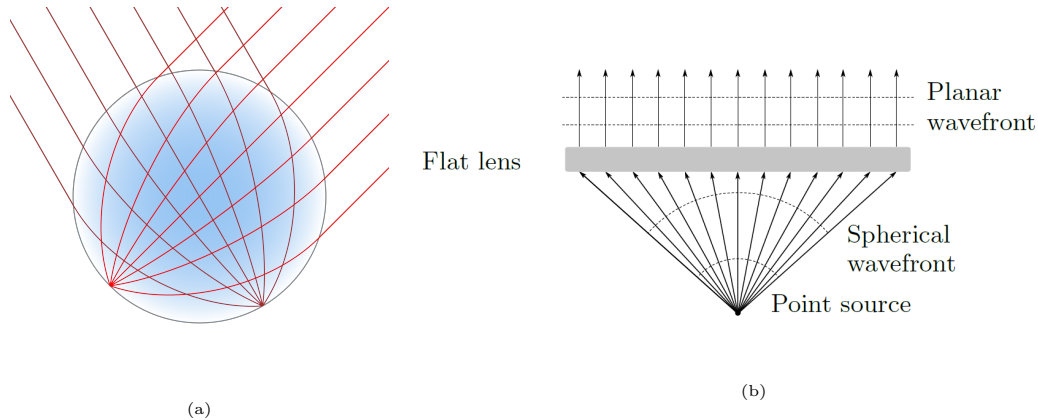


Figure 1.1: (a) Luneburg lens (Image credit: Wikipedia). (b) A flat lens example.

1.2 Gradient Index Lenses

A Gradient Index (GRIN) lens, characterized by its spatially varying refractive index profile, manipulates the wavefront not only by means of its geometrical properties but also by exploiting the spatially varying refractive index. Unlike the conventional DLAs, which relies on the curved surface to manipulate the wave, the varying refractive index can bend electromagnetic rays with far greater control [1]. One of the most common GRIN lens is the Luneburg lens [2]. The refractive index n follows the profile law

$$n = \sqrt{2 - \frac{\rho^2}{R^2}}, \quad (1.1)$$

where ρ is the radial distance from the lens center and R is the radius of the sphere. With such a distribution, the refractive index decreases radially from the center to the outer shell. As a result, electromagnetic rays emanating from any point source located on the outer surface of the lens are bent within the lens to exit with a planar wavefront at the opposite end. By duality, parallel rays impinging on the lens are focused in a point at the opposite side of the lens. There is no reflection on the lens boundary as the permittivity on the surface is the same as the surrounding one.

Many other examples of GRIN lenses exist besides the Luneburg lens. Since both the geometrical shape and the refractive index play roles in controlling the wave propagation, more compact and low profile lenses can also be realized.

1.3 Flat Gradient Index Lenses

One type of GRIN lenses is represented by flat lenses (see Fig. 1.1b). Flat lenses are low profile and can be fabricated more easily compared to curved lenses, making them desirable at mmWave frequencies.

Planar multi-beam thin lens antennas can be realized as transmitarrays [3], metasurfaces [4], or Fresnel lenses [5]. However, one of the limitations of these solutions is

the narrow frequency bandwidth, due to the phase wrapping along the aperture, which results in sudden discontinuous jumps in the phase distribution. To overcome this limitation, true-time-delay (TTD) lenses can be used that provide wideband behavior. One example is the GRIN lens consisting of a dielectric cylinder with a radial gradient of the refractive index [6]. GRIN lenses are characterized by reflection losses varying across the lens and large electrical thickness. However, matching layers can be employed to improve the transmission at the lens-air interface [7]. Moreover, to reduce the thickness of GRIN lenses one can resort to high permittivity dielectrics [8].

A convenient way to realize high permittivity materials, with refractive indexes that can be much larger than the ones of commercially available dielectrics, is based on artificial dielectric layers (ADLs) [9]. These can be realized with a cascade of periodic arrays composed of sub-wavelength patches (capacitive gratings) to boost the effective permittivity by providing increased phase shift for a plane wave propagating within the artificial medium. TTD lens designs based on such periodic structures with sub-wavelength elements were presented in [10].

1.3.1 Flat GRIN Lenses Design Approaches

Generally, there are different approaches to design GRIN lenses. A common method is based on transformation optics (TO). TO is a systematic and well-established method that consists of a coordinate systems transformations of Maxwell's equations [11, 12]. In order to design a lens with certain properties, a specific coordinate transformation is applied that results in a corresponding map of the permittivity and permeability tensors [13].

Another approach was proposed in [14] and uses Field Transformation (FT). This method is based on a discretization of the lens into unit cells, each with a certain unknown permittivity ϵ . The permittivity in each region can be found with a synthesis procedure that converts a given input field distribution into a desired output field distribution exiting the lens. An equivalent cascade transmission line model can be used for finding the correct parameters to have a desired output phase distribution and high transmission.

An alternative approach for designing GRIN lenses is to match the path length of the wave propagating through different segments of the lens [6, 8, 15]. A closed form expression of the optical path through the lens was given in [15] and a generalization of this method to more general cases will be used in this thesis.

1.4 Artificial Dielectric Layers

One of the fundamental tradeoffs in GRIN lenses design is between thickness and bandwidth. Thin lenses are convenient in terms of cost and complexity, but typically provide narrow bandwidths of operation. On the other hand, wideband lenses are bulky and not easy to integrate with the electronic front-end for mm-wave and terahertz frequency applications. In this thesis we suggest that artificial dielectric layers (ADLs) can provide a good tradeoff between bandwidth and compactness, by providing true-time-delay phase

shifts (wideband) while keeping the thickness small and thus suitable for integrated front-ends.

Artificial dielectrics (AD) were introduced in [16]. They have emerged as promising engineered materials for offering unique electromagnetic properties, such as a significantly increased dielectric permittivity, that cannot be found in natural dielectric materials.

A specific type of artificial dielectric that lends itself to multi-layer implementation, consists of cascade structures of planar metal layers. This structure is also referred to as artificial dielectric layers (ADLs). The metal layers are composed by periodic sub-wavelength patches.

The closed-form expressions for the capacitance and impedance of a single layer and each layer in a multi-layer structure are firstly given in [17, 18]. It is found in [19] that the maximum refractive index achievable can be increased by introducing the inter layer shifting, which means the total thickness of the ADL structure can be decreased while keeping the performance unchanged. These expressions are derived with the higher order Floquet-mode interactions between layers into considerations. In [20], the analysis on ADLs is further extended to non-periodic layers. These expressions can be used to find the effective permittivity of a certain ADL structure by equating the ABCD matrix of the ADLs with the one of an equivalent material [21] with a relative permittivity $\varepsilon_{r,\text{eff}}$.

1.5 State of the Art of Flat GRIN Lens

In this section we report and compare several results of the recently proposed GRIN lenses realized using ADs. The comparisons on the geometry parameters and other specifications are shown in Table 1.1. It can be noticed that aperture efficiencies lower than 60% are typically obtained for the existing designs, and the efficiency decreases for small F/D ratios.

Author	[22]	[23]	[24]	[25]	[26]
Diameter	4.3λ	3.8λ	3.8λ	0.73λ	6.3λ
Thickness	0.6λ	0.55λ	0.4λ	0.87λ	0.53λ
F/D	0.28	~ 0.5	0.5	0.2	0.7
Bandwidth (GHz)	7-13	8-12	7-13	8-10	7-13.2
Cx-pol	< -17.1 dB	< -15 dB	< -15 dB	\sim	< -26 dB
Scanning ($^\circ$)	$\pm 32/\pm 35$	± 34	\sim	± 45	\sim
Aperture efficiency	46.2%	63%	\sim	23%	51%

Table 1.1: Comparison of state of the art flat lens designs (λ is the wavelength at the highest frequency of operation).

1.6 Objective of the Thesis

The objective of this thesis is to propose a general procedure to design artificial dielectric flat lenses. The artificial dielectrics represent a good compromise between bandwidth and thickness, allowing for wide bandwidth behaviour, while reducing the overall thickness of the lens for suitable manufacturing at mm-wave and terahertz frequencies.

The presented approach combines several techniques:

- Closed-form expressions are derived to define the refractive index distribution of the lens, for several cases: collimating lenses with on-axis feed, collimating lenses with off-axis feed, lenses converting spherical wavefronts with different wavenumbers, lenses changing the focal number of a quasi-optical systems, Fresnel zone lenses.
- Once the ideal distribution of refractive index is determined, multiple matching layers are included to ensure low reflection over wide frequency band. A numerical ray tracing tool is implemented, to validate the design obtained from the closed-form expressions and to readjust the performance once the matching layers are included. This ray tracing has been also implemented in the form of a Matlab tool with a graphical user interface.
- From the continuous distribution of refractive index of the core lens and the matching layers, a synthesis procedure is applied to implement the desired permittivity with artificial dielectric layers (ADLs). ADLs are an arrangement of sub-wavelength metal patches placed within a host medium.
- Finally, CST simulations of the resulting ADL lens are performed as additional check of the entire procedure.

Based on the proposed method, several designs are made for different applications. For one of this design, a prototype was also developed and measured. This consists of a flat lens with an operation bandwidth from 30 to 60 GHz and directivity ranging from 20 to 25 dB. The measured results showed good agreement with the simulated predictions.

1.7 Outline

This thesis consists of five main chapters:

- In Chapter 2, the general equations for finding the permittivity profile of a flat GRIN lens are reported. The implementation of these equations are validated by performing the ray-tracing simulations. Example designs are given for each scenario.
- Chapter 3 describes the procedure of designing a wideband flat collimating lens prototype. The design for the core layer and matching layer (ML) are discussed. The procedure for synthesizing the varying permittivity across the aperture with ADLs is explained, with the unit cell design being shown.

- Chapter 4 shows the full wave simulation and measurement results of the prototype. The scanning performance is also evaluated. Both results are analyzed and compared. Several types of feeds are simulated with the prototype.
- Two other GRIN lenses are investigated in chapter 5. A flat lens for a core-shell lens system is designed. Furthermore, a Fresnel zone lens at 7 THz is investigated and designed. These designs are validated by both the ray tracing and full wave simulations.
- Chapter 6 concludes this thesis by summarizing the work and giving suggestions for further study.

Chapter 2

GRIN Lens Design

2.1 Fermat's Principle

In optics, Fermat's Principle is a statement that relates the path of light to the time it takes to travel. Fermat's Principle for electromagnetic waves is a generalization of Fermat's Principle for light. It states that the path taken by an electromagnetic (EM) wave, i.e. the optical path, between two points P_1 and P_2 is the one that minimizes the time of travel. The optical path length (OPL) is the integral of the local refractive index $n(s)$ along the optical path:

$$\text{OPL} = \int_{P_1}^{P_2} n(s) ds, \quad (2.1)$$

where s indicates a generic point along the path. This parameter determines the phase difference as the wave propagates through different media. The refractive index of an isotropic material equals:

$$n = \sqrt{\varepsilon_r \cdot \mu_r} \quad (2.2)$$

where ε_r is the relative permittivity of the material, and μ_r refers to its relative permeability [27]. In the following parts, we assume all the materials under consideration are non-magnetic, which means the relative permeability equals 1. Therefore, the refractive index n is simplified as:

$$n = \sqrt{\varepsilon_r}. \quad (2.3)$$

When an electromagnetic wave travels a specific optical path length, it reaches its destination with a phase shift that depends on the various media it passes through. The corresponding phase variation along the integration path is given by:

$$\Delta\phi = \frac{2\pi}{\lambda_0} \cdot \text{OPL}. \quad (2.4)$$

where λ_0 is the wavelength in free space.

2.2 Lens Design Equations

The relative permittivity of a GRIN lens that reshapes the wavefront in different ways should change as a function of position to compensate for the phase difference accordingly. From (2.4), the phase variations across the lens depend on the optical path length only at a given frequency.

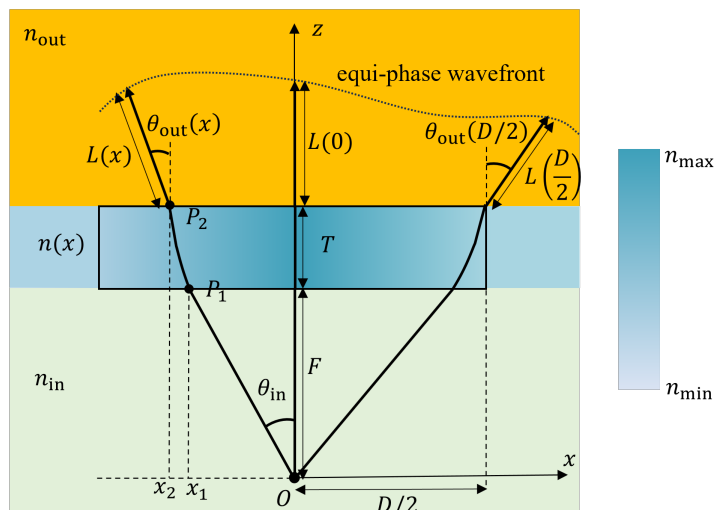


Figure 2.1: Geometry of the flat lens.

Considering a general scenario shown in Fig. 2.1, the lens with a diameter of D is illuminated by a point source placed at the focal point, with F as the focal distance. The media below and above the lens have refractive indexes n_{in} and n_{out} , respectively. The permittivity distribution inside the lens is simplified to vary only in the radial direction, i.e. the refractive index for a two dimensional cross section of the lens (xz -plane) is only function of x and is constant with z inside the lens. An arbitrary ray with an incident angle θ_{in} transmits through the lens from $P_1(x)$ to $P_2(x)$ and propagates into the upper medium with transmitted angle θ_{out} . We assume that the distance between a generic point $P_2(x)$, where the ray exits the lens, and a desired equi-phase surface is denoted as $L(x)$. The phase variations from the feed to this equi-phase wavefront for each ray should be equal to the one of the ray passing through the lens' center:

$$n_{\text{in}}F + n_{\text{max}}T + n_{\text{out}}L(0) = n_{\text{in}}\frac{F}{\cos\theta_{\text{in}}} + \int_{P_1}^{P_2} n ds + n_{\text{out}}L(x). \quad (2.5)$$

A typical way to solve (2.5) requires imposing a condition for the edge of the lens, e.g. $L(D/2) = 0$ (the equi-phase front passes through the top edge of the lens) and $n(D/2) = n_{\text{min}}$, which allows to solve for unknowns such as the thickness of the lens T or the maximum refractive index n_{max} .

2.2.1 Closed-form Expression for OPL Integration

Closing the integral $\int_{P_1}^{P_2} nds$ is required for solving (2.5). The derivations are based on [15] and are described in detail in Appendix. A. In this section we report the final expressions and the main assumptions used for the solution.

The first hypothesis to simplify the problem consists of assuming that the variation of permittivity (from ε_{r1} to ε_{r2}) is linear within the region from x_1 to x_2 with a slope a ($a > 0$) where x_1 and x_2 are the x -coordinates of the points P_1 and P_2 . Thus, for a point x in the range $[x_1, x_2]$, characterized by relative permittivity ε_r , one can write:

$$\varepsilon_r - \varepsilon_{r2} = a(x_2 - x) \quad (2.6)$$

where a can be expressed as:

$$a = \frac{\varepsilon_{r1} - \varepsilon_{r2}}{x_2 - x_1}. \quad (2.7)$$

This assumption allows deriving a closed-form expression for the optical path integral that can be found as follows:

$$\int_{P_1}^{P_2} nds = T \frac{(S_{\text{in}}^3/3 + 2S_{\text{out}}^3/3 + (\varepsilon_{r2} - S_{\text{out}}^2)S_{\text{in}} - \varepsilon_{r2}S_{\text{out}})}{\sqrt{\varepsilon_{r2} - S_{\text{out}}^2}(S_{\text{in}} - S_{\text{out}})} \quad (2.8)$$

where $S_{\text{in}} = n_{\text{in}} \sin \theta_{\text{in}}$, $S_{\text{out}} = n_{\text{out}} \sin \theta_{\text{out}}$, T is the thickness of the GRIN lens and ε_{r2} refers to the relative permittivity at position x_2 , i.e. $\varepsilon_{r2} = \varepsilon_r(x_2)$. (2.8) can be also written in a dual form, as a function of the permittivity and the input point of the ray at the bottom of the lens $\varepsilon_{r1} = \varepsilon_r(x_1)$:

$$\int_{P_1}^{P_2} nds = T \frac{(-2S_{\text{in}}^3/3 - S_{\text{out}}^3/3 - (\varepsilon_{r1} - S_{\text{in}}^2)S_{\text{out}} + \varepsilon_{r1}S_{\text{in}})}{\sqrt{\varepsilon_{r1} - S_{\text{in}}^2}(S_{\text{in}} - S_{\text{out}})}. \quad (2.9)$$

One can note that the solution depends on both S_{in} and S_{out} , which in turns are functions of θ_{in} and θ_{out} . Therefore, the design of the GRIN lens varies for different transmitted wavefront scenarios, which correspond to different θ_{out} . The expressions for the variation slope a can be related to thickness as well, using either of the following two forms:

$$a = \frac{2\sqrt{\varepsilon_{r2} - S_{\text{out}}^2}(S_{\text{in}} - S_{\text{out}})}{T} \quad (2.10a)$$

$$a = \frac{2\sqrt{\varepsilon_{r1} - S_{\text{in}}^2}(S_{\text{in}} - S_{\text{out}})}{T}. \quad (2.10b)$$

The general formulas reported here are applied in the following sections to specific lens configurations.

2.3 Collimating Lens Design

The simplest scenario is the collimating lens, where the spherical wave emanating from the feed is converted into a planar wave exiting the lens. The extra path term $L(x)$ on both sides of (2.5) vanishes, because the wave has the same phase everywhere when reaching the exit plane $z = T$. All transmitted angles θ_{out} are equal to 0. This simplifies (2.8) and (2.9) into:

$$\int_{P_1}^{P_2} nds = T \frac{S_{\text{in}}^2 + \varepsilon_{r2}}{\sqrt{\varepsilon_{r2}}} \quad (2.11a)$$

$$\int_{P_1}^{P_2} nds = T \frac{(-2\frac{S_{\text{in}}^2}{3} + \varepsilon_{r1})}{\sqrt{\varepsilon_{r1} - S_{\text{in}}^2}}. \quad (2.11b)$$

It can be observed that (2.11a) and (2.11b) depend on the thickness of lens T , the incident angle θ_{in} , and the relative permittivity $\varepsilon_{r1/2}$ at positions where the ray enters and exits the lens $x_{1/2}$. (2.5) can be rewritten as:

$$n_{\text{in}}F + n_{\text{max}}T = n_{\text{in}} \frac{F}{\cos \theta_{\text{in}}} + \int_{P_1}^{P_2} nds \quad (2.12)$$

where the integral is defined from (2.11a) or (2.11b) as a function of θ_{in} and $\varepsilon_{r1/2}$. To find the distribution of permittivity, we need to solve (2.12). In this equation, θ_{in} is known in each point and given by $\tan^{-1}(x_1/F)$, while $\varepsilon_{r1/2}$ are dependent variables. Therefore, the two unknowns of (2.12) are n_{max} and T . There are two possible options to design the lens, by either fixing n_{max} and finding T , or fixing T and finding the correspondent n_{max} . For example, in some designs one could opt to fix the thickness of the lens to a constrained value, resulting in a specific value of the maximum refractive index. Alternatively, one could constrain the n_{max} , e.g. by the specific technology used to realize the artificial dielectric, which results in a certain thickness.

2.3.1 Fixed n_{max}

With n_{max} as a given value, we apply (2.12) to the ray that crosses the lens edge, corresponding to the maximum incident angle $\theta_{\text{in,max}} = \tan^{-1}[D/(2F)]$ and to the minimum permittivity $\varepsilon_{r,\text{min}}$:

$$n_{\text{in}}F + n_{\text{max}}T = n_{\text{in}} \frac{F}{\cos \theta_{\text{in}}} + T \frac{(-2S_{\text{in,max}}^2/3 + \varepsilon_{r,\text{min}})}{\sqrt{\varepsilon_{r,\text{min}} - S_{\text{in,max}}^2}} \quad (2.13)$$

where $S_{\text{in,max}} = n_{\text{in}} \sin \theta_{\text{in,max}}$. The thickness of the lens can be found by inverting (2.13), resulting in:

$$T = \frac{n_{\text{in}}F \left(\frac{1}{\cos \theta_{\text{in,max}}} - 1 \right)}{n_{\text{max}} - \frac{3\varepsilon_{r,\text{min}} - 2S_{\text{in,max}}^2}{3\sqrt{\varepsilon_{r,\text{min}} - S_{\text{in,max}}^2}}}. \quad (2.14)$$

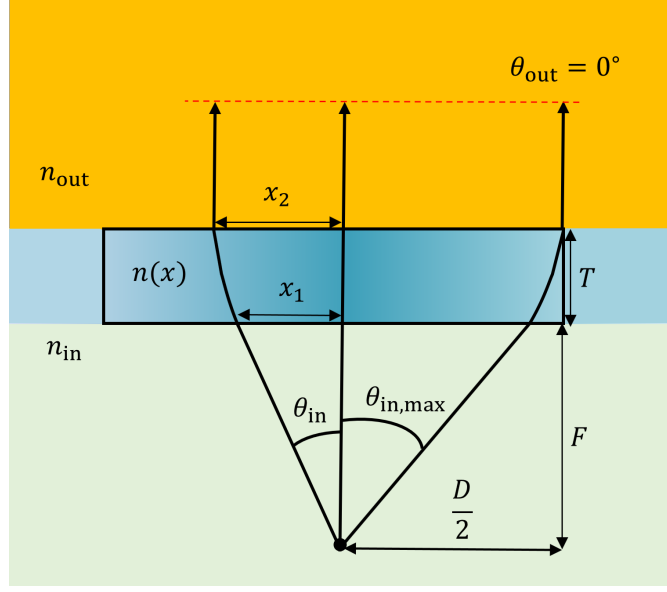


Figure 2.2: Geometry for the collimating lens case.

Once the value of T is found, one can again apply (2.12) to find all the values of $\varepsilon_{r1}(x)$ in any generic lens position x .

2.3.2 Fixed T

In the previous subsection, the edge ray identified with the incident angle $\theta_{\text{in,max}}$ is intersecting the lens bottom surface at the edge $x_1 = D/2$. This ray is not bent as it propagates outside the lens. It is then convenient to consider as the last ray, the one exiting the lens at $x_2 = D/2$, rather than entering at the same x -position. Imposing the edge ray to exit at $x_2 = D/2$ typically improves the collimating performance of the lens at the edges. This assumption could not be used in the fixed n_{max} approach, because it would result in too many unknowns in equation (2.13). In the current approach, where the thickness is fixed, we can instead solve the problem assuming $x_2 = D/2$. However, with this assumption, $\theta_{\text{in,max}}$ becomes an unknown.

For a ray exiting the lens at the upper edge ($x_2 = D/2$), as shown in Fig. 2.2, x_1 and x_2 are given by:

$$x_1 = F \cdot \tan \theta_{\text{in,max}}, \quad x_2 = \frac{D}{2} \quad (2.15)$$

From (2.7) and by applying several conditions, such as Snell's law at x_1 and x_2 , the radial distance between the input and the output points for an arbitrary ray is:

$$x_2 - x_1 = \frac{S_{\text{in}}^2 - S_{\text{out}}^2}{a}. \quad (2.16)$$

(2.10a) becomes:

$$\frac{D}{2} - F \cdot \tan \theta_{\text{in,max}} = \frac{T \cdot S_{\text{in,max}}}{2\sqrt{\varepsilon_{r,\text{min}}}}. \quad (2.17)$$

This equation can be solved by rewriting it as a 4-th order equation of the variable $Q = \sin \theta_{\text{in,max}}$:

$$-\frac{B^2}{4}Q^4 + ABQ^3 + \left(\frac{B^2}{4} - A^2 - F^2\right)Q^2 - ABQ + A^2 = 0 \quad (2.18)$$

where $A = \frac{D}{2}$, $B = \frac{T}{\sqrt{\varepsilon_{r,\text{min}}}}$. By solving this quartic equation and discarding those nonphysical roots (imposing that $\theta_{\text{in,max}}$ is a real angle), the incident angle of the last ray can be found, and therefore the total optical path length through the lens edge can be accurately described. The refractive index at the center n_{max} can be then calculated based on (2.12) by substituting ε_{r2} with $\varepsilon_{r,\text{min}}$ and θ_{in} with $\theta_{\text{in,max}}$ as the root of the quartic equation.

With the two cases discussed above, both n_{max} and T become known values whichever one is given. Thus far, accurate descriptions of the OPL of the centre and edge paths are attained. For any other positions on the lens, the permittivity can be solved by combining (2.11b) and (2.12) with $\theta_{\text{in}} = \tan^{-1}(x/F)$:

$$n_{\text{in}}F + n_{\text{max}}T = n_{\text{in}}\frac{F}{\cos \theta_{\text{in}}} + T\frac{3\varepsilon_{r1} - 2S_{\text{in}}^2}{3\sqrt{\varepsilon_{r1} - S_{\text{in}}^2}}. \quad (2.19)$$

2.3.3 Examples of Collimating Lens Design

The method is validated by applying ray-tracing simulations on the designed lens. The steps for ray-tracing simulation within the non-homogeneous medium are introduced in [28].

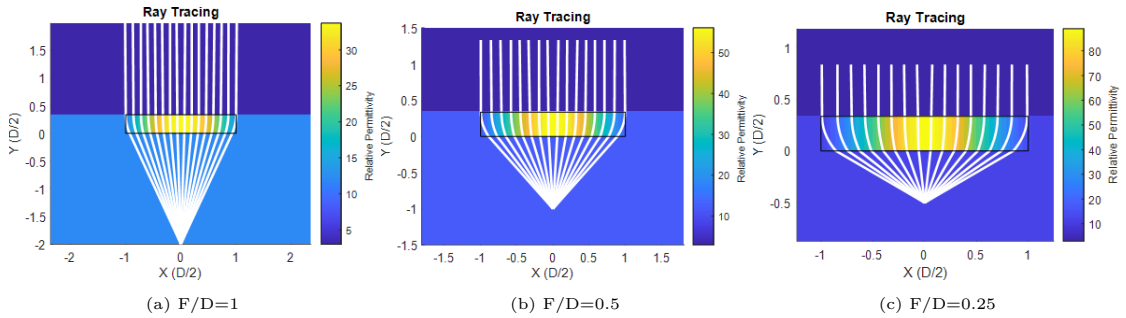


Figure 2.3: Result of ray-tracing simulation for lenses with different F/D ratios.

With the design equations, considering $\varepsilon_{r,\text{min}} = \varepsilon_{r,\text{in}} = 12$, $\varepsilon_{r,\text{out}} = 3$, $D = 3 \text{ mm}$, $T = 0.17D$, 3 lenses with different F/D ratios were obtained. Fig. 2.3 shows the ray paths through these lenses computed using the ray-tracing simulations. The output rays are

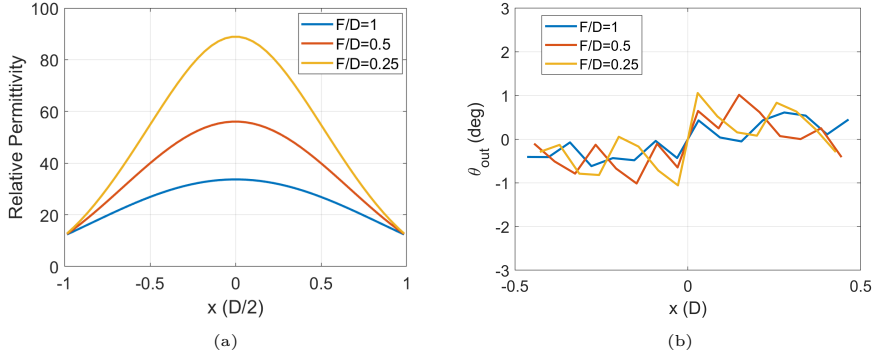


Figure 2.4: (a) Relative permittivity distribution and (b) transmitted angle of three F/D lenses.

nearly parallel and vertical, thus validating the proposed method. Fig. 2.4a shows the distribution of the relative permittivity for the three F/D ratios, while Fig. 2.4b presents the values of the transmitted angle for each ray. All considered examples exhibit variations within $\pm 1^\circ$, computed with numerical ray-tracing method using MATLAB's built-in `ode45()` function to solve the system of ordinary differential equations in (B.14) and (B.15).

2.4 Spherical Wavefront

In some cases, one can design the lens such that the output wavefront is not planar but still spherical, but with a different radius of curvature or wavenumber. Some examples of applications for this scenario will be discussed in Chapter 5, referring to double lens systems.

In this case, the lens is located between two different media and is designed so that the spherical wavefront is maintained across the two media as if there was no medium discontinuity. In other words, the transmitted rays should appear as if they were emanating as straight rays from the same focal point (see Fig. 2.5a).

Since a spherical wavefront is desired on top of the lens, the function $L(x)$ is not zero across the lens. If a spherical wavefront intersecting the lens upper edge is considered, i.e. $L(D/2) = 0$, then $L(x)$ can be expressed as:

$$L(x) = \frac{F + T}{\cos \theta_{\text{out,max}}} - \frac{F + T}{\cos \theta_{\text{out}}} \quad (2.20)$$

where $\theta_{\text{out,max}}$ is defined as in Fig. 2.5a, to be equal to

$$\theta_{\text{out,max}} = \tan^{-1} \left(\frac{D}{2(F + T)} \right). \quad (2.21)$$

Unlike the collimating case, the transmitted angle varies for each position and is an additional unknown of the problem, making the solution more complicate. Therefore, the mapping between each pair of $\theta_{\text{in}}, \theta_{\text{out}}$ must be found to solve (2.5).

For the sake of simplicity, we only consider here the simpler case where the lens thickness T is fixed while n_{\max} is left unknown. Similar to the steps described in the collimating case, as shown in Fig. 2.5a:

$$x_1 = F \tan \theta_{\text{in,max}}, \quad x_2 = (F + T) \tan \theta_{\text{out}}. \quad (2.22)$$

(2.16) for spherical wavefront can be still expressed in the form given in (2.18), but with different values of A and B :

$$A = (F + T) \tan \theta_{\text{out}} - T \frac{S_{\text{out}}}{2\sqrt{\varepsilon_{r,\min}} - S_{\text{out}}^2}; \quad B = T \frac{n_{\text{in}}}{\sqrt{\varepsilon_{r,\min}} - S_{\text{out}}^2}. \quad (2.23a)$$

By replacing $\theta_{\text{in}}, \theta_{\text{out}}, \varepsilon_{r2}$ with $\theta_{\text{in,max}}, \theta_{\text{out,max}}, \varepsilon_{r,\min}$ into the (2.5), n_{\max} can be written as:

$$n_{\max} = \frac{1}{T} \left(\frac{n_{\text{in}} F}{\cos \theta_{\text{in,max}}} - n_{\text{out}} \left(\frac{F + T}{\cos \theta_{\text{out,max}}} - F - T \right) - n_{\text{in}} F + \int_{P_1}^{P_2} n ds \right). \quad (2.24)$$

With n_{\max} known, to find the relative permittivity at any position on the lens with respect to each θ_{out} , the first step is to rewrite ε_{r2} in (2.16) as a function of incident angle θ_{in} :

$$\varepsilon_{r2}(\theta_{\text{in}}) = S_{\text{out}}^2 + \frac{1}{4} \left[\frac{T(S_{\text{in}} + S_{\text{out}})}{(F + T) \tan \theta_{\text{out}} - F \tan \theta_{\text{in}}} \right]^2. \quad (2.25)$$

Unlike the collimating case, where $\theta_{\text{out}} = 0$ everywhere, θ_{out} is now a function that depends on radial distance. In order to have the ray refocus on the focal point, the transmitted angle for the ray exiting lens at x is given by:

$$\theta_{\text{out}} = \tan^{-1} \left(\frac{x}{F + T} \right). \quad (2.26)$$

Because we are imposing θ_{out} to be given, the angle θ_{in} is not known. For every given θ_{out} , the OPL equation varies with θ_{in} only. Therefore, the certain θ_{in} that makes (2.5) valid is the incident angle of the ray which exits the lens at θ_{out} . This θ_{in} can be calculated by finding numerically the value that minimizes the difference between the left and right hand side of OPL. From the geometry shown in Fig. 2.5b, for a given θ_{out} , a single value of θ_{in} can be found when limiting the search in the range $(\theta_{\text{out}}, \theta')$, where $\theta' = \tan^{-1}(x_2/F)$. In this way, the mapping of θ_{in} and θ_{out} is found, and therefore ε_{r2} can be determined by substituting $(\theta_{\text{in}}, \theta_{\text{out}})$ into (2.25).

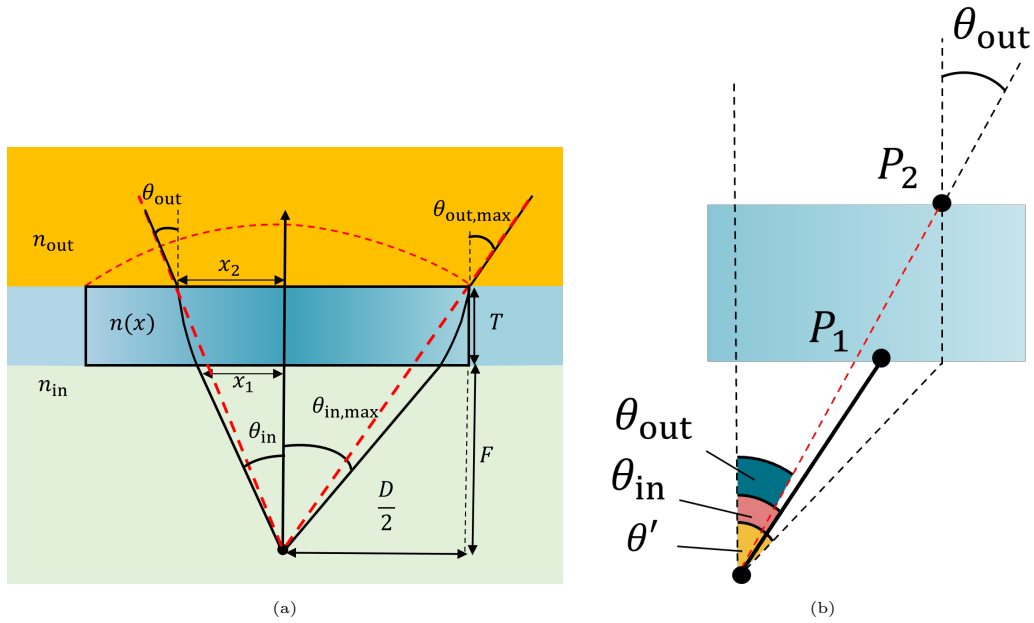


Figure 2.5: (a) Geometry of spherical wavefront lens; (b) definition of range for θ_{in} .

2.4.1 Examples of Lens Design

Two lenses with different F/D ratio are designed. Both lenses radiate from silicon ($\epsilon_r = 12$) to plastic ($\epsilon_r = 3$) and have $\epsilon_{r,min} = 12$. The thickness of both lenses is $0.2D$.

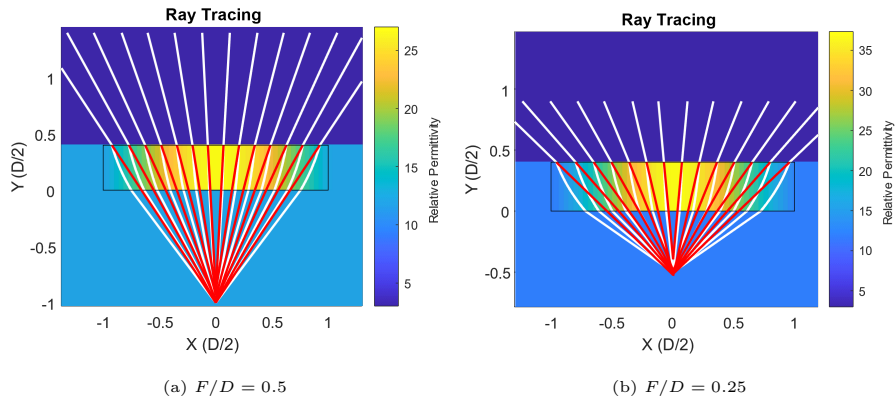


Figure 2.6: Examples of lenses maintaining spherical wave across media.

In Fig. 2.6, the white curves indicate the forward paths wave propagation, while the red curves are the reverse extensions from the transmitted rays. It can be noticed that most of the red curves converge in the focal point, which is the goal of this design.

2.5 Other Scenarios

With the equations reported in the previous sections, applications other than collimating and spherical wavefront can be considered. Here, we report the design methods for three different types of lenses: scanning lens, focal length transformation lens and Fresnel zone lens.

2.5.1 Scanning Lens

Conventionally, it is possible to tilt the main beam of a dielectric lens by shifting the feed. In Fig. 2.7, the results of θ_{out} for the collimating lens with various feed shift are shown.

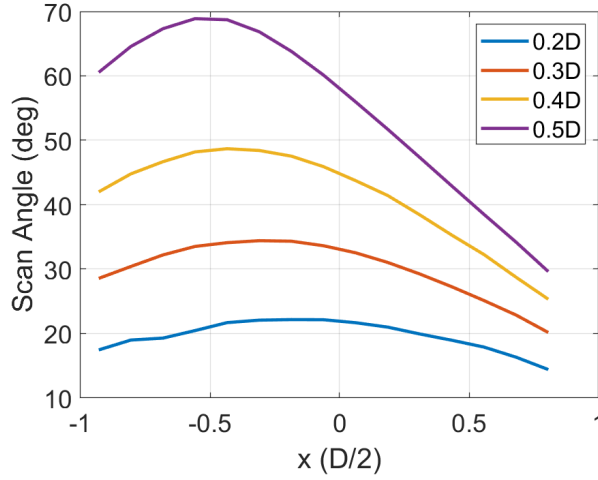


Figure 2.7: Transmitted angle for feed shifting.

It can be noticed that, with the permittivity distribution optimized for broadside maximum radiation, the GRIN lens scanning performance is quite limited, and the phase and the direction of the transmitted rays undergo larger aberrations as the feed is shifted farther from the center. Nevertheless, a flat lens that transforms the spherical beam into a planar beam pointing at θ_{scan} can be realized. For the scanning GRIN lens, $\theta_{\text{out}} = \theta_{\text{scan}}$ is valid across the lens. The OPL for an arbitrary position is given by:

$$n_{\text{in}} \sqrt{x_1^2 + F^2} + \int_{P_1}^{P_2} n ds + n_{\text{out}} \left(\frac{D}{2} - x_2 \right) \sin \theta_{\text{scan}}. \quad (2.27)$$

The OPL along the edge path is more important in this scenario as the center path along which the ray propagates without being bent does not exist anymore. The incident angle for the edge path $\theta_{\text{in,max}}$ is determined by solving (2.18) with:

$$A = \frac{D}{2} - T \frac{S_{\text{out}}}{2\sqrt{\varepsilon_{r,\text{min}} - S_{\text{out}}^2}}, \quad B = T \frac{n_{\text{in}}}{\sqrt{\varepsilon_{r,\text{min}} - S_{\text{out}}^2}}. \quad (2.28)$$

The OPL for other positions can be found by first writing x_2 from (2.16) as a function of incident angle θ_{in} :

$$x_2 = T \frac{S_{in} + S_{out}}{2\sqrt{\varepsilon_{r1} - S_{in}^2}} + F \tan \theta_{in}. \quad (2.29)$$

Combining (2.9), (2.29) and substituting into (2.27), each ray's OPL through the lens can be represented. Using numerical solver, such as `vpasolve` in MATLAB, the solution for the permittivity distribution can be found by equating the OPL of any ray to the edge one.

It is worth mentioning that the ray will still be bent even if it is normally incident into the lens for scanning scenarios. This can be explained with the Eikonal ray equation:

$$\frac{d}{ds} \left(n \frac{dr}{ds} \right) = \frac{\partial n}{\partial r}, \quad (2.30)$$

where r is the ray trajectory. Under the Cartesian coordinate system, (2.30) can be decomposed into x , y , and z components. For the 2D GRIN lens under study, the $\partial n / \partial x$ is non-zero and thus it can still bent a normal incident ray. In other words, the ray trajectory will not be straight if the relative permittivity locally has a nonzero derivative.

Examples of Lens Design

For comparison, the lens re-designed to be optimized for scanning using the same specifications as the designed collimating lens ($F/D = 1$) are simulated. The permittivity distributions and transmitted angles across the lenses are plotted in Fig. 2.9. The solid curves refer to the relative permittivity and dashed curves represent the transmitted angles.

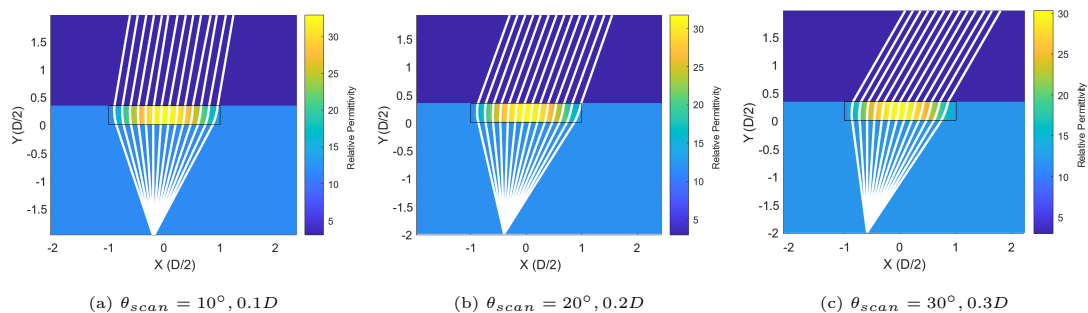


Figure 2.8: Ray tracing simulations for scanning lenses

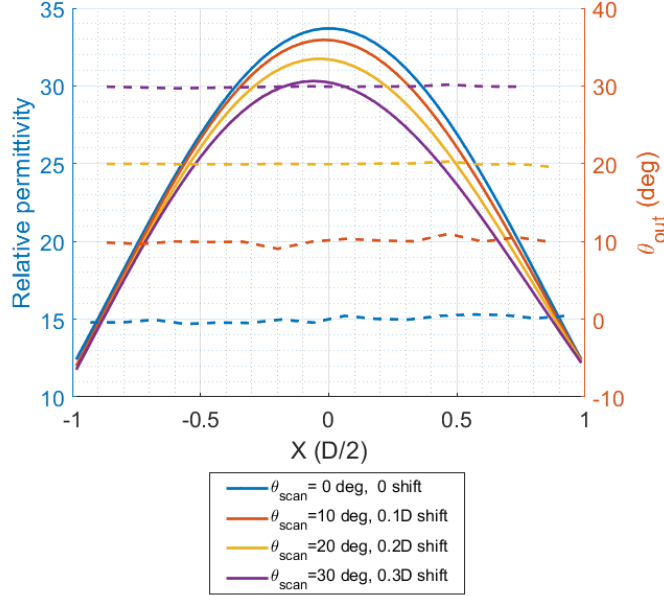


Figure 2.9: Permittivity Distribution and θ_{out} of each lens

It can be observed that now the transmitted angles are constant, correcting for the aberration shown earlier in Fig. 2.7.

2.5.2 Focal Length Transformation

In Sec. 2.4, a method to design a lens that converts a spherical wave in a certain medium into a spherical wave in a different medium, keeping the same focal point. In this section, a more general case is studied, which considers a transmitted spherical wave with a different (virtual) focus. This is equivalent to a quasi-optical system that changes the focal length. By doing this, it is possible to enlarge or narrow the equivalent subtended angle (from $\theta_{\text{in,max}}$ of the feed alone to $\theta_{\text{out,max}}$ of the feed-flat lens system). For example, the system could feed a larger elliptical or hyper-hemispherical lens. For mmWave and terahertz frequency, curved lenses are difficult to manufacture due to the required accuracy of the lens profile. The precision of the manufacturing is higher for shallow lenses, characterized by large F/D . Therefore, for the application with a secondary lens, the F -number of the system can be increased to simplify the manufacturing of the secondary lens. Assuming now the distance between the virtual feed and the actual feed is Δz , the new equivalent focal length is:

$$F' = \sqrt{(\Delta z + F + T)^2 + \left(\frac{D}{2}\right)^2}. \quad (2.31)$$

The extra path $L(x)$ in this case can be quantified as:

$$L(x) = F' - \frac{T + F + \Delta z}{\cos \theta_{\text{out}}}. \quad (2.32)$$

Still, for the last ray propagating through the upper edge of the lens:

$$x_1 = (F + \Delta z) \tan \theta_{\text{out,max}}, \quad x_2 = \frac{D}{2}. \quad (2.33a)$$

The approach to find this $\theta_{\text{in,max}}$ is the same as the previous cases: substituting (2.33) into (2.16) and a 4-th order function of $\theta_{\text{in,max}}$ similar to (2.18) can be formed with:

$$A = (F + T + \Delta z) \tan \theta_{\text{out,max}} - \frac{TS_{\text{out}}}{2\sqrt{\varepsilon_{r,\text{min}} - S_{\text{out}}^2}}, \quad B = \frac{Tn_{\text{in}}}{\sqrt{\varepsilon_{r,\text{min}} - S_{\text{out}}^2}}. \quad (2.34)$$

Since the optical path length of the edge ray is well-defined, the n_{max} is also available from (2.24). The further steps for finding θ_{in} with respect to each θ_{out} and the distribution of ε_r are identical to the ones described in Sec. 2.4.

Examples of Lens Design

The equations are applied to design lenses with $\varepsilon_{r,\text{min}} = 12$ and radiating from silicon ($\varepsilon_r=12$) to quartz ($\varepsilon_r=3.8$). The thickness is given as $0.135D$. Fig. 2.10a shows the lens design for reducing the feed $\pm 48^\circ$ illumination beam into a $\pm 20^\circ$ beam. Δz of this case is calculated as $0.92D$. The corresponding F/D is increased from 0.45 to 1.37. Fig. 2.10b shows the lens for shaping beams from $\pm 30^\circ$ to $\pm 10^\circ$, resulting in a F/D increasing from 0.87 to 2.58.

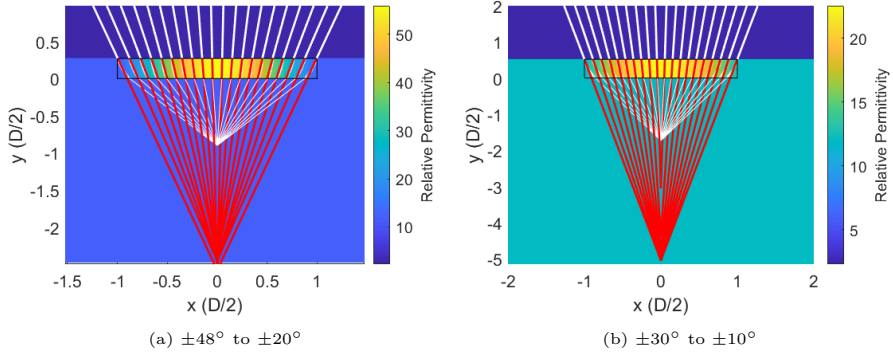
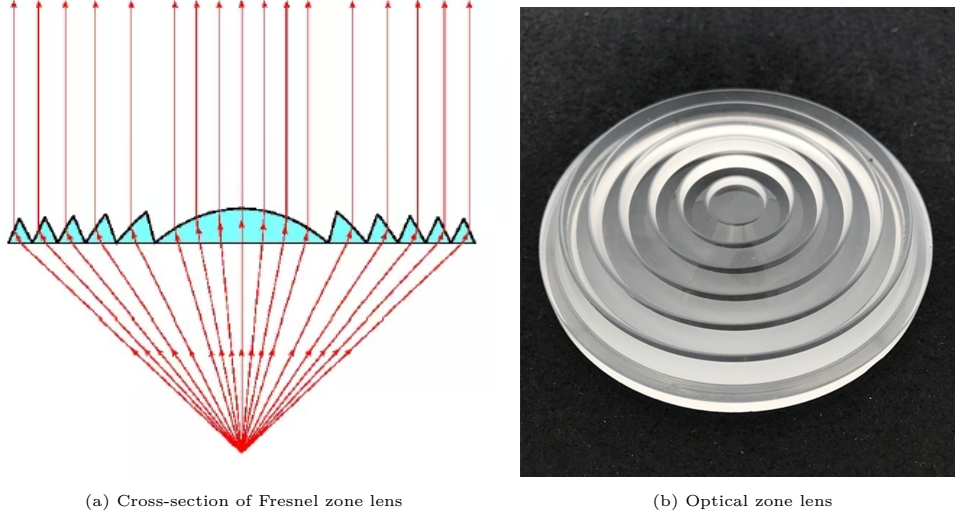


Figure 2.10: Example of GRIN lenses for transforming focal length.

2.5.3 Fresnel Zone Lens

A Fresnel zone plate lens consists of a flat, circular plate with a series of concentric circular zones, similar to other types of Fresnel lenses. However, unlike traditional Fresnel lenses that use alternating transparent and opaque zones, a Fresnel zone plate



(a) Cross-section of Fresnel zone lens

(b) Optical zone lens

Figure 2.11: Fresnel zone lens.

lens uses zones with different thicknesses. The zones of a Fresnel zone plate lens act as phase-shifting elements for the incident wavefront. Each zone has a specific optical path length, which causes a phase delay in the transmitted or diffracted waves.

In [29], the equations for each zone's radii and the corresponding permittivity required for a multi-dielectric Fresnel zone lens are presented. A set of similar equations based on GRIN techniques are given in [30]. Fresnel zone lens can also be realized with the design equations above. Regarding the phase front, the Fresnel zone lens performs the same as the collimating lens within one zone while the phase difference between adjacent zones is 2π . Therefore, the design equations are the same as the collimating lens for the centre zone of a particular zoned lens. The phase difference between the i -th zone lens and the centre one is $\Delta\phi = i \cdot 2\pi$. Designing such lenses is approached by equating the phase variation through the edge with the summation of OPL through the i -th zone lens and multiple phase wrappings difference:

$$n_{\text{in}}F + n_{\text{max}}T = n_{\text{in}}\frac{F}{\cos\theta_{\text{in}}} + \int_{P_1}^{P_2} nds + i\frac{2\pi}{k_0}. \quad (2.35)$$

Examples of Lens Design

Here, we reported an example Fresnel zone design with $\epsilon_r = 8$ dielectric as the substrate, transforming a $\pm 48^\circ$ beam to a $\pm 20^\circ$ beam in silicon. The whole lens can be separated into four zones, with the ray paths and permittivity distributions shown in Fig. 2.12.

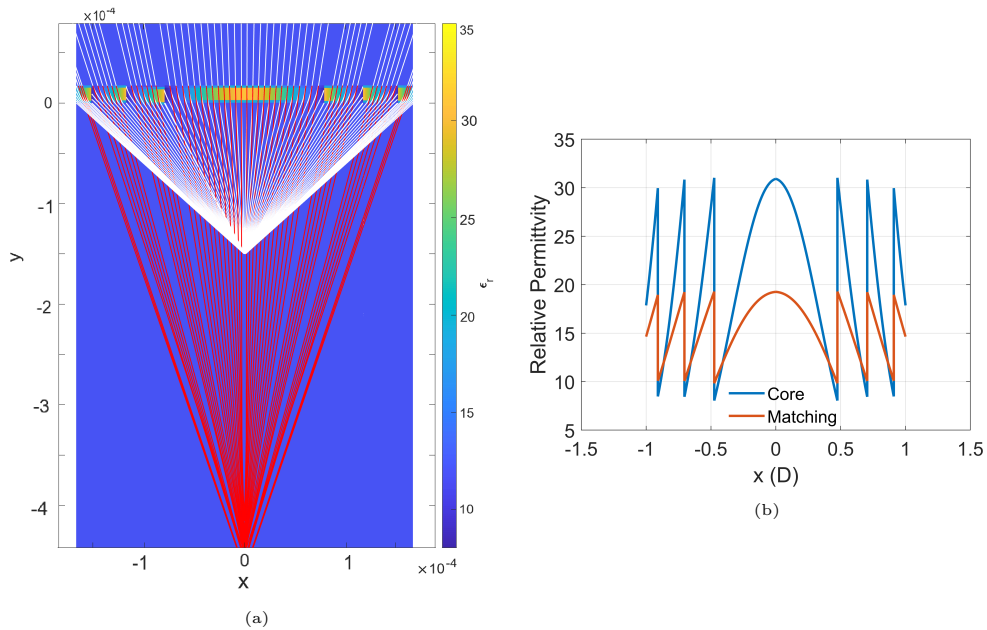


Figure 2.12: (a) Ray tracing simulations and (b) permittivity distribution for the example design.

It can be noticed that several rays are not plotted in Fig. 2.12a. The reason for this is these ray propagate through the interface of two zones, which brings in the abrupt variations on permittivity. In these area, the Eikonal equation is not valid and the Fresnel equation should be used instead. Another example design with specific ADLs synthesis and full wave simulations is presented in Chap. 5 in detail.

Note that for most of the case studied, the approach of expressing everything with ϵ_{r2} (equivalently in x_2) is used. For example, in the study of the collimating lens, using ϵ_{r1} refers to fixed n_{\max} scenario while writing everything in ϵ_{r2} corresponds to a fixed thickness case. Therefore, choosing either parameter as the main independent variable for lens designing is possible, depending on the available specifications.

Chapter 3

Flat Lens Prototype Design

To verify the design procedure of the previous chapter, a flat GRIN lens ($F/D = 0.67$) with a bandwidth from 30 to 60 GHz is designed with a 6λ (30mm) diameter at the highest frequency. This lens is designed to transform a spherical wave into a planar wave in free space.

3.1 Lens Geometry

We chose to use the printed circuit board (PCB) technique as the manufacturing process to reduce the cost of the prototype. The Rogers RO4003C™ laminate board [31] is a relatively cheap and common substrate option for PCB prototypes. This material has a typical dielectric constant of 3.55 and a loss tangent of 0.0027 (@ 10 GHz) and offers laminates with different thicknesses, varying from 0.203mm to 1.524mm. The minimum gap width, i.e. the smallest distance between the metal patches, is 130μm, and the minimum track width is 130μm for PCB process. Based on these technology constraints, we chose the maximum relative permittivity at the center of the lens to be around 22. This value is obtained by considering the minimum gap width for the metal layer and the minimum dielectric thickness (inter-layer distance in the artificial dielectric). Moreover the period of the patches is kept below 0.25λ at the highest frequency of operation, to reduce the losses and the dispersion of the artificial dielectric.

Since the GRIN lens to be designed has a fixed permittivity in the z -direction, high reflection losses are estimated at the interfaces of the lens and free space due to mismatch. Adding an impedance transformer is the most typical way to match the lens to free space. The intrinsic impedance of the matching slab is chosen as:

$$Z = \sqrt{Z_{\text{core}} Z_{\text{out}}}, \quad (3.1)$$

where Z_{core} is the impedance of the lens material and Z_{out} is the characteristic impedance of material outside the lens (air in this example). The thickness of the matching layer is a quarter wavelength inside the material at the center frequency.

One disadvantage of using a single quarter-wave matching layer is the narrow bandwidth. For wideband operation, a two-section impedance transformer was designed for

the prototype. The outer matching layer was designed to have a fixed relative permittivity of 2, with a quarter wavelength thickness at the center frequency, constant across the lens. The thickness of inner matching layer is also constant across the lens, but its permittivity is varying. For this reason, the inner transformer is not quarter wavelength everywhere across the lens. Since the maximum transformation ratio appears at the center of the lens, the inner matching layer has a thickness of quarter wavelength at the center frequency in the material with $\varepsilon_r = \sqrt{\varepsilon_{r,\max} \varepsilon_{r,\text{outer}}}$. The permittivity of the inner matching layer varying follows

$$\varepsilon_{r,\text{inner}} = \sqrt{\varepsilon_{r,\text{core}} \varepsilon_{r,\text{outer}}}. \quad (3.2)$$

With $\varepsilon_{r,\text{in}} = 1$, $\varepsilon_{r,\text{out}} = 1$ and $\varepsilon_{r,\text{min}} = 3.55$, the procedure described in chapter 2 leads to lens having a maximum relative permittivity $\varepsilon_{r,\max} = 22$ at the center with a thickness of $T = 1.7\text{mm}$. The minimum relative permittivity of the inner matching layer is forced to be equal to the hosting medium of the ADL patches. The matching performances of this 5-section structure are plotted in Fig. 3.1a, assuming that ideal materials are used. The simulation is based on a transmission line model corresponding to a plane wave under normal incidence.

The relative permittivity distributions of the core and the inner matching layer are plotted in Fig. 3.1b. By introducing the matching layers, the transmitted ray will be over-bent by the lens, as the design equations are not optimized for the extra optical path length generated by the matching layers. One way to solve this is to shrink the lens core thickness to compensate for the additional phase shift due to the matching layers. The complete lens with a thickness of the core reduced to 73% of its original value is shown to have all transmitted angles falling in the $\pm 1^\circ$ range in Fig. 3.1c.

3.2 Core Unit Cell Design

The different unit cells composing the lens are realized by the artificial dielectric layers to have varying relative permittivity in the core layer. To ensure the equivalent circuit model of ADL is valid, the periodicity in three dimensions should be electrically small. Therefore, the period of the unit cell (periodicity in x and y directions) is selected as $p = 1.2\text{mm}$, which is less than a quarter wavelength at the highest frequency. Considering both the fabrication limits and maximum permittivity to achieve, the periodicity in z -direction d_z is 0.304mm . With these geometrical parameters fixed, the relative permittivity as a function of the gap width can be plotted for different frequencies (Fig. 3.2).

The periodicity of the ADL is chosen as $p = 1.2\text{mm}$ ($0.18\lambda_0$) to keep the patches' size sub-wavelength. This period gives 25 unit cells across the lens aperture. With the relative permittivity distributions shown in Fig. 3.1b, the curves are first discretized into piecewise constant distribution equal to the value at the center of each unit cell. The permittivity of the unit cell required is used to synthesize the equivalent ADL structure at the center frequency to ensure a relatively stable permittivity across the band. The minimum gap width, which appears at the center unit cell, is $230\mu\text{m}$. The last unit

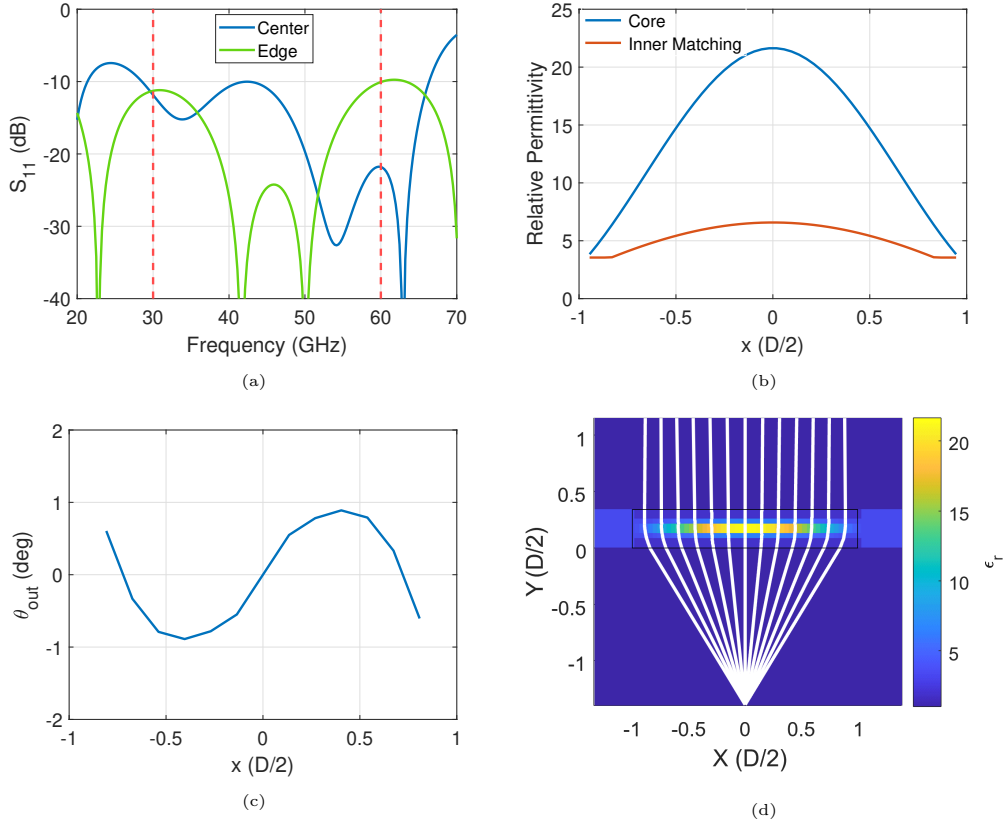


Figure 3.1: (a) Reflection coefficients at center and edge of the lens, assuming the ideal materials are used. (b) The distribution of relative permittivity of core and inner matching layer. (c) The transmitted angle of the shrank lens. (d) The ray paths through the lens.

cell near the edge is purely dielectric, with no metal inclusions. The unit cell stackup is symmetric so that two halves of the lens can be realized on the same board and then assembled together to reduce the manufacturing cost. This symmetry will be elaborated on in Sec. 3.4 and Fig. 3.8.

3.3 Matching Layer Design and Synthesis

Given the maximum relative permittivity being around 22, a two section impedance transformer is applied in this design to reduce the reflection losses at the interface between the lens and free space, both above and below the lens. The inner matching layer has varying refractive indices across the lens while the outer matching layer has a fixed relative permittivity of 2, to simplify the manufacturing. Hence, these two sections are synthesized with different methods.

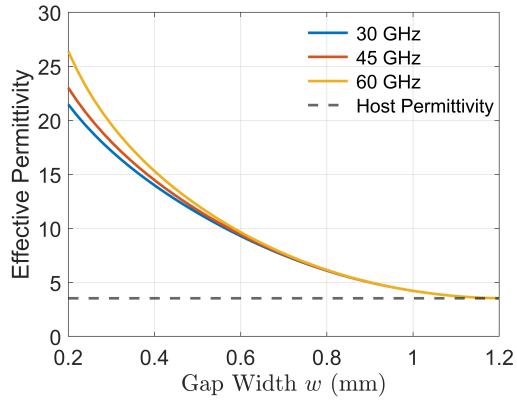


Figure 3.2: Realized effective permittivity of the ADL as a function of the gap width for different frequencies.

3.3.1 Inner Matching Layer

The inner matching layer was realized in a similar way as the core. The combined center unit cell is shown in Fig. 3.3.

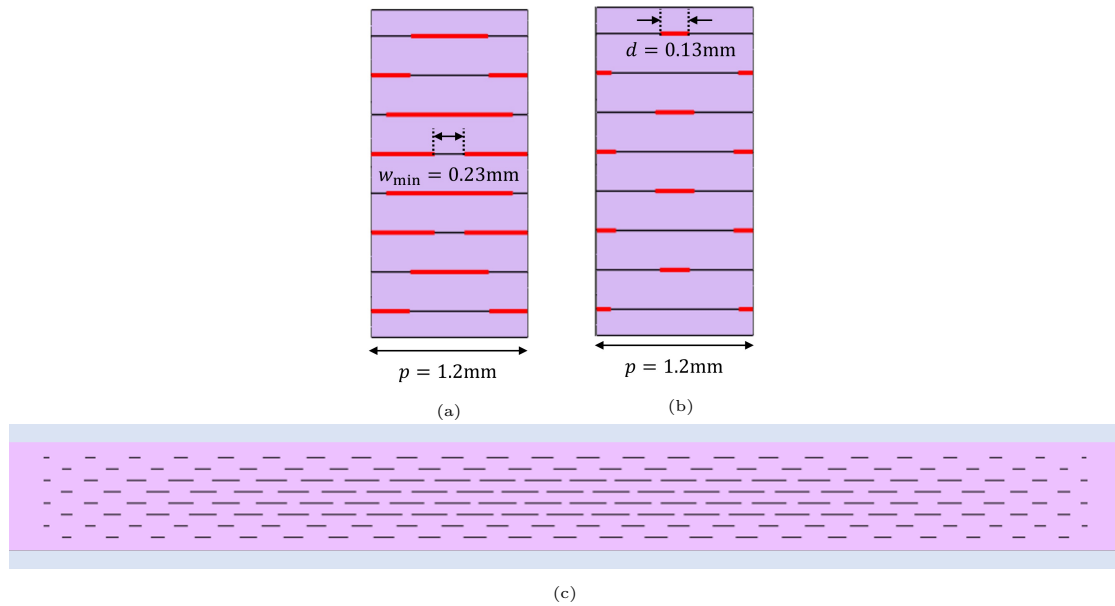


Figure 3.3: Cross section of (a) the center unit cell, (b) the last unit cell with metal, and (c) the entire lens.

The reflection coefficient of the combined unit cells, including a second matching layer above and below with $\epsilon_r = 2$ and thickness 1.12mm, are plotted in Fig. 3.4a, normalized to the impedance of free space. The S-parameters of the unit cells are found using the ADL equivalent circuits.

For evaluating the deviation between the synthesized ADL lens and the ideal GRIN

lens, the phase distribution of the field above the lens is plotted for both lenses in Fig. 3.4b. A similar profile can be recognized for the ideal continuously varying permittivity and the discretized ADL version, characterized by a stepped profile of the phase.

As mentioned above, the inner matching layer is constraint to have the same thickness across the lens, so that it can be realized with a single PCB stackup.

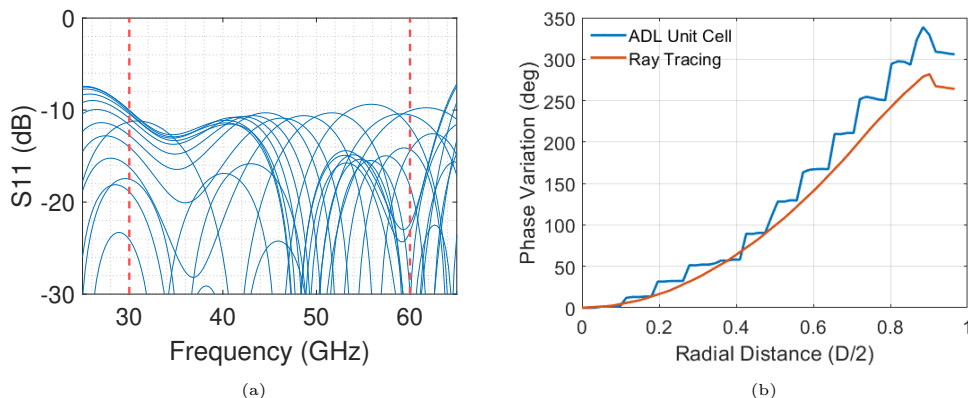


Figure 3.4: (a) S_{11} for all unit cells and (b) phase variations of ADL synthesized lens and ideal GRIN lens.

3.3.2 Outer Matching Layer

For the ADL technique with metallic inclusions, a relative permittivity lower than the host material is not realizable. The possible solutions for the $\epsilon_r = 2$ outer matching layer is to either use directly an existing dielectric material with $\epsilon_r = 2$ or add perforations into an electrically denser material to reduce its effective permittivity.

There are series of polymers having dielectric constant close to 2. For example, Polytetrafluoroethylene (PTFE) $\epsilon_r = 2.1$; Polypropylene (PP) $\epsilon_r = 2.2$; Polyethylene (PE) $\epsilon_r = 2.2$; Polystyrene (PS) $\epsilon_r = 2.5$; cyclic olefin copolymer (COC) $\epsilon_r = 2.1$ and etc. However, these types of material are not easy to assemble into multi-layer PCB, because of their thermal and mechanical properties.

Alternatively, one can use the same hosting medium as the lens ($\epsilon_r = 3.55$) with periodic perforations to realize a reduced effective permittivity. Several studies have been done based on the perforation on a homogeneous dielectric substrate [32–34]. The analytical formulas of effective medium theory for calculating the effective permittivity of porous structures are presented in [35]. The basic models for retrieving the effective permittivity from a mixing structure are described in [36] and will be outlined here.

A group of common rules for 2-D mixtures can be summarized as:

$$\frac{\epsilon_{\text{eff}} - \epsilon_e}{\epsilon_{\text{eff}} + \epsilon_e + v(\epsilon_{\text{eff}} - \epsilon_e)} = f \frac{\epsilon_i - \epsilon_e}{\epsilon_i + \epsilon_e + v(\epsilon_{\text{eff}} - \epsilon_e)}, \quad (3.3)$$

where:

- ε_{eff} is the effective permittivity of the mixing structure
- ε_e is the permittivity of the substrate
- ε_i is the permittivity of the inclusions
- f is the volume portion of the inclusions in percentage
- v is a dimensionless parameter that leads to different mixing formulas

With $v = 0$, it gives the Maxwell-Garnett (MG) formula; with $v = 1$, it gives the Bruggeman formula; with $v = 2$, it gives the Coherent Potential formula. These three formulas are compared in [37] by simulating perforating on two different substrates: Rogers RO4003 ($\varepsilon_r = 3.38$) and material with $\varepsilon_r = 10$. The MG formula better fits the effective permittivity with the simulation results. This superiority is more noticeable for substrates with higher permittivity. Therefore, the MG formula is applied in this study.

For the case of an isotropic mixture, a more general MG formula is given [38]:

$$\varepsilon_{\text{eff}} = \varepsilon_e + \frac{\sum_{i=1}^3 \frac{f\varepsilon_e(\varepsilon_i - \varepsilon_e)}{3[\varepsilon_e + N_i(\varepsilon_i - \varepsilon_e)]}}{1 - \sum_{i=1}^3 \frac{fN_i(\varepsilon_i - \varepsilon_e)}{3[\varepsilon_e + N_i(\varepsilon_i - \varepsilon_e)]}}. \quad (3.4)$$

Under the Cartesian coordinate system, $i = x, y, z$, and N_i is the depolarization factor along the corresponding direction. In the International System of Units (SI), the depolarization factors are positive and satisfy:

$$N_x + N_y + N_z = 1. \quad (3.5)$$

The depolarization factors for different porous shapes and different orientations are shown in Table 3.1 [39].

Shape	Axis	N
Sphere	any	1/3
Thin Slab	normal	1
Thin Slab	in plane	0
Long circular cylinder	longitudinal	0
Long circular cylinder	transverse	1/2

Table 3.1: Depolarization factors.

We consider a perforation axis along the z -direction. From Table 3.1, if the perforation axis is parallel to the E-field orientation (TM), the depolarization factor is 0, while it is $\frac{1}{2}$ if the perforation axis is perpendicular to the E-field (TE). The permittivity tensor for an anisotropic material can be expressed as:

$$\varepsilon = \begin{bmatrix} \varepsilon_{xx} & \varepsilon_{xy} & \varepsilon_{xz} \\ \varepsilon_{yx} & \varepsilon_{yy} & \varepsilon_{yz} \\ \varepsilon_{zx} & \varepsilon_{zy} & \varepsilon_{zz} \end{bmatrix} \quad (3.6)$$

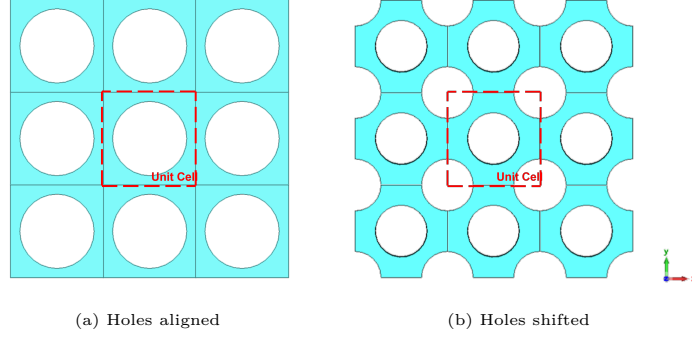


Figure 3.5: Two different unit cell geometries for the outer matching layer.

With the given choice of the reference system, the permittivity matrix can be written as diagonal, which simplifies (3.6) as:

$$\varepsilon = \begin{bmatrix} \varepsilon_x & 0 & 0 \\ 0 & \varepsilon_y & 0 \\ 0 & 0 & \varepsilon_z \end{bmatrix} \quad (3.7)$$

For a z -direction stratified structure, the permittivity tensor of the structure can be written as [40]:

$$\varepsilon = \begin{bmatrix} \varepsilon_{TE} & 0 & 0 \\ 0 & \varepsilon_{TE} & 0 \\ 0 & 0 & \varepsilon_{TM} \end{bmatrix}. \quad (3.8)$$

Substituting N into ε_{eff} , one can have the $\varepsilon_{\text{eff,TE}}$ and $\varepsilon_{\text{eff,TM}}$ for cylindrical perforation:

$$\varepsilon_{\text{eff,TE}} = \varepsilon_e + 2f\varepsilon_e \frac{\varepsilon_i - \varepsilon_e}{\varepsilon_i + \varepsilon_e - f(\varepsilon_i - \varepsilon_e)} \quad (3.9)$$

$$\varepsilon_{\text{eff,TM}} = f\varepsilon_i + (1 - f)\varepsilon_e. \quad (3.10)$$

We designed two different circular cylinder porous geometries. One geometry has one hole in the center of the unit cell cube (holes are aligned). The other one has one hole in the center with a quarter circle on each corner (see Fig. 3.6). The same substrate (Rogers RO4003C) is selected as the host material for perforation. Substituting $\varepsilon_e = 3.55$, $\varepsilon_i = 1$, $\varepsilon_{\text{eff,TE}} = 2$ into (3.9), the volume portion of air $f = 0.49$ can be determined, meaning almost half of the original substrate in the unit cell need to be removed. Since the holes are drilled through the substrate, the volume ratio can be simplified as the area ratio. For the geometry where holes are aligned, $f = 0.49$ corresponds to 0.4mm hole radius (from $f = \pi r^2/p^2$). For the other geometry, $r = 0.28\text{mm}$ holes will give $\varepsilon_{r,\text{eff}} = 2$ ($f = 2\pi r^2/p^2$).

We then simulated the fore-mentioned two geometries with thee calculated perforation size. For both cases, we consider an original unit cell of size 1mm by 1mm by 1.12mm. These two models are simulated in CST Microwave Studio assuming broadside incidence, with Floquet boundary conditions (Fig. 3.6).

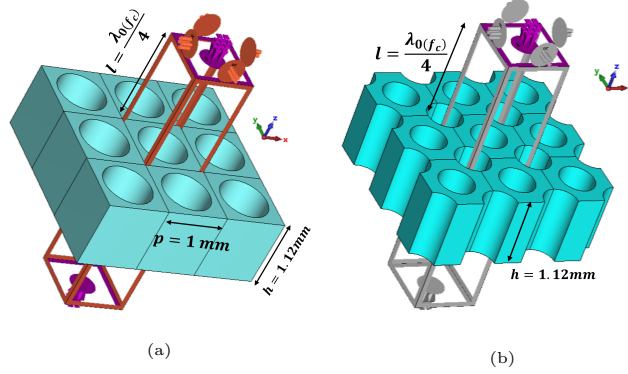


Figure 3.6: CST models of the two considered perforated unit cells.

The ϵ_{eff} of the structure can be extracted from the simulated S-parameters. The idea for finding the equivalent permittivity of the unit cell is to equate the phase variation from port 1 to port 2 through the structure under simulation with the one through a sample material with $\epsilon_r = \epsilon_{r,\text{eff}}$ with the same height. Therefore, $\epsilon_{r,\text{eff}}$ can be written as:

$$\epsilon_{r,\text{eff}} = \left(\frac{\angle S_{21}}{k_0 h} \right)^2. \quad (3.11)$$

The effective permittivity extracted using (3.11) is plotted in Fig. 3.7a. It can be noticed that both geometries have an equivalent permittivity around 2 across the band. Therefore, the design procedure based on MG formula is verified. In Fig. 3.7, the variations of permittivity versus the hole size are plotted.

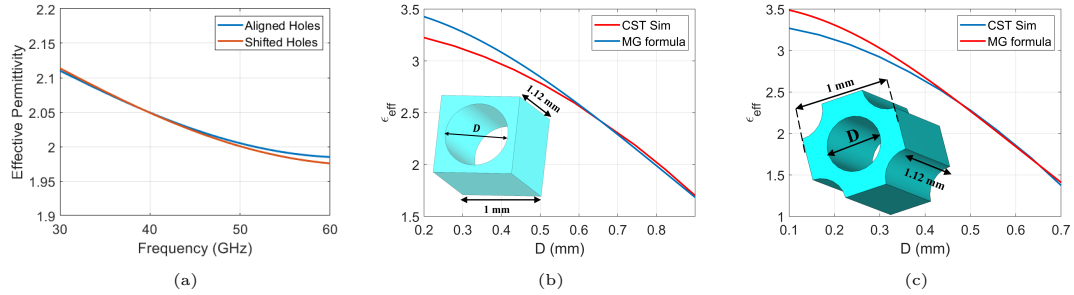


Figure 3.7: (a) Effective permittivity variation across the band. Effective permittivity versus perforation diameter of (b) aligned holes (c) shifted holes.

From Fig. 3.5, the minimum width of the dielectric grid is slightly larger for the aligned case. With $r_{\text{aligned}} = 0.4\text{mm}$ and $r_{\text{shifted}} = 0.28\text{mm}$, the minimum width of the dielectric trace can be calculated as 0.2mm and 0.14mm , respectively. Thus, the first unit cell design is selected to realize the $\epsilon_r = 2$ matching layer due to its better mechanical robustness, compared to the shifted design.

3.4 Detailed Design

The total stackup of the PCB flat lens is shown in Fig. 3.8. To reduce the cost of manufacturing, the prototype has a symmetrical structure in the z -direction. Hence, the complete 8-layer PCB can be separated into two 4-layer boards. The spacing between layers is realized by a RO4003C laminate with $203\mu\text{m}$ thickness and a RO4450F bondply [41] ($\epsilon_r = 3.52$) with $101\mu\text{m}$ thickness.

A spacer, a single layer of RO4003C Laminate with a thickness of $305\mu\text{m}$, is applied to have the same thickness without any bondply. The outer matching layer is realized by cylindrical perforations, drilled into two layers of RO4003C with a thickness of $508\mu\text{m}$ connected by one layer of $101\mu\text{m}$ RO4450F bondply to approach the quarter wavelength thickness (1.2mm).

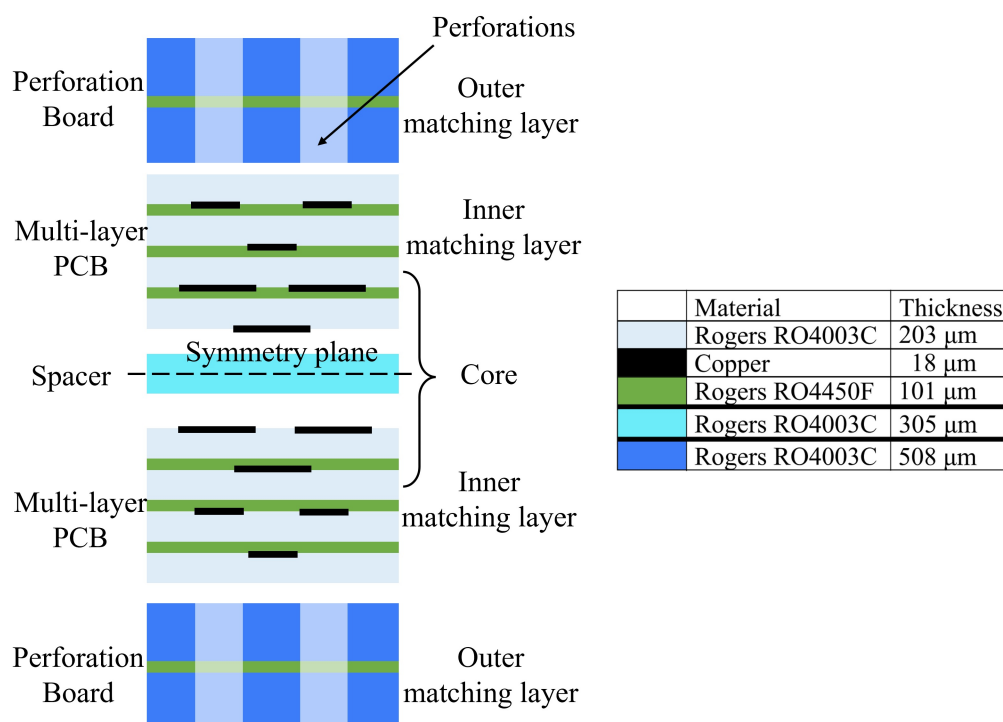


Figure 3.8: Prototype stack-up.

The lens is designed in a cylindrical shape with a diameter of 32mm so that the metal would not be too close to the substrate edge. Four holes for mounting screws are placed symmetrically. To satisfy the manufacturing rules, given that the minimum patch size to manufacture is $130\mu\text{m}$, all the patches smaller than $65\mu\text{m}$ are removed while others are replaced by square patches with a side length of $130\mu\text{m}$. The patches are made of copper with NiAu surface finishing. The thickness of the metal is $35\mu\text{m}$ and $18\mu\text{m}$ for the outer and inner layers respectively. Fig. 3.9 displays the layout for each part of the prototype.

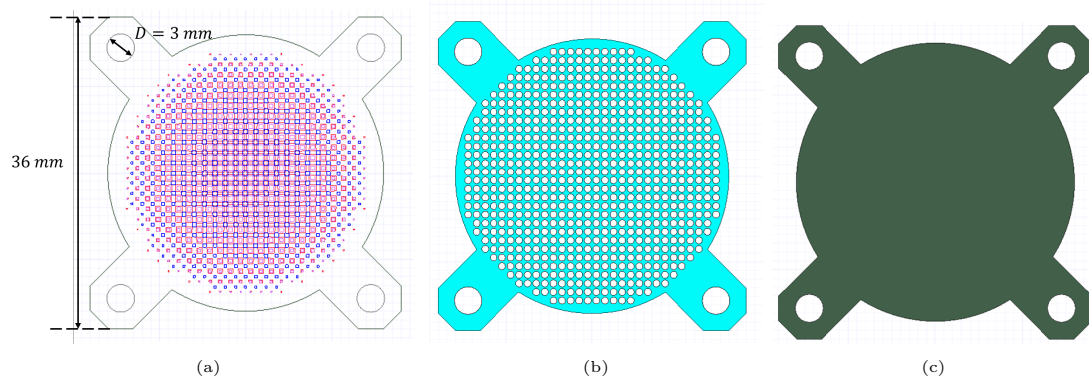


Figure 3.9: The schematic of (a) the core layer with metal, (b) the matching layer with perforations, and (c) the spacer between two multi-layer PCBs.

A metal plate with a 30mm diameter circular window, which is made of 316 stainless steel with 1mm thickness, is used as the lens holder.

Chapter 4

Prototype Simulations and Measurements

In this chapter, the validations of the designed prototype are reported by means of full-wave simulations and the measurements on the prototype. The simulation results include both the ones illuminated by standard open-ended waveguide and the alternative feeds. The actual far-field radiation patterns of the prototype is obtained by measuring the near field scanning and transformed to far field based on the equivalent theorem and free space Green's function. The gain of the lens is measured using the three antenna methods based on Friis equation.

4.1 Full-Wave Simulations

4.1.1 Efficiencies

To characterize the lens performance, a series of efficiencies can be calculated for analysis:

Spill-over efficiency η_{so} is a measure of how much power from the feed is intercepted by the lens. It is calculated from the pattern of the feed:

$$\eta_{\text{so}} = \frac{\int_0^{2\pi} \int_0^{\theta_0} U_{\text{feed}}(\theta, \phi) \sin \theta d\theta d\phi}{\int_0^{2\pi} \int_0^{\pi} U_{\text{feed}}(\theta, \phi) \sin \theta d\theta d\phi}, \quad (4.1)$$

where θ_0 is the subtended angle of the lens and U_{feed} is the radiation intensity from the feed. For this prototype, the subtended angle is: $\theta_0 = \tan^{-1}[D/(2F)] \approx 37^\circ$.

Taper efficiency η_t is an indicator of how uniform the equivalent aperture field is. This efficiency can be calculated as following:

$$\eta_t = \frac{1}{A} \frac{|\iint_A \vec{E}_a dA|^2}{\iint_A |\vec{E}_a|^2 dA}, \quad (4.2)$$

where A is the physical size of the lens, \vec{E}_a is the electric field on the aperture in the near field of the lens. It can be also regarded as a parameter quantifying how much the lens area is effectively used for radiating. Hence, the taper efficiency is also given as:

$$\eta_t = \frac{A_{\text{eff}}}{A} = \frac{D}{D_{\text{max}}}, \quad (4.3)$$

where D is the realized directivity and D_{\max} is the theoretical achievable maximum directivity for a given physical size ($D_{\max} = 4\pi A/\lambda^2$). The taper efficiency can be decomposed into the amplitude taper loss (ATL) and the phase error loss (PEL), with:

$$\text{ATL} = \frac{\left(\iint_A |\vec{E}_a| dA\right)^2}{A \iint |\vec{E}_a|^2 dA} \quad (4.4a)$$

$$\text{PEL} = \frac{|\iint_A \vec{E}_a dA|^2}{\left(\iint |\vec{E}_a| dA\right)^2}, \quad (4.4b)$$

where the last equation is only valid for broadside, while a slightly different formula has to be used for scanning, with additional terms.

Ohmic efficiency η_{ohmic} is calculated as follows:

$$\eta_{\text{ohmic}} = 1 - \frac{P_{\text{loss,diel}} + P_{\text{loss,metal}}}{P_{\text{acc}}\eta_{\text{so}}} \quad (4.5)$$

where $P_{\text{loss,diel}}$ and $P_{\text{loss,metal}}$ are the power lost in dielectric and metal, respectively, while P_{acc} refers to the power accepted by the lens. These values can be found from full-wave simulations.

Aperture efficiency η_{ap} is a measure of how effectively an antenna collects or radiates electromagnetic energy within a certain solid angle. It is given by

$$\eta_{\text{ap}} = \eta_{\text{so}} \eta_t = \frac{G\lambda^2}{4\pi A_{\text{eff}}}, \quad (4.6)$$

where A_{em} is the maximum effective area of the aperture. A higher aperture efficiency implies that the antenna is better at capturing or radiating energy.

4.1.2 Open-Ended Waveguide Feeds

The lens is simulated with three different standard open ended waveguides illumination. The basic specifications of the waveguides are shown in Table 4.1. Clearly, none of the

WG Name	Frequency	$f_{\text{cut-off}}$ next mode	Dimension (mm)
WR28	26.5 - 40 GHz	42.154 GHz	7.112 * 3.556
WR22	33 - 50 GHz	52.692 GHz	5.69 * 2.84
WR15	50 - 75 GHz	79.75 GHz	3.76 * 1.88

Table 4.1: Open-ended waveguide used in simulations and measurements.

waveguide in Table 4.1 can cover the entire prototype design bandwidth. Hence, the selection of waveguide depends on the simulation bands. From 30-40 GHz, the lens is simulated with the WR28. The WR22 is used to illuminate the lens through the band 40-50 GHz in the simulations. For higher frequency (50-60 GHz), WR15 is simulated with the lens. The pattern of each waveguide at their respective center simulation frequency are shown in Fig. 4.1a.

4.1.3 Broadside Simulated Performance

We first simulated the broadside pattern by placing the waveguide aligned with the lens axis with a distance $F = 20\text{mm}$ from the waveguide open end to the bottom of the lens.

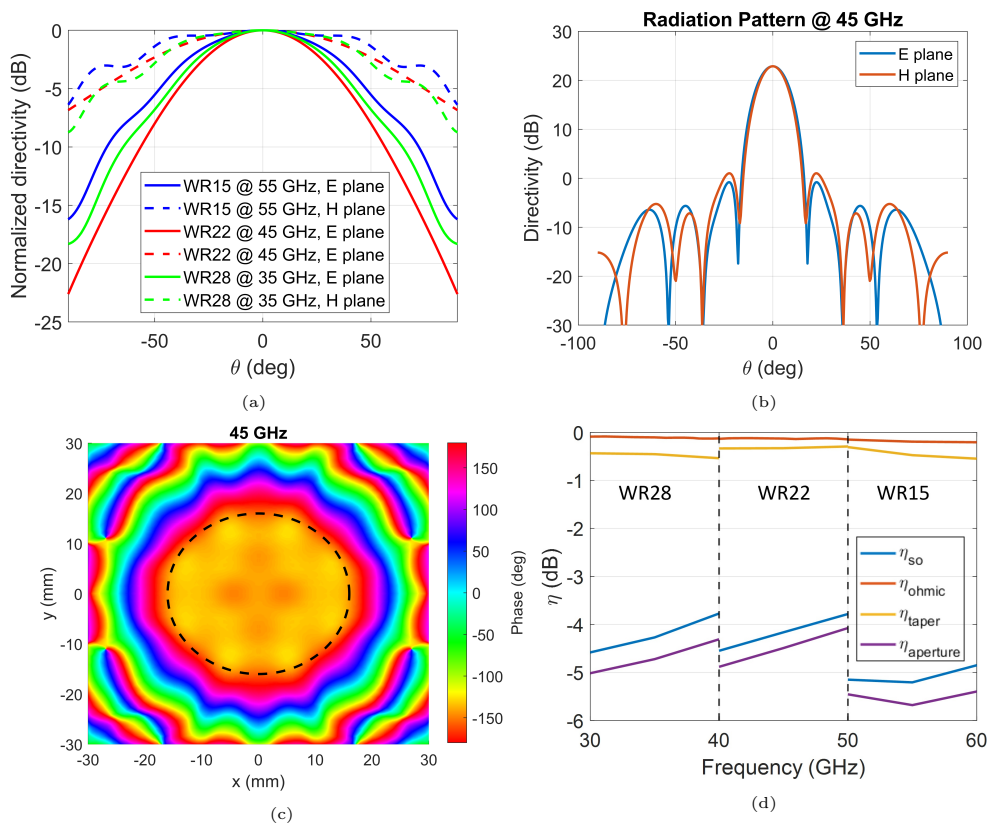


Figure 4.1: The simulation results of (a) the normalized patterns for three waveguides in the E- and H-planes (b) far field patterns in the E- and H-plane; (c) transmitted phase of the lens illuminated by WR22 at 45 GHz, where the lens aperture is shown as dashed line and (d) the calculated efficiencies across the band.

The radiation patterns and the phase on top of the lens at 45 GHz are plotted in Fig. 4.1b and Fig. 4.1c, respectively. A flat phase front can be observed from the plot, within the lens aperture, indicated by the dashed circle. Following the formulas in subsection 4.1.1, the efficiencies are calculated and presented in Fig. 4.1d. It can be noted that most of the losses are due to spillover, because of the large pattern from the open-ended waveguide. While this feed is not efficient to illuminate the lens under investigation, it is selected to demonstrate the properties of the lens and the validity of the design. Alternative feed solutions with improved spillover efficiency will be briefly discussed later in Sec. 4.4. The discontinuities in the curve are due to the change of feeding waveguides, which have different physical sizes and primary patterns.

Scan Simulated Performance

The scanning performance of the lens is also evaluated by having lateral shifts on the feed. The optimal shift is not on a line but on a curved surface. In [42], the scanning curve for a parabolic reflector is given as a paraboloid that has a curvature radius half that of the parabolic antenna based on the Petzval surface:

$$\Delta z = \frac{\Delta x^2}{2F}, \quad (4.7)$$

where $\Delta x/\Delta z$ represents the displacement to the focal point and F is the focal length of the system. The scan curve for a Fresnel zone lens is given in [43] and appears to be a circle:

$$\Delta x^2 + \Delta z^2 = F^2. \quad (4.8)$$

Both curves are simulated numerically for the designed lens (shown in Fig. 4.2) and they appear to be very similar for the considered F/D . Thus, the circular curve is selected for

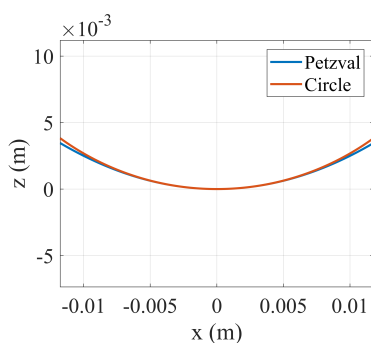


Figure 4.2: Comparison between two scan curves.

the simulations as it can be easily implemented in the CAD of the commercial software CST microwave studio. The full-wave simulations show that the main beam can be pointed to an angle θ if the feed is rotated by 1.2θ and tilted facing the lens center along the scan curve. With the main beam pointing towards 10° , 20° , 30° . The scanning patterns at the center frequency are plotted in Fig. 4.3.

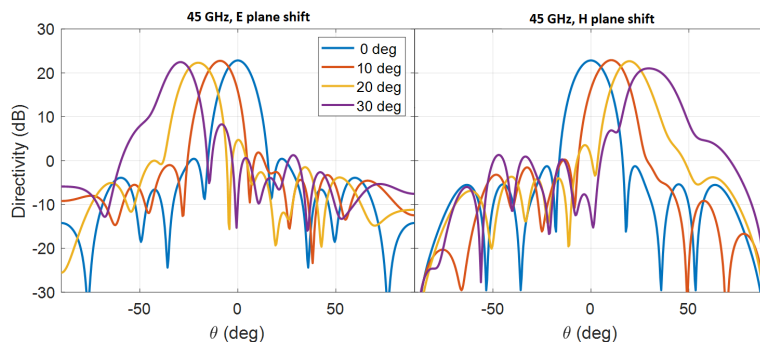


Figure 4.3: Simulated patterns for scanning in the E- and H-planes.

The full-wave simulated E-field are displayed in Fig. 4.4.

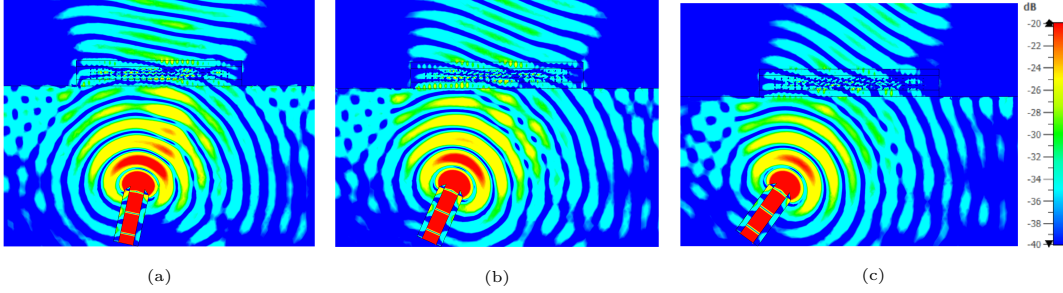


Figure 4.4: The 2D E-field for scanning to (a) 10° (b) 20° (c) 30°.

4.2 Prototype and Measurement

The prototype of the 30-60 GHz flat lens is manufactured following the architecture shown in Fig. 3.8 and the layout shown in Fig. 3.9. This prototype aims to demonstrate the wide bandwidth characteristic due to the application of ADLs and validate the analysis and design procedures. The photographs of the prototype's core layer, matching layer and the complete assembled lens are shown in Fig. 4.5.

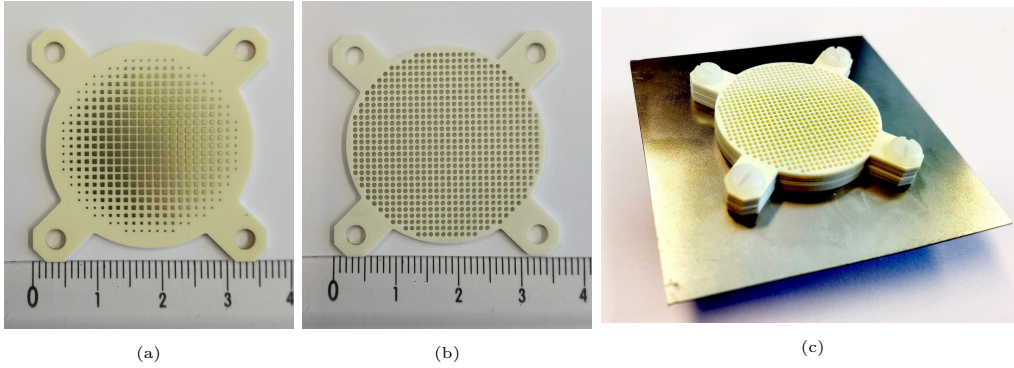


Figure 4.5: Prototype pictures of (a) the core layer with metal (b) the outer matching layer with perforations to achieve $\epsilon_r = 2$ (c) the assembled prototype (the metal plate is for demonstration only, not the real size).

4.2.1 Measurement Setup

We used a vector network analyzer (VNA) and two identical open-ended waveguides to characterize the lens. The lens was measured using WR28 from 30-40 GHz and WR15 from 50-60 GHz, while no measurements are available from 40 to 50 GHz. A holder for supporting the feeding waveguide and the lens was designed and 3D printed (as seen in Fig. 4.6a). The flange of the waveguide was screwed to this holder. The lens was placed on top of a 160mm by 160mm by 1mm stainless steel plate with a circular window in the center with diameter $D = 30$ mm. This plate was located 20mm (focal length) away

from the waveguide's open end. The metal plate was designed relatively large w.r.t. the lens to provide a good shielding performance and hence a clean pattern can be acquired. Four plastic screws were used to keep good alignment between the metal plate and the 3D printed holder. The feeding waveguide and the probe waveguide were connected to the two ports of the VNA using a coaxial-to-waveguide adaptor and a coaxial cable. The probe was mounted on the 3-axis computer numerical control (CNC) machine vertically to realize the near field scanning (as shown in Fig. 4.6b). Multiple absorbers were used to reduce the scattering and reflections within the measurement setup.

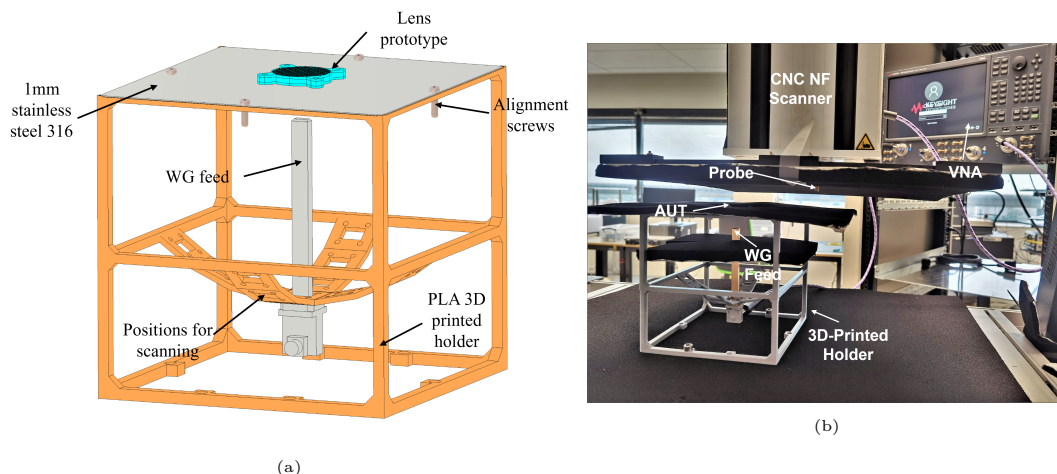


Figure 4.6: Measurement setup.

4.2.2 Radiation Pattern Measurement

The far field radiation patterns were obtained through near-field (NF) to far-field (FF) transformation. To measure the radiation patterns of the prototype across the designed band, two different open end waveguides were used. From 30-40 GHz, an area of 18×18 cm was scanned at a distance 3 cm over the lens using WR28 waveguides. For the higher frequency band (50-60 GHz), WR15 waveguides were used to scan an area of 12×12 cm at a distance of 2 cm from the top of the lens.

The near field was sampled with grid distance $\Delta x = \Delta y < \lambda/2$ at the highest frequency: the scanning step was chosen as 3mm and 2mm for two measuring bands, respectively.

The FF electric field in the direction identified by the angles θ, ϕ can be found from the near field measurements as follows:

$$\vec{E}^{ff}(\theta, \phi) = jk_0 \cos \theta \tilde{G}(\theta, \phi) \vec{M}_{eq}(\theta, \phi) \frac{e^{-jk_0 r}}{2\pi r} \quad (4.9)$$

where \vec{M}_{eq} is the Fourier transform of the equivalent current distribution on top of the lens (related to the measured aperture field), the function \tilde{G} is the spectral domain

dyadic Green's function of free space, k_0 is the wave number and r is radial distance of the observation sphere.

The equivalent current distribution can be derived from the measured S_{21} parameters by applying the equivalence theorem. This 2D distribution consists of both x and y -components, in order to find both co-polar (Co) and cross-polar (Cx) components of the radiated field. From the near field results plotted in Fig. 4.7 for broadside, the main component is 25 dB higher than the orthogonal one, which will result in low Cx in the radiation patterns.

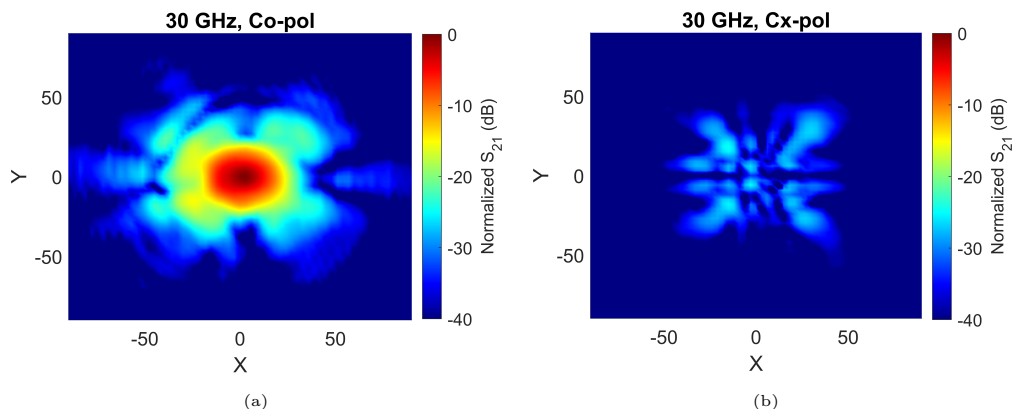


Figure 4.7: Two dimensional near field scan results for (a) Co-pol and (b) Cx-pol at 30 GHz.

In Fig. 4.8, the broadside patterns from simulations and measurements are plotted together for comparison. The measured results present good agreement with the simulation results near the main beam. The side lobe level of the measured results are slightly higher than the one from simulations. The Cx-pol is also shown in the figure, but only for diagonal plane, since it is much lower for the main planes.

For all the measurements evaluating the scanning performance, only the Co-pol component was measured since only the main planes are considered.

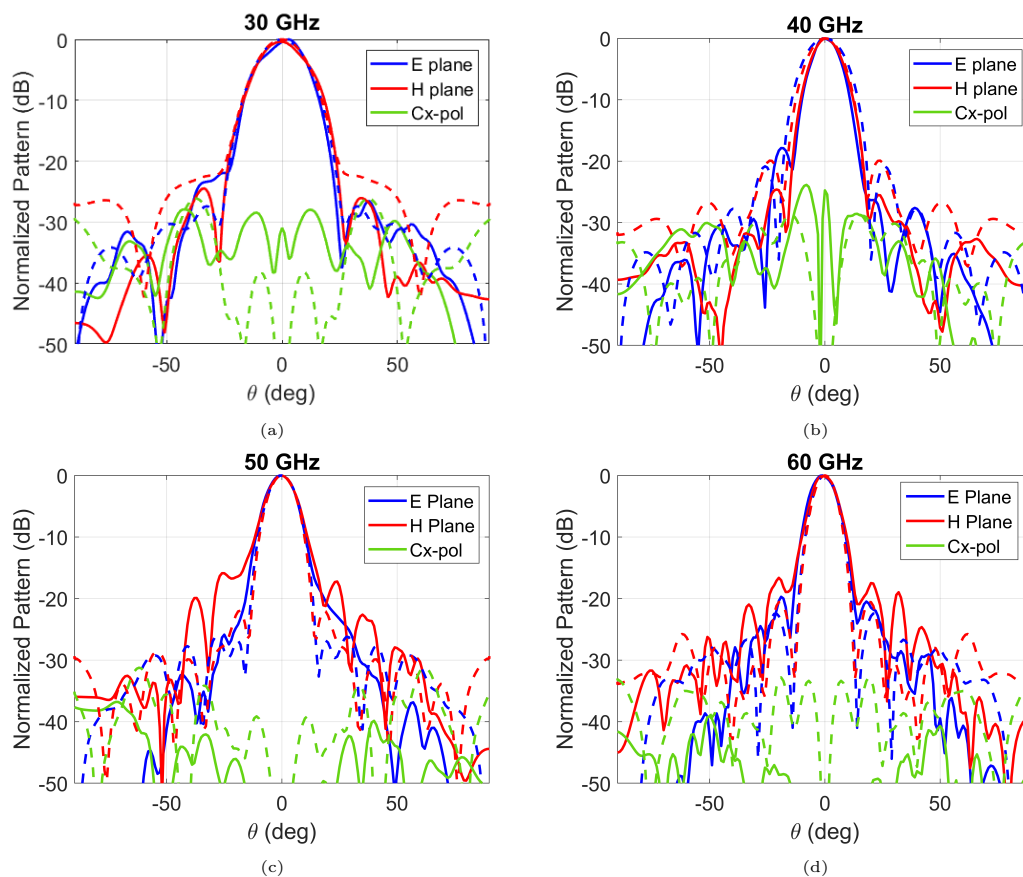


Figure 4.8: Measured broadside patterns in comparison with simulated results at (a) 30 GHz (b) 40 GHz (c) 50 GHz (d) 60 GHz. The solid curves represents the measured results and dashed ones are for simulations.

The measured scan patterns of the lens are shown in Fig. 4.9, normalized to the broadside directivity, to quantify the scan loss. A scan loss following the ideal cosine profile can be observed. A squint of the scan beams can be observed with respect to the nominal pointing angle. This was observed to be due to an alignment error of the waveguide feed with respect to the lens.

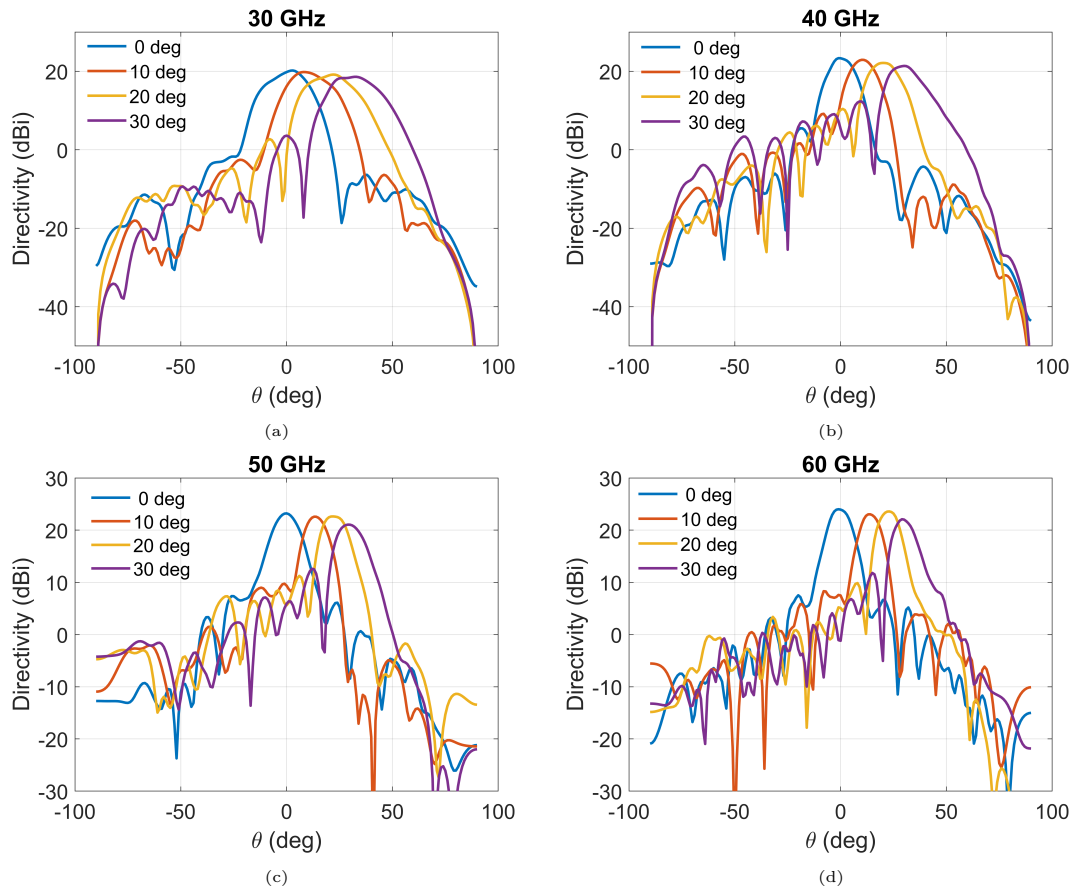


Figure 4.9: Measured results for different scan angles and frequencies.

4.3 Gain Measurement

The realized gain of the flat lens prototype is measured following the procedure discussed in [44]. The open ended waveguide was used instead of the standard gain horn to estimate the gain.

The time-gating technique was applied to eliminate the effect of possible multiple reflections. The measured gain for the open ended waveguides is shown in Fig. 4.10(a) and (b), for the two measured bands, respectively (blue curves). The gain provided in the probe data sheet (green curves) are also plotted for comparison. It can be clearly see that the measured gain is lower than the provided value, especially for the high frequency band. It has to be noted, however, that the measured gain also include the losses of coaxial-to-waveguide adaptor that is not calibrated. To verify this assumption, a measurement of two waveguides, connected back-to-back with their open ends touching, was performed. By adding the losses calculated with this measurements to the gain (red curves in Fig. 4.10), the gain specified by the provider is reconstructed.

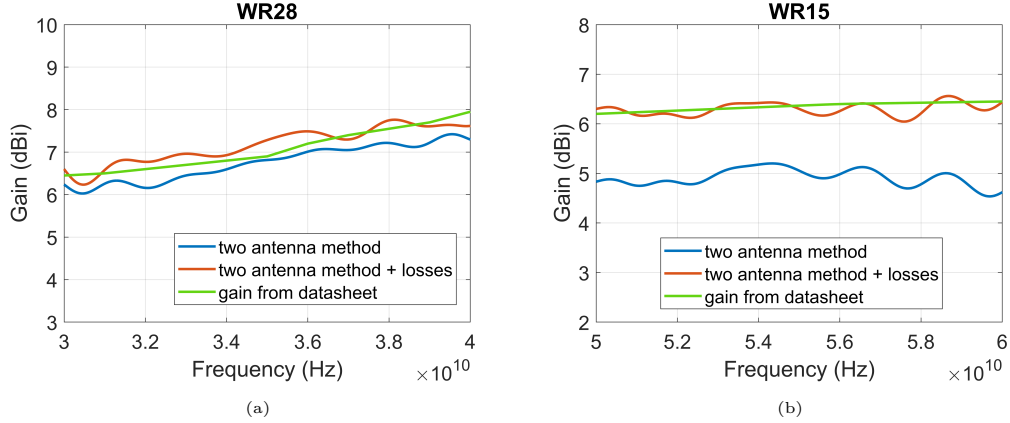


Figure 4.10: The comparisons of measured gains with typical values of (a) WR28 from 30 GHz to 40 GHz and (b) WR15 from 50 GHz to 60 GHz.

4.3.1 Alignment

The broadside measured pattern, for the high frequency band, was squinted by about 4 degrees with respect to the boresight direction. The patterns plotted in Fig. 4.9 are corrected for this tilt. A more in depth discussion is reported in this section. A misalignment of the feed with respect to the lens due to the deformation of the holder was observed. Because of the weight of the cable connected on one side of the adaptor, the waveguide is slightly tilted with respect to the nominal on-axis placement. Simulations of the tilt angles were performed, showing that even 1° tilt of the waveguide results in a 4° shift in the main beam and a drop to up to 0.8 dB in the broadside directivity. This is due to the fact that the waveguide is very long (10cm) and it is attached to the holder at its base, thus a small tilt results in a significant shift of the waveguide open end ($10\text{cm} \times \tan(1^\circ) = 1.7\text{mm}$).

To reduce the error, the drop of the directivity was evaluated by comparing simulations with and without tilt. The pattern is corrected for a certain misalignment by:

$$S_{12\text{corr}}(x, y) = S_{12\text{meas}}(x, y) e^{-jk_0 x \sin \theta_{\text{tilt},x}} e^{-jk_0 y \sin \theta_{\text{tilt},y}}. \quad (4.10)$$

where $\theta_{\text{tilt},x}$ and $\theta_{\text{tilt},y}$ are tilt angles in the two main planes, corresponding to a certain shift of the feed along x and y . For example, the original measured transmitted phase at 60 GHz is plotted in Fig. 4.11a. A linear phase shift in both x and y directions can be seen clearly. If a correction with $\theta_{\text{tilt},x} = -2^\circ$ along x and $\theta_{\text{tilt},y} = 2^\circ$ along y is applied, the flat phase distribution is re-obtained, as the results shown in Fig. 4.11b. The corresponding position of the lens is indicated in dashed curve.

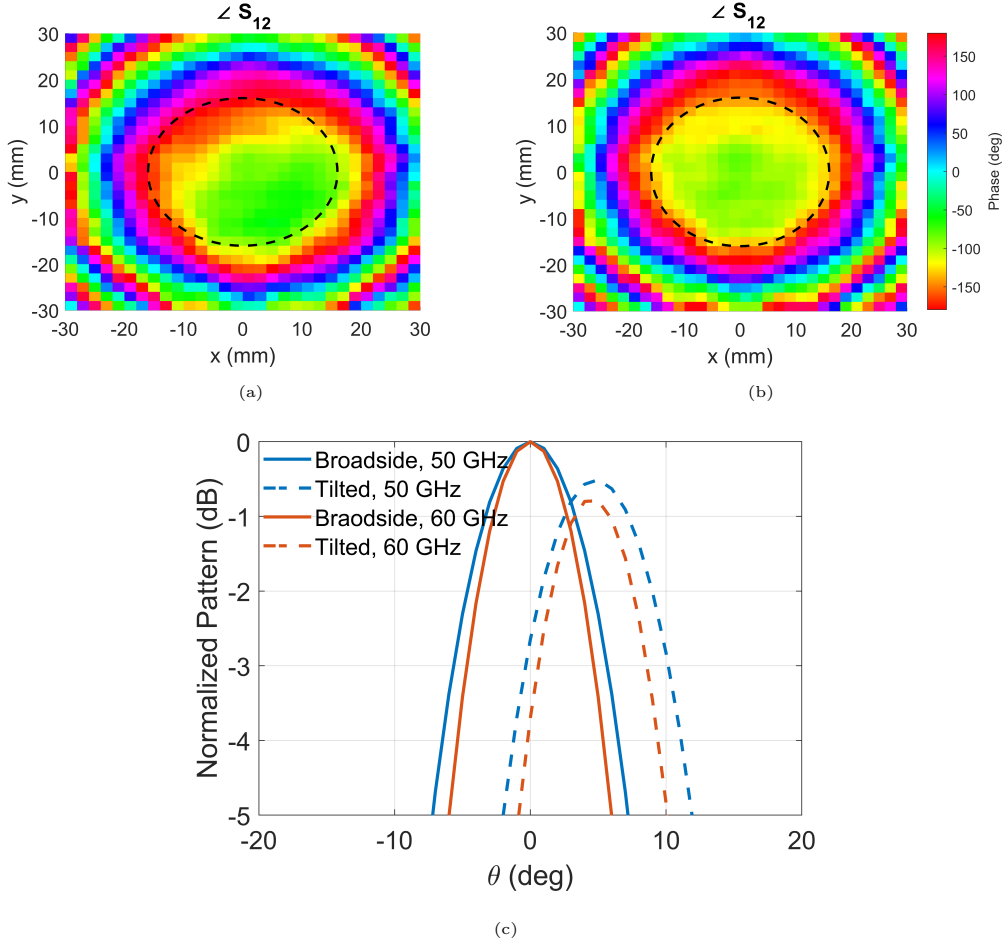


Figure 4.11: (a) The original measured transmitted phase, (b) the measured transmitted phase with misalignment correction at 60 GHz and (c) the directivity decreasing of 1° tilting simulations.

The drop of directivity was evaluated from full-wave simulation results. The maximum directivity difference between the well-aligned system and the one with tilted feed varies from 0.4 dB (50 GHz) to 0.8 dB (60 GHz).

4.3.2 Limited Distance in the Setup

Secondly, limited by the structure of the CNC machine, the maximum separation distance between two waveguides is 28.8mm. The far field condition is $R > 2D^2/\lambda$ is no longer verified when the frequency is higher than 48 GHz. To estimate the effect of this approximation, we calculated the field radiated by a uniform current distribution with the same size of the lens, at the distance used in the measurements. We then compared the beamwidth obtained using the far-field approximation with the result from the general radiation integral valid also in the near field. A small difference in gain is estimated to be up to 0.15 dB at the highest frequency.

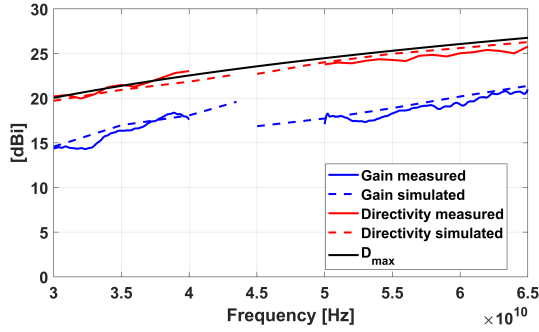


Figure 4.12: Measured and simulated directivity and gain.

4.3.3 Metal Surface Roughness

Another part of the deviations comes from the roughness of the metal, that was originally not included in the lens simulations. Although in the simulations, the losses of the dielectric material and the metal are considered, the metal was simulated as infinitely thin pure copper slab with a conductivity of $\sigma = 5.97 \times 10^7$ S/m to reduce the simulation's complexity. In practice, the metal has a certain thickness ($18 \mu\text{m}$ for inner layers, $36 \mu\text{m}$ for outer layers) and specific surface roughness. This difference was re-evaluated by comparing the simulations of one unit cell, consisting of zero thickness pure copper metal layers, with the one having the realistic thicknesses with the surface roughness as 0.0028 mm (specified in the PCB datasheet). The additional loss due to surface roughness was estimated to be around 0.3 dB for the center unit cell, but will be lower for all the other unit cell which contain less metal.

4.3.4 Comparison Between Measurements and Simulations

With all the corrections being made for the measurements, the final plots for the measured and simulated directivity and gain are plotted in Fig. 4.12. Since different waveguides are used for the measurements in two sub-bands, a drop between the two measured gain can be observed. This can be explained by the reduce of the spillover efficiency when switching to the waveguide with smaller physical aperture (WR15). It can be noted that the measured curves are in fair agreement with the simulations for both directivity and gain.

The breakdown of the different causes of losses earlier presented in Fig. 4.1d highlights that the main difference between gain and directivity is the spillover losses of the waveguide feed. Thus, the good agreement between measured and simulated gain confirms that only a minor contribution of the losses come from Ohmic and reflection losses.

In the following section, more suitable feeds with higher spillover efficiency are briefly discussed.

4.4 Alternative Feeds

From the simulation results with waveguides, it can be seen that although the taper efficiencies are high, the aperture efficiencies are relative low due to the very wide primary patterns. Also, the pattern varies a lot across the bandwidth, resulting in the unstable secondary patterns. Therefore, the performance of the system can be improved with a better feed design. This feed is supposed to have most of its power intercepted by the lens and have frequency independent patterns in the band 30-60 GHz. While the design of an optimized feed was not the focus of this work, a basic study of different feeds was carried out. Two feeds were considered: a conical horn and a 4 by 4 connected slot array.

4.4.1 Conical Horn

A conical horn antenna consists of a cylindrical waveguide and a flared transition is considered, as shown in Fig. 4.14a. The geometrical parameters are chosen to have a maximum -10 dB taper across the lens aperture at the center frequency. The primary patterns of this conical horn are plotted in Fig. 4.13a. Due to the circular aperture of the conical horn, its primary patterns have a good symmetry for E- and H-plane. This symmetry is largely maintained on the secondary patterns (Fig. 4.13b).

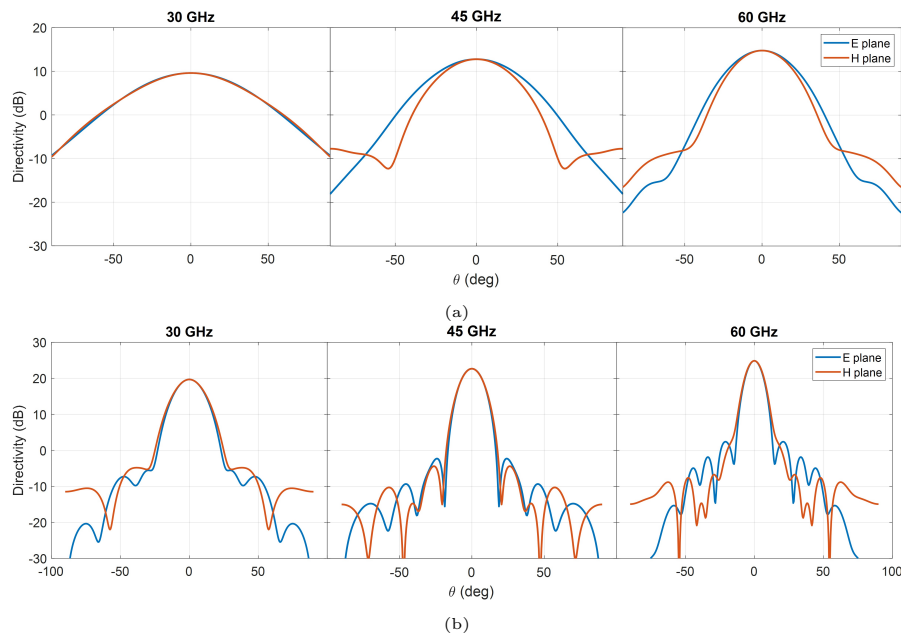


Figure 4.13: (a) The primary patterns of the conical horn. (b) The secondary patterns of lens illuminated by the horn.

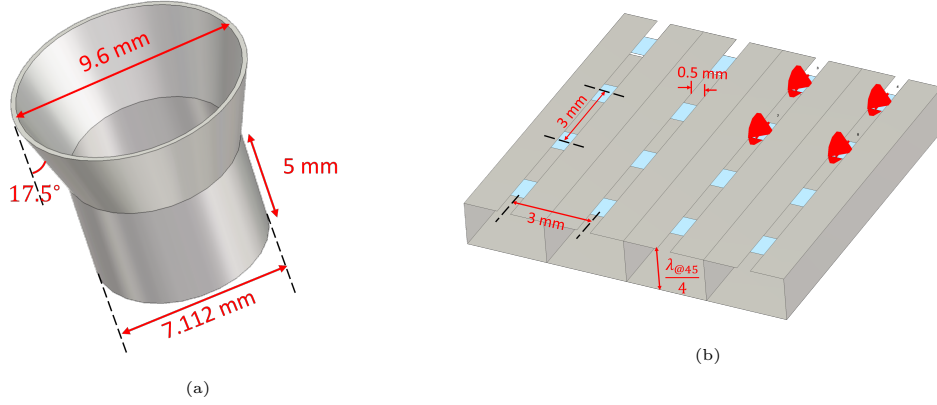


Figure 4.14: (a) Conical horn feed (b) 4 by 4 connected array.

4.4.2 4x4 Connected Array

A connected array antenna was used in [45] to realized a wideband reflector feed. Frequency-independent patterns were obtained from the array by feeding the elements with a quadratic phase distribution and an amplitude taper. The quadratic phase creates a virtual focus at a certain distance from the array, keeping the beamwidth of the primary pattern less dispersive with the frequency. If the quadratic phase is obtained with true-time delay lines, the position of the virtual focus does not change with the frequency. The amplitude taper was used to reduce oscillations in the patterns. The same idea is used here for a small array of 4 by 4 elements, to illuminate the lens under consideration.

The 16-port connected array shown in Fig. 4.14b is designed and simulated. Each port of the array is stimulated with different amplitude and phase. The matrix for the amplitude taper and phase delay for the excitation is generated by the production of the excitation array along the x - and y -directions. To find the optimal set of excitation parameters, an optimization process is implemented by minimizing the cost function, which is defined as the difference at three difference frequency (30, 45 and 60 GHz) for both E- and H- planes with an ideal frequency independent Gaussian beam. The amplitude and phase excitations are defined as follows:

$$\text{amp} = \begin{bmatrix} A_x A_y & A_y & A_y & A_x A_y \\ A_x & 1 & 1 & A_x \\ A_x & 1 & 1 & A_x \\ A_x A_y & A_y & A_y & A_x A_y \end{bmatrix}$$

$$\text{phase} = \begin{bmatrix} -(L_x + L_y)k_0 & -L_y k_0 & -L_y k_0 & -(L_x + L_y)k_0 \\ -L_x k_0 & 0 & 0 & -L_x k_0 \\ -L_x k_0 & 0 & 0 & -L_x k_0 \\ -(L_x + L_y)k_0 & -L_y k_0 & -L_y k_0 & -(L_x + L_y)k_0 \end{bmatrix}$$

where A_x, A_y are the amplitude taper parameters of excitation and L_x, L_y refer to the extra feeding length of the true-time-delay lines used for the quadratic phase implementation. In this work, the optimized feeding parameters are defined by $A_x = A_y = 0.6$ and $L_x = L_y = 0.8\text{mm}$.

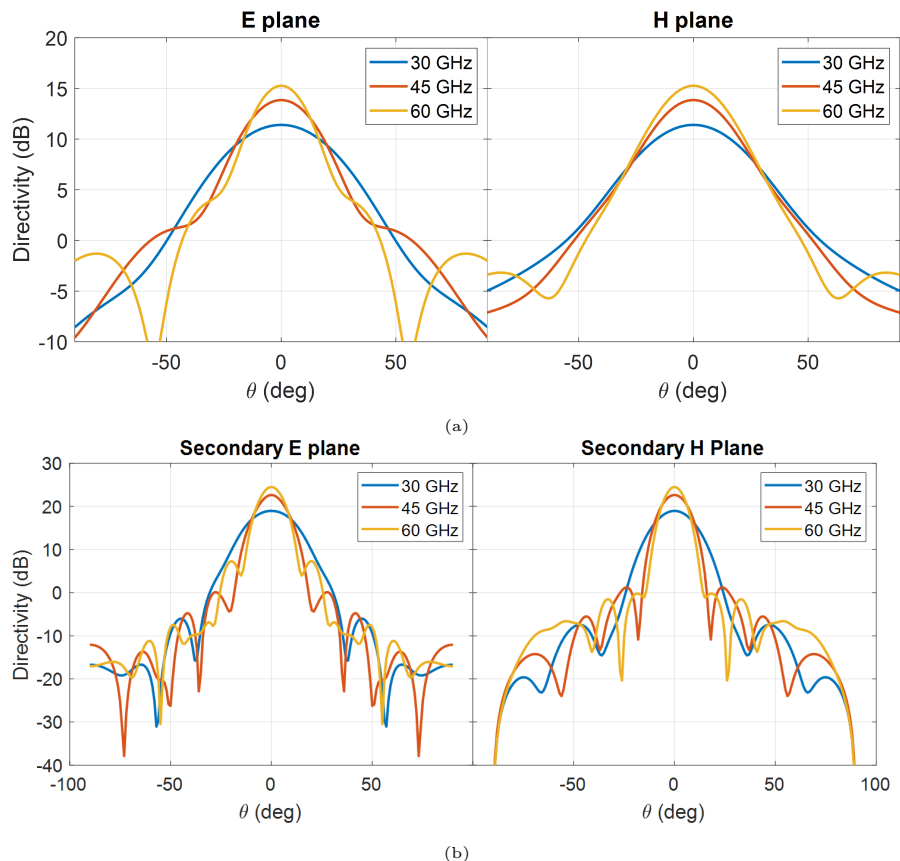


Figure 4.15: (a) The primary patterns and (b) secondary patterns of E and H plane for lens illuminated by the 4×4 connected array

The primary patterns from the connected array feed are shown in Fig. 4.15a. It can be noticed that the directivity of these patterns for an octave bandwidth varies of about 4 dB, which is 2 dB less than the conical horn. The secondary patterns for the connected array feed are plotted in Fig. 4.15b.

The extracted efficiencies for the two alternative feed discussed above can be seen in Fig. 4.16. It can be observed that both feed concepts provide higher efficiency compared to the open-ended waveguide, mainly due to the reduced spillover. The horn reaches higher total efficiency at frequency above 40 GHz, but it is slightly worse at 30 GHz because of the larger primary pattern. The connected array provides more stable efficiency across the octave bandwidth, higher the 60%.

The phase center is an imaginary point where the incoming signal are focused or the origin of the EM wave propagates spherically outwards. The feed should be placed to

ensure its phase center is located at the focal point. Generally, the aperture center is regarded as the phase center of waveguides. However, the phase center of a horn antenna is somewhere in between the throat to the aperture and is frequency dependent. It is fair to note that the implementation of the amplitude and phase distribution for the connected array would require a feeding network that would generate additional Ohmic losses. The design of a low-loss feed network based on parallel plate waveguides goes beyond the scope of this thesis and is left for a follow-up study.

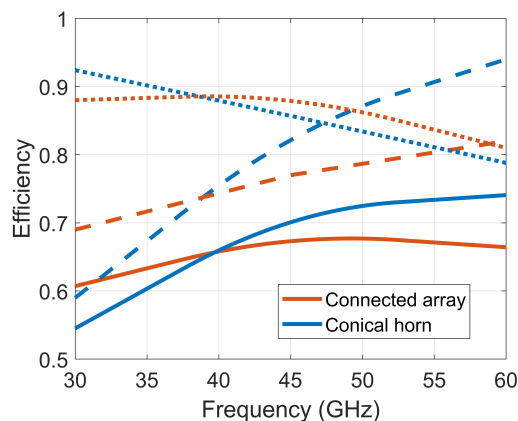


Figure 4.16: Efficiencies for the conical horn and 4x4 connected array, where the dashed curves represent η_{so} ; dotted curves stand for η_t ; solid curves refer to η_{ap} .

Chapter 5

Other GRIN Lens Designs

Despite the focus of this thesis was on the design and experimental validation of a collimating flat lens, some other GRIN lenses following the design equations in Chap. 2 have been investigated and synthesized with the ADL structure. Two different examples of lens designs are illustrated in this chapter by means of simulations: a flat core lens transferring spherical waves across different media and a flat Fresnel zone lens.

5.1 Flat Lens for 140-170 GHz Core-Shell Lens System

The core-shell lens is an optical system consisting of a smaller core lens surrounded by a larger shell lens with different optical properties. The core lens is co-designed together with the feed to control the primary pattern illuminating the larger lens.

Such a system with a bandwidth of 140-170 GHz is presented in [46], where the core lens functions as a transition between different media. It has a spherical shape for reducing the influences on the patterns, with a matching layer on top of it to reduce the reflections. The main idea in [46] is depicted in Fig. 5.1a and consists in placing a small high permittivity lens in the vicinity of the feed to exploit the leaky wave nature of the feed and to enhance the feed radiation performance. However, the high permittivity material would not be suitable for the large dielectric lens that is used to achieve high directivity. Such a material would have high cost and high reflections at the top interface. For this reason a transition between the electrically dense material of the small lens ($\epsilon_r = 12$) and a lower permittivity ($\epsilon_r = 2.3$) for the larger lens is realized. The large lens is then made of low-loss and low-cost plastic material, which is convenient for mmWave applications.

One limitation of the design proposed in [46] is that the interface between the core lens and the shell lens is curved, which increases the manufacturing complexity, since the two curved surfaces need to be very accurate to avoid air gaps. Moreover, also the matching layers needs to be curved and accurately manufactured to avoid air gaps between the matching layer and the plastic lens. The original core lens has a diameter of 3.91mm and $F = 2.75$ mm. At the interface between the core lens ($\epsilon_r = 12$) and the larger plastic lens ($\epsilon_r = 2.3$), a matching layer with relative permittivity of 5.2 is

considered. The lens is manufactured as a spherical surface above a slab with thickness 1.34mm.

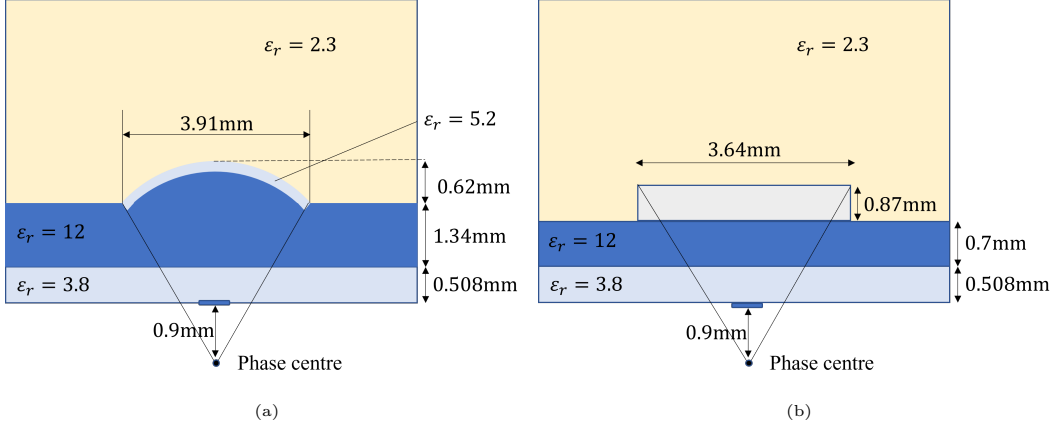


Figure 5.1: (a) Geometry of original core-shell lens and (b) geometry of flat-core shell lens.

5.1.1 Lens Design

Here, a flat GRIN lens is proposed to replace the spherical lens for the mentioned application. For the design we assume $\varepsilon_{r,\text{host}} = 7$, $\varepsilon_{r,\text{in}} = 12$, and $\varepsilon_{r,\text{out}} = 2.3$. The maximum permittivity is set to be around:

$$\varepsilon_{r,\text{max}} \approx \frac{\varepsilon_{r,\text{host}}^2}{\varepsilon_{r,\text{out}}}, \quad (5.1)$$

so that part of the host material can also be used as a quarter-wavelength matching layer at the center frequency above the lens. An analysis of the minimum thickness of the slab below the GRIN lens was performed. Because this slab is now flat, it can be realized as a flat silicon slab. It was observed that the slab's thickness could be reduced to 0.7mm or even 0.5mm without significant loss of performance, while simplifying the GRIN lens design. Therefore, the new focal length decreases to 2.1mm. The diameter of the flat lens is 3.64mm to have a similar subtended angle as the original design. The results shown in Fig. 5.2a is the lens designed followed the procedure presented in Chap. 2. This lens has a maximum permittivity $\varepsilon_{r,\text{max}} = 22$ and a thickness of 0.87mm. Considering the manufacturing limitations, the thickness of the lens core was adjusted to be integer multiple of the minimum internal layer thickness, where Low Temperature Co-fired Ceramic (LTCC) was considered as suitable fabrication technology.

Fig. 5.2b shows the ray tracing on the fine tuned designed with $\varepsilon_{r,\text{max}} = 22$ and $T_{\text{core}} = 0.7\text{mm}$. The thickness of the matching layer is adjusted to 0.17mm. An example elliptical shell antenna with a diameter of $15\lambda_0$ is designed using the geometrical optics / Fourier optics (GO/FO) tool developed in [47], and simulated with the adjusted flat lens. The ray tracing simulation of the whole system is displayed in Fig. 5.2c.

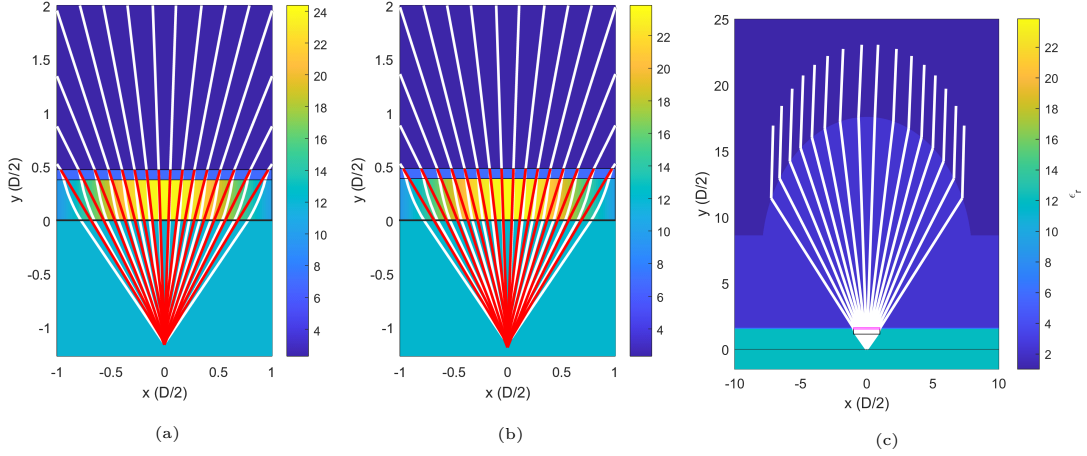


Figure 5.2: Ray tracing simulations for flat core lens of (a) initial design, (b) adjusted design and (c) design with the outer shell lens.

5.1.2 ADL Synthesis

The ADL has to be designed to achieve the maximum permittivity of the core $\varepsilon_{r,\max} = 22$. The period of the ADL patches $p = 0.28\text{mm} = 0.14\lambda_0$, where λ_0 is the wavelength in free space. Fig. 5.3a shows the effective permittivity realized as a function of internal layer distance at the center frequency with fixed p . Fig. 5.3b represents how dispersive the ADL is, by plotting the variations of effective permittivity across the band. The distance between layers is selected as 0.1mm so that the ADL structure can have an appropriate permittivity and also avoid being too dispersive from 140 to 170 GHz.

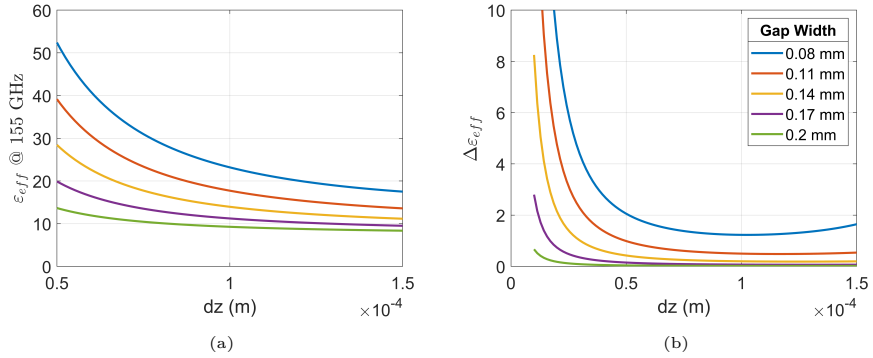


Figure 5.3: (a) Maximum relative permittivity realizable and (b) variation of permittivity across the band.

The lens designed as continuous varying permittivity distribution can be divided into 13 unit cells given the period. The permittivity sampled at the center of these unit cells can be mapped to the gap width needed for the ADL structure to synthesize this permittivity value. The sampled permittivity and the mapping with gap width are shown in Fig. 5.4

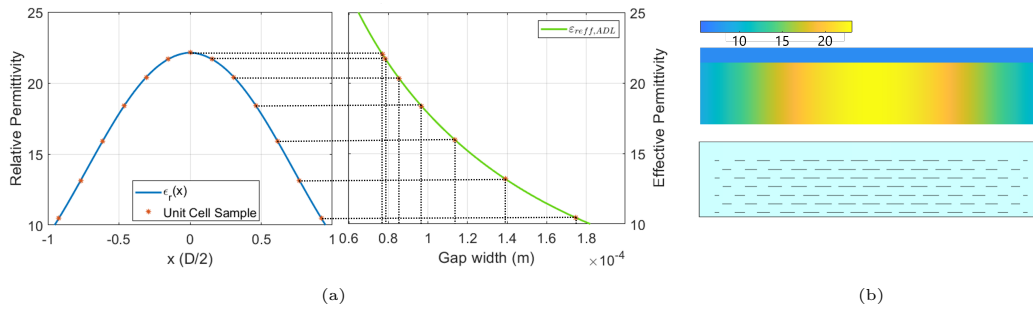


Figure 5.4: (a) GRIN lens core permittivity discretization and (b) cross-section of the ADL realized GRIN lens.

With this lookup table established, seven different unit cells (symmetrical design) are designed. To verify whether the design is well-matched through the band as expected, the S_{11} of the center unit cell is plotted in Fig. 5.5a based on the equivalent circuits of ADL. This unit cell is chosen due to its largest dielectric contrast and transformer ratio of the matching layer (from $\epsilon_r = 22$ to $\epsilon_r = 7$).

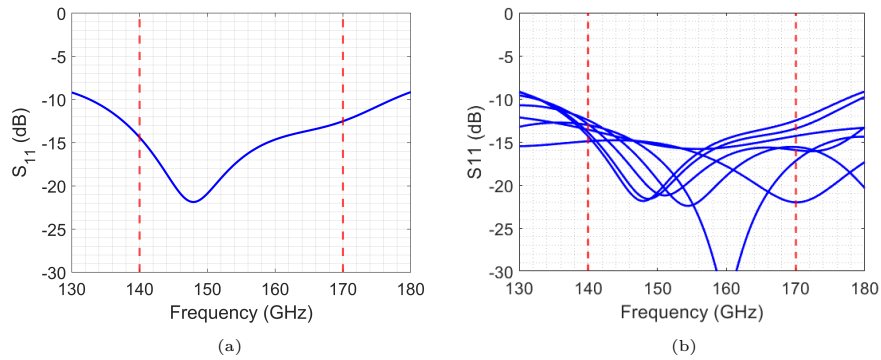


Figure 5.5: Reflection coefficients S_{11} of (a) the center unit cell and (b) all unit cells.

The reflection coefficients of all unit cells are also plotted in Fig. 5.5b. It is noticeable that the reflection coefficients are all below -10 dB across the target band. The 3D lens is built by combining all these unit cells and relating each unit cell with its radial distance to the lens center. The final flat core lens has seven metal layers (the structure is shown in Fig. 5.6).

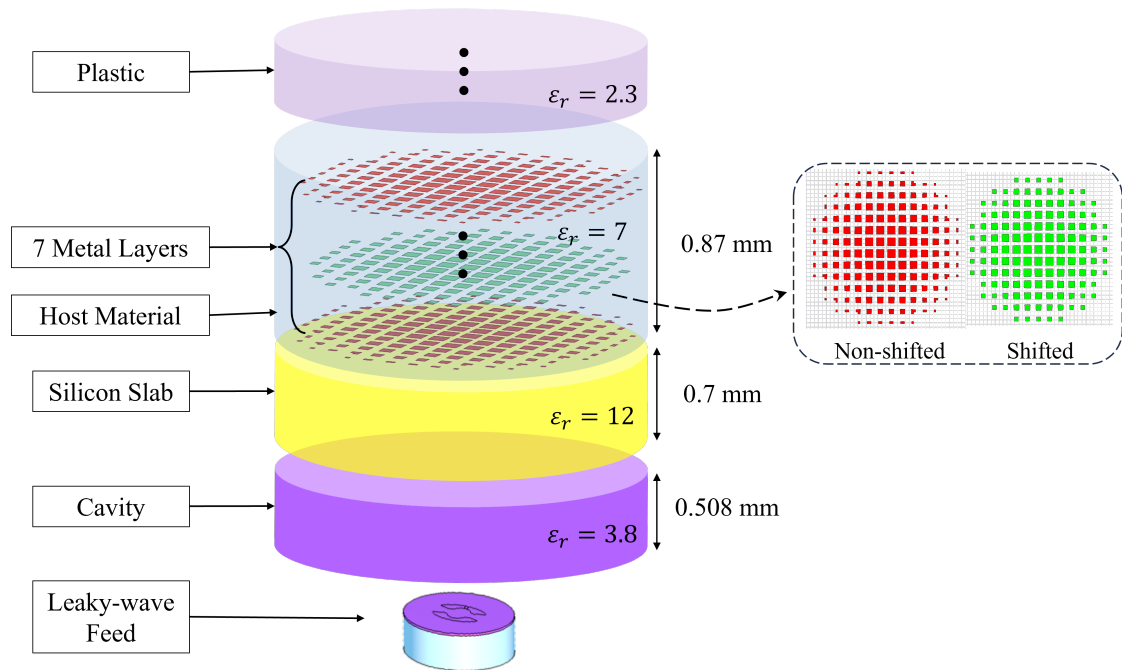


Figure 5.6: Flat core lens structure.

Each metal layer has the maximum shift with respect to the adjacent layer to decrease the total thickness. The cross-section of the ADL-implemented lens is shown in Fig. 5.4b.

5.1.3 Simulation Results

The radiation patterns of the complete flat-core shell lens antenna were simulated in CST Microwave Studio. The comparisons between the far field patterns for both E- and H-planes at three frequency points of the curved original design and the flat ADL-realized design are plotted in Fig. 5.7. The patterns are calculated considering a semi-infinite medium above the flat lens with the same permittivity of the large shell lens. It can be observed that the flat lens design has radiation patterns very close to the original design through the band, for both E and H plane.

Also, the patterns are relatively stable in terms of beamwidth for all frequencies, as shown in Fig. 5.8a. This property results in an efficient and wideband illumination of the larger plastic lens. The map of the E-field magnitude at 155 GHz on a vertical plane crossing the lens is plotted in Fig. 5.8b. It can be observed that both the input and output fields from the lens behave like spherical waves, but with different wavenumbers.

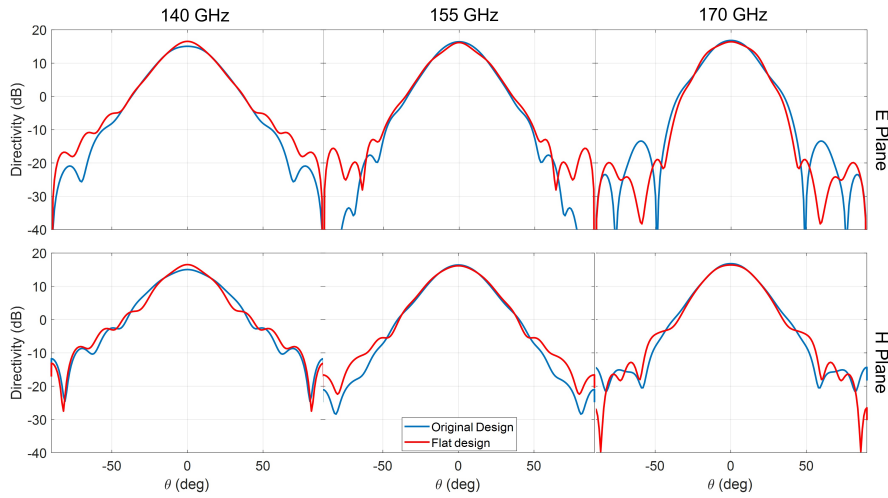


Figure 5.7: Pattern Comparisons.

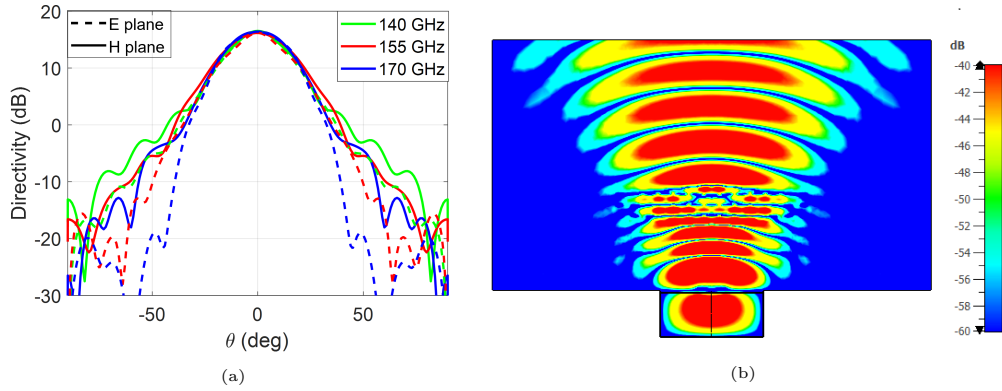


Figure 5.8: (a) Far field patterns of flat core lens and (b) simulated E field at 155 GHz.

5.1.4 LTCC Realization

LTCC (low temperature co-fired ceramic) is an advanced technology used in the electronics and telecommunications industry for manufacturing multi-layered ceramic circuits and components. LTCC technology offers several advantages over traditional methods, making it popular for various applications. The key features and advantages of LTCC technology include:

- **High Frequency Capability:** LTCC materials offer excellent electrical properties at high frequencies, making them ideal for RF circuits and devices. They have low dielectric losses, high Q factor, and good signal propagation characteristics, allowing for efficient RF signal transmission and reception.
- **Miniaturization and Integration:** LTCC enables the miniaturization of RF components and circuits due to its multi-layer capability. By stacking multiple

layers of conductive and dielectric materials, complex RF structures can be designed and integrated into compact packages, saving space and improving overall system performance [48].

- **Wide Frequency Range:** LTCC technology supports a wide range of operating frequencies, from a few megahertz to sub terahertz, making it suitable for various RF applications across different industries.

The typical dielectric constant for LTCC substrate materials range from 6 to 10. The minimum thickness of internal layer reach until $25\ \mu\text{m}$ and can have a multi-layer structure of up to 40 stacks.

The DuPont™ Green Tape™ 951 is a low-temperature cofired ceramic tape that can offer the corresponding layer thickness and a dielectric constant around 7 [49]. Part of the physical and electrical properties of these lamination substrate boards are shown in Table 5.1. The designed lens can be realized with the structure below Fig. 5.9

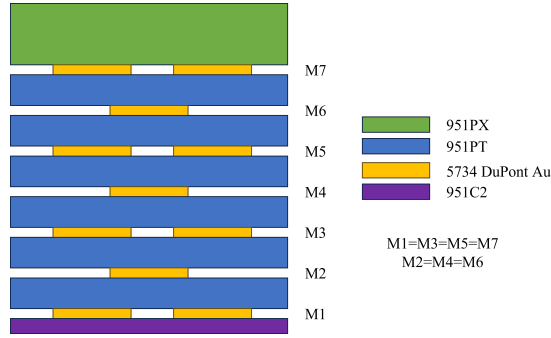


Figure 5.9: Flat core lens stackup design based on LTCC.

Tape Product	Unfired Thickness	X,Y Shrinkage	Surface Roughness	ϵ_r	Loss Tangent
951C2	$50 \pm 3\ \mu\text{m}$	$13.0 \pm 0.2\ \%$	$<0.34\ \mu\text{m}$	7.8 ± 0.2	0.006 (@ 3 GHz)
951PT	$114 \pm 8\ \mu\text{m}$	$12.7 \pm 0.3\ \%$		(@ 3 GHz)	
951P2	$165 \pm 11\ \mu\text{m}$			7.5 ± 0.2	
951PX	$254 \pm 13\ \mu\text{m}$			(@ 10 GHz)	

Table 5.1: DuPont™ green tape™ 951 specifications.

5.2 Flat Fresnel Zoned Lens at 7 THz

In some applications at very high frequency (7 THz), the frequency band of operation can be given up to gain in terms of reduced cost and complexity. For example, THz superconducting detectors operating at this frequency do not require a large bandwidth, but would benefit enormously by a more accurate process to manufacture the lenses. A

flat lens could be realized with Electron beam processing, that is much more accurate in terms of alignment and precision with respect to curved lens surfaces.

One way to limit the complexity is by limiting the number of metal layers of the GRIN lens. This results in a lens that is no longer true time delay, but implements a Fresnel zone lens with 2π phase jumps at the interface with the adjacent zone lens, as shown in Fig. 5.10a. Therefore, the size of each zone lens is determined by the phase to compensate. To have the flat equi-phase plane, the phase needed to be compensated with respect to the radial distance x can be expressed as:

$$\Delta\varphi = k_0 n_{\text{in}} \left(\sqrt{F^2 + x^2} - F \right), \quad (5.2)$$

where $k_0 n_{\text{in}}$ represents the wavenumber in the lower medium. If one considers a lens with $F/D = 1$ with silicon ($\varepsilon_r = 12$) below, the phase variation versus the incident angle is plotted in Fig. 5.10b.

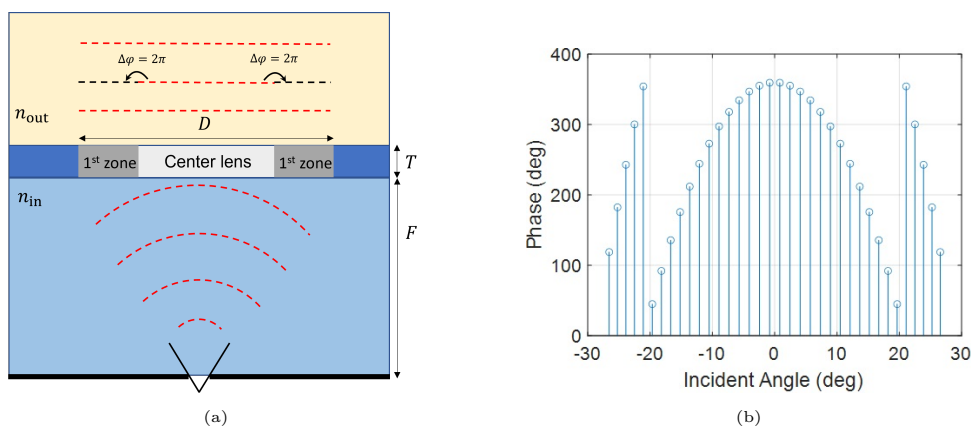


Figure 5.10: (a) A graphic illustration of Fresnel zone lens. (b) Phase variation on the lens with respect to incident angle.

However, this come at the cost of a narrow bandwidth because the point at which the phase wraps is frequency dependent, meaning that at other frequencies this jump happens at the different position and a phase error is introduced.

5.2.1 Lens Design

The position where the phase is wrapped is the boundary between two lens zones. If the focal length of such scenario is $175 \mu\text{m}$, the diameter of the center lens is $125 \mu\text{m}$ and $25 \mu\text{m}$ for the first zone lens. The flat Fresnel zone lens is assumed to located between silicon and free space, with a thin layer of parylene ($\varepsilon_r = 2.62$) as the matching layer between the lens and free space. The lens is designed to operate at 7 THz with SiC or SiNx ($\varepsilon_r \approx 8$) as the host material for ADL patches. The centre lens is identical as a collimating lens. The operation bandwidth of this lens is quite narrow due to the phase wrapping. The thickness of the lens will be $15 \mu\text{m}$ if $\varepsilon_{r,\text{max}} = 35$ for the center lens.

To avoid too much energy being reflected due to mismatch, a quarter-wavelength impedance transformer is designed for matching silicon to core lens. This defines the thickness as $2.4\mu\text{m}$ and $\varepsilon_{r,\text{max}}$ as 20.5 of the lower matching layer. For matching the lens core to the parylene thin film and free space, a two section impedance transformer is applied. The structure of the lens is shown in Fig. 5.11. The total thickness of the lens to design is $20.1\mu\text{m}$.

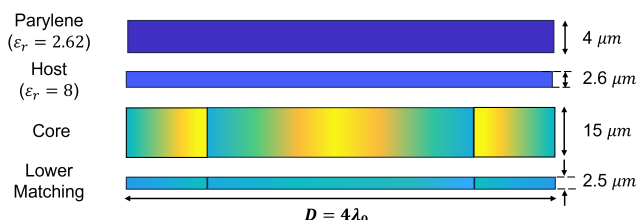


Figure 5.11: Zone lens structure.

Different from previous designs, the distribution of permittivity (shown in Fig. 5.12a) is not continuous at the boundaries between the center lens and first zone lens, the ray tracing simulations are carried out on the center and zone lenses separately. The combination paths of ray is shown in Fig. 5.12b.

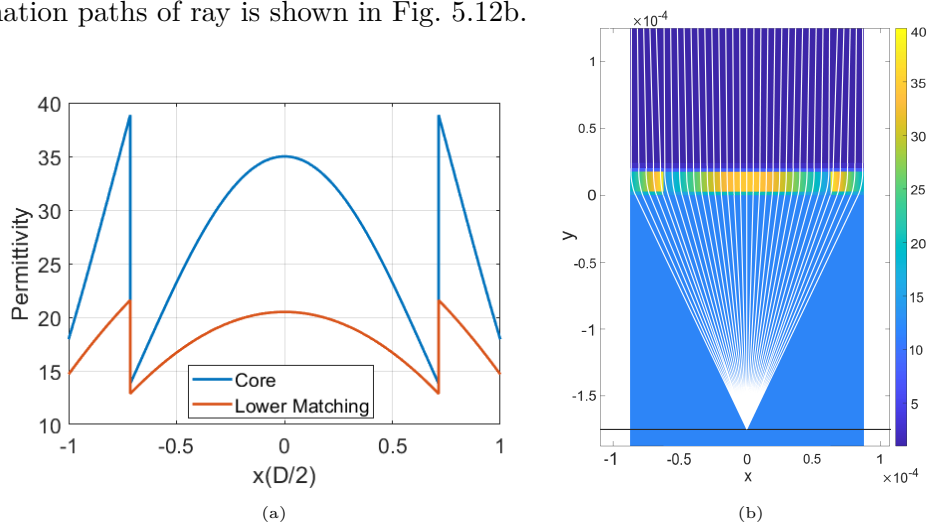


Figure 5.12: (a) Distribution of permittivity. (b) Ray tracing simulations.

5.2.2 ADL Synthesis and Simulation Results

Taking into account for the need for high maximum permittivity and the compact size, we chose the period of the ADL as $p_{\text{ADL}} = 5\mu\text{m}$ and the interlayer distance as $d_z = 2.5\mu\text{m}$. This gives a minimum $0.5\mu\text{m}$ gap width between patches, that can be realized with electron-beam lithography. The whole lens is discretized into 35 unit cells and 7 layers. The top view of the central row of each layer is shown in Fig. 5.13.

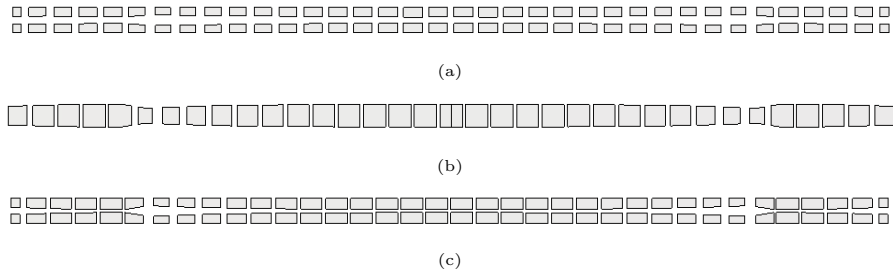


Figure 5.13: The top view of the central row of metal patches for the (a) matching layer (b) non-shifted core layer (c) shifted core layer of the Fresnel zone lens.

To make simulation faster, only a slice of the lens is simulated (2D geometry) assuming a periodic boundaries in the other dimension. A waveguide feed, with an aperture size of $22\mu\text{m}$ by $5\mu\text{m}$ offering 48° of -10 dB beamwidth and 91.5% of spillover efficiency is used to illuminate the lens. In Fig. 5.14a, the full-wave simulated phase variation cross the lens is plotted. A flat phase front can be observed on the transmitted side of the lens.

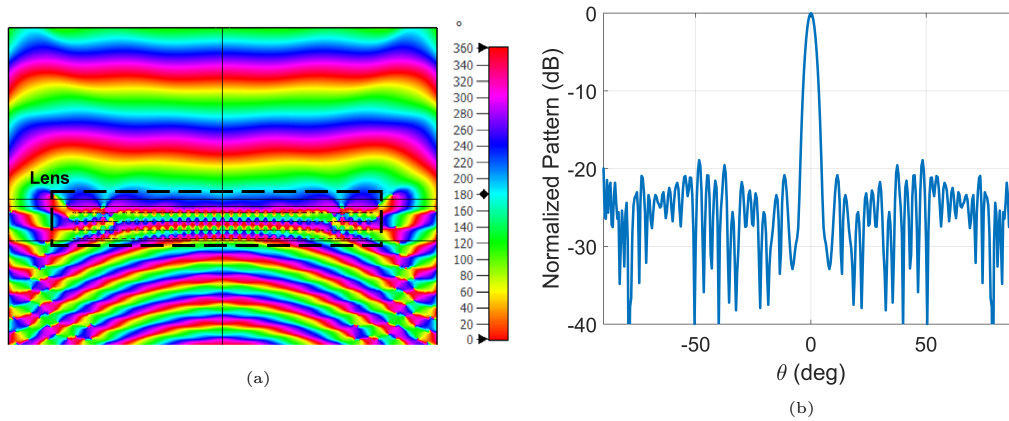


Figure 5.14: (a) Phase distribution and (b) far-field pattern simulated at 7 THz with periodical boundary conditions.

Chapter 6

Conclusion and Future Work

6.1 Conclusion

In this work, artificial dielectric flat lenses were investigated, including different aspects of analysis, design, and experiments.

Design equations for different type GRIN lenses were derived, to achieve transmitted wavefronts with arbitrary linear or quadratic phase profiles. The method provided is semi-analytical, based on closed form expressions of the optical path through the GRIN lenses, and analytical or numerical solutions for all the lens parameters, to find the refractive index distribution.

Once the desired refractive index profile is obtained, ray tracing is used to validate the design and fine-tune the lens to include matching layers. Finally the synthesis of artificial dielectric layers (ADLs) that implement the desired permittivity distribution is performed, based on techniques that were available in the group from prior work.

To verify the design procedure, a wideband (30-60 GHz) collimating GRIN lens in free space based on ADLs is designed. The lens is designed to have a diameter of $6\lambda_0$, with an overall thickness of $1\lambda_0$ at the highest frequency and an F/D equal to 0.67. The continuous varying permittivity profile is discretized and realized by ADLs. Two sections of impedance transformer are applied to match the center permittivity $\epsilon_{r,\max} = 22$ to free space. The simulated S_{11} based on the transmission line model shows reflection coefficients lower than -10 dB across the aperture. The outer matching layer, which has a lower permittivity than the host material, is realized by perforations to achieve an effective permittivity of 2. The lens design was validated with extensive simulations, showing wide bandwidth and high efficiency.

The lens was tested with a simple feed (open end waveguide) to demonstrate the intrinsic performance on the lens. The simulation results showed the effective spherical to planar phase front conversion, with a taper efficiency $> 90\%$, low Cx-pol (around -20 dB normalized to Co-pol maximum), low side lobe (less than -15 dB) and high directivity (max 25.5 dB). With the choice of the waveguide feed, high spillover losses are obtained but two possible feeds were briefly investigated, that could achieve an overall aperture efficiency around 60% across the entire band.

Based on this design, a prototype was manufactured and measured with two different open-ended waveguides in two sub-bands. The radiation patterns were measured by near field to far field transformation. Broadside and three scanning patterns were measured. The misalignment between the feed and the lens due to the deformation of the 3D printed holder is corrected by adding a corresponding phase shift to the measured aperture field and compensating for the directivity drop estimated with from-full wave simulations (with and without tilt). The gain of the prototype is also measured, showing good agreement with simulations.

Different GRIN lens designs were also carried out, manipulating the wave in different ways. A flat lens is designed to replace the curved core lens of a core-shell antenna in sub-THz band (140-170 GHz). Both ray tracing and full-wave simulation were presented. They demonstrated the implementation method achieves almost identical performance as the original design, based on a curve lens. As another application example, a flat Fresnel zone lens operating at 7 THz, which compensates for the phase difference of the incident field by phase wrapping, is designed and simulated. Although the abrupt changes of the track width introduce some errors because of the broken periodicity of the ADL patches, a flat phase front can be observed in the full wave simulation results.

The presented design method is based on simple MATLAB codes and was implemented in a graphical user interface (GUI) to aid different designs in the future.

6.2 Future Work

One of the aspects that was briefly discussed but can be further investigated is the design of the feed. A wideband lens design is useful only if combined with a feed that can illuminate the lens efficiently across this wide bandwidth. The design of an optimized feed could be the scope of a follow up study, to improve the aperture efficiency above 60%. An optimal feed should ensure frequency invariant patterns with flat-top characteristics and stable phase center with the frequency range.

Possible solutions for wideband feeds can be realized with conical corrugated horn antennas [50] or double-ridge horn [51] (see Fig. 6.1a and Fig. 6.1b). Also a small array with quadratic phase illumination could be further investigated for the same purpose [45]. Other wideband feed based on small lenses could be used, such as the connected-array-fed hyper-hemispherical lens introduced in [52], which achieved stable patterns for a 3:1 band (see Fig. 6.1c), or the hemispherical lens fed with corrugated waveguide feed proposed in [53] as shown in Fig. 6.1d.

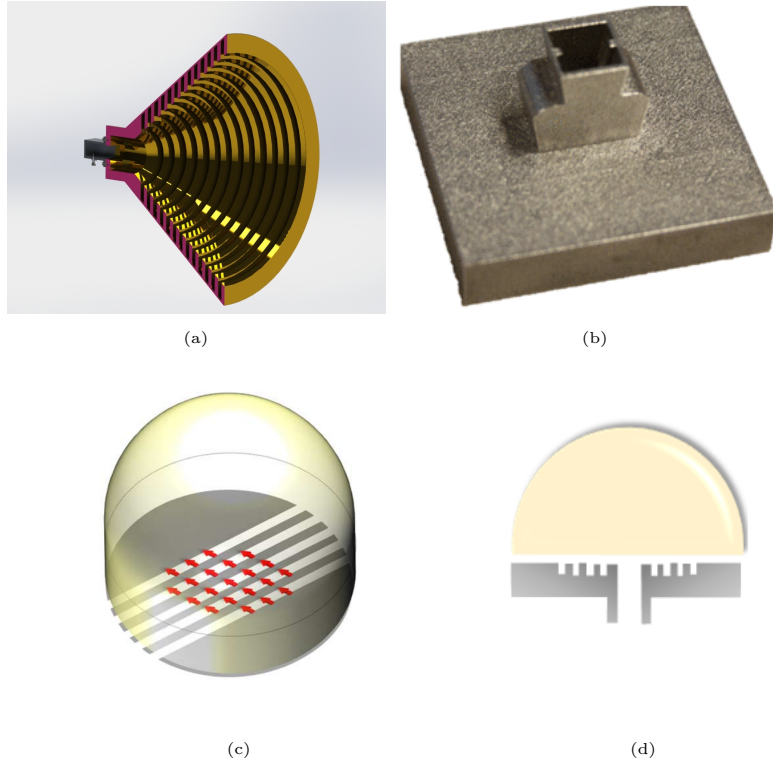


Figure 6.1: (a) Cross section of the corrugated conical horn antenna (Image credit: GrabCAD Community). (b) 3D-printed double-ridges horn. (c) Connected-array-fed hyper-hemispherical lens. (d) Hemispherical lens fed with corrugated waveguide.

Secondly, more studies can be made on the design equations, especially for the case with the matching layers. One can also take the ray paths and phase variations within the matching layers into the total phase variations to optimize the design with specific type of matching layers. Therefore, instead of shrinking the core thickness, a more rigorous design including the matching layers can be realized to optimize the performance.

Moreover, with the given closed-form expressions for the optical path integration inside the GRIN lens, more applications based on GRIN lens can be explored to shape the transmitted wave. A better algorithm for finding the mappings between the incident and transmitted angles for different scenarios could be found, especially for the area near the lens center and edges that are more critical for the ray tracing.

The measurement setup for the prototype can also be improved by applying better methods to ensure the alignment and avoid unwanted inaccuracies. A more stable and adjustable holder could be used to mitigate this problem. A more accurate evaluation of gain can be realized by using the standard gain horn antennas instead of the open-ended waveguides. Cleaner pattern measurements would be possible if the prototype is measured in an anechoic chamber, with absence of reflections from the environment.

Last but not least, more efforts can be made to improve the GUI's performance. The execution speed of the GUI is relative slow, especially for the optimization part, which

finds the best set of parameters for additional phase shift to compensate the deviations due to the presence of matching layers. The data can be better assigned for slicing so that the parallel computations can be applied (or implement the equations optimized for matching layer, which is also the possible future works). It might be interesting to find a better way for retrieving the permittivity distribution to avoid doing interpolations after solving the design equations at certain sampled points, which is the present approach.

Appendix A

Steps for Finding Optical Path Integration

The following derivations are based on the work of [15], but are extended for more general applicability to different GRIN lens designs.

To find the distribution of permittivity across the lens, a closed-form expression for the integration term is needed. with reference to Fig. A.1, considering a small section of arc ds on the ray's trajectory within the lens, according to Pythagoras theorem, one can write:

$$ds = \sqrt{dx^2 + dz^2} = \sqrt{1 + \left(\frac{dz}{dx}\right)^2} dx. \quad (\text{A.1})$$

Therefore, the original integration along the arc can be transformed into the integration on x under Cartesian coordinate system:

$$\int_{P_1}^{P_2} nds = \int_{x_1}^{x_2} n \sqrt{1 + \left(\frac{dz}{dx}\right)^2} dx. \quad (\text{A.2})$$

It can be noticed that, inside the lens, since the refractive index only varies in a continuous manner along x , the Snell's law is verified at every vertical interface between infinitesimal regions. This can be expressed as

$$n(x) \cos \phi = \text{Constant} \quad (\text{A.3})$$

(A.3) is valid for every position inside the lens, including both upper and lower boundaries. Therefore, the value of this constant can be found by applying (A.3) on the boundaries (at the points P_1 and P_2):

$$n_1 \cos \phi_1 = n_2 \cos \phi_2 \quad (\text{A.4})$$

where n_1 and n_2 denote the refractive index at x_1 and x_2 respectively. Similarly, the Snell's Law can be applied on these positions for the horizontal interfaces:

$$n_1 \sin \phi_1 = n_{\text{in}} \sin \theta_{\text{in}} \quad (\text{A.5a})$$

$$n_2 \sin \phi_2 = n_{\text{out}} \sin \theta_{\text{out}}. \quad (\text{A.5b})$$

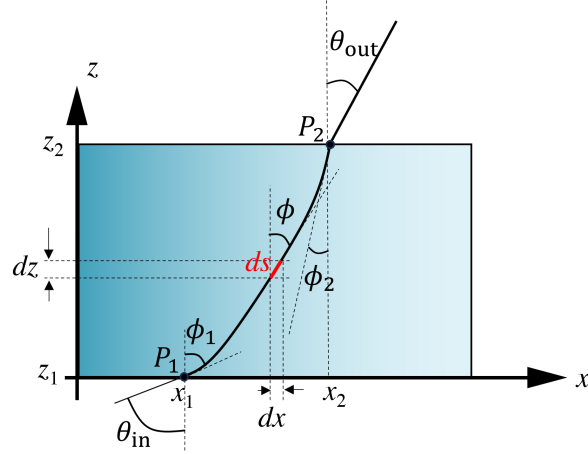


Figure A.1: Optical path inside the lens.

Combining (A.3) and (A.5):

$$n_1^2 \cos^2 \phi_1 = n_1^2 (1 - \sin^2 \phi_1) = \varepsilon_{r1} - n_{\text{in}}^2 \sin^2 \theta_{\text{in}} \quad (\text{A.6a})$$

$$n_2^2 \cos^2 \phi_2 = n_2^2 (1 - \sin^2 \phi_2) = \varepsilon_{r2} - n_{\text{out}}^2 \sin^2 \theta_{\text{out}}. \quad (\text{A.6b})$$

From the trigonometric equations, (A.3) can be written as:

$$n \cos \phi = n \cot \phi \sin \phi = n \frac{\cot \phi}{\sqrt{1 + \cot^2 \phi}}. \quad (\text{A.7})$$

The cotangent of the angle inside the lens can be related with the slope of the path by:

$$\frac{dz}{dx} = \tan \left(\frac{\pi}{2} - \phi \right) = \cot \phi \quad (\text{A.8})$$

Thus,

$$n \frac{\frac{dz}{dx}}{\sqrt{1 + \left(\frac{dz}{dx} \right)^2}} = n_2 \cos \phi_2. \quad (\text{A.9})$$

By applying some algebraic steps, (A.9) can be rewritten as:

$$\frac{dz}{dx} = \frac{n_2 \cos \phi_2}{\sqrt{n^2 - n_2^2 \cos^2 \phi_2}}. \quad (\text{A.10})$$

Substituting (A.6b) and (A.10) into (A.2), we can write

$$\int_{P_1}^{P_2} n ds = \int_{x_1}^{x_2} \frac{n^2}{\sqrt{n^2 - (\varepsilon_{r2} - n_{\text{out}}^2 \sin^2 \theta_{\text{out}})}} dx. \quad (\text{A.11})$$

To close this integral, it is assumed that the relative permittivity changes linearly in the region between x_1 and x_2 with a slope a ($a > 0$):

$$\varepsilon_r - \varepsilon_{r2} = a(x_2 - x) \quad (\text{A.12})$$

where a can be expressed as:

$$a = \frac{\varepsilon_{r1} - \varepsilon_{r2}}{x_2 - x_1}. \quad (\text{A.13})$$

Using (A.6), a can also be expressed as

$$a = \frac{n_{\text{in}}^2 \sin^2 \theta_{\text{in}} - n_{\text{out}}^2 \sin^2 \theta_{\text{out}}}{x_2 - x_1}. \quad (\text{A.14})$$

(A.2) can be closed using commercial mathematics software. The closed-form expression for the integration is:

$$\int_{x_1}^{x_2} n ds = 2 \frac{S_{\text{in}}^3/3 + 2S_{\text{out}}^3/3 + (\varepsilon_{r2} - S_{\text{out}}^2)S_{\text{in}} - \varepsilon_{r2}S_{\text{out}}}{a} \quad (\text{A.15})$$

where $S_{\text{in}} = n_{\text{in}} \sin \theta_{\text{in}}$, $S_{\text{out}} = n_{\text{out}} \sin \theta_{\text{out}}$. Similarly, substituting (A.5a), (A.6a) into (A.2), a dual expression of (A.15) as function of ε_{r1} is obtained:

$$\int_{x_1}^{x_2} n ds = 2 \frac{-2S_{\text{in}}^3/3 - S_{\text{out}}^3/3 + (S_{\text{in}}^2 - \varepsilon_{r1})S_{\text{out}} + \varepsilon_{r1}S_{\text{in}}}{a}. \quad (\text{A.16})$$

The integration contains both a and ε_{r1} or ε_{r2} as unknowns. To solve this, another set of equations is needed. Supposing that the thickness of the GRIN lens is T , then the integration along z -direction is:

$$T = \int_0^T dz = \int_{x_1}^{x_2} \frac{dz}{dx} dx \stackrel{(\text{A.10})}{=} \int_{x_1}^{x_2} \frac{n_2 \cos \phi_2}{\sqrt{n^2 - n_2^2 \cos^2 \phi_2}} dx \quad (\text{A.17})$$

This analytical integral expression can also be closed using commercial mathematics software and gives:

$$T = \frac{2\sqrt{\varepsilon_{r2} - S_{\text{out}}^2}(S_{\text{in}} - S_{\text{out}})}{a}. \quad (\text{A.18})$$

Similarly, if the equations with ε_{r1} are used, the dual expression for (A.18) is obtained:

$$T = \frac{2\sqrt{\varepsilon_{r1} - S_{\text{in}}^2}(S_{\text{in}} - S_{\text{out}})}{a}. \quad (\text{A.19})$$

Combining (A.15) with (A.18) and (A.16) with (A.19), the complete closed-form expression for the optical path inside the lens are found:

$$\int_{P_1}^{P_2} n ds = T \frac{S_{\text{in}}^3/3 + 2S_{\text{out}}^3/3 + (\varepsilon_{r2} - S_{\text{out}}^2)S_{\text{in}} - \varepsilon_{r2}S_{\text{out}}}{\sqrt{\varepsilon_{r2} - S_{\text{out}}^2}(S_{\text{in}} - S_{\text{out}})} \quad (\text{A.20a})$$

$$\int_{P_1}^{P_2} n ds = T \frac{-2S_{\text{in}}^3/3 - S_{\text{out}}^3/3 - (\varepsilon_{r1} - S_{\text{in}}^2)S_{\text{out}} + \varepsilon_{r1}S_{\text{in}}}{\sqrt{\varepsilon_{r1} - S_{\text{in}}^2}(S_{\text{in}} - S_{\text{out}})}. \quad (\text{A.20b})$$

Appendix B

Derivation of the Eikonal Equation

The step-by-step derivations of the Eikonal equation and the ray equation are presented in [28]. Here, another approach is outlined.

B.1 Eikonal Equation from Wave Equation

For a source-free, isotropic, linear, homogeneous region, the wave equation (Helmholtz equation) is given as [54]:

$$(\nabla^2 + \omega^2 \varepsilon \mu) \mathbf{E}(\mathbf{r}) = 0. \quad (\text{B.1})$$

where $\mathbf{E}(\mathbf{r})$ is a scalar field, ω is the angular frequency, \mathbf{r} is the position vector, ε and μ are the permittivity and permeability of the medium. The general solution for this equation can be written as:

$$\mathbf{E}(\mathbf{r}) = E_0(\mathbf{r})e^{-j\bar{\mathbf{k}} \cdot \mathbf{r}} = E_0(\mathbf{r})e^{-jk_0 n(\mathbf{r})\hat{\mathbf{k}} \cdot \mathbf{r}} \quad (\text{B.2})$$

where $\mathbf{k} = k\hat{\mathbf{k}}$ is the wave vector, $\hat{\mathbf{k}}$ is the unit vector along the propagation direction, $E_0(\mathbf{r})$ is the complex vector amplitudes, k_0 is the wavenumber in free-space and n is medium's refractive index which can be written as the root of the production of its relative permittivity ε_r and permeability μ_r : $n = \sqrt{\varepsilon_r \mu_r}$. Defining $S(\mathbf{r}) = n(\mathbf{r})(\hat{\mathbf{k}} \cdot \mathbf{r})$, where $S(\mathbf{r})$ refers to the concept 'eikonal', one can write the general solution as

$$\mathbf{E}(\mathbf{r}) = E_0(\mathbf{r})e^{-jk_0 S(\mathbf{r})}. \quad (\text{B.3})$$

Substituting $\mathbf{E}(\mathbf{r})$ into (B.1):

$$k_0^2 \left(\frac{k^2}{k_0^2} - \nabla S(\mathbf{r}) \cdot \nabla S(\mathbf{r}) \right) E_0(\mathbf{r}) - jk_0 (2\nabla S(\mathbf{r}) \cdot \nabla E_0 + E_0 \nabla^2 S(\mathbf{r})) + \nabla^2 E_0 = 0, \quad (\text{B.4})$$

divided by k_0^2 :

$$\left(\frac{k^2}{k_0^2} - \nabla S(\mathbf{r}) \cdot \nabla S(\mathbf{r}) \right) E_0(\mathbf{r}) - \frac{j}{k_0} (2\nabla S(\mathbf{r}) \cdot \nabla E_0 + E_0 \nabla^2 S(\mathbf{r})) + \frac{\nabla^2 E_0}{k_0^2} = 0. \quad (\text{B.5})$$

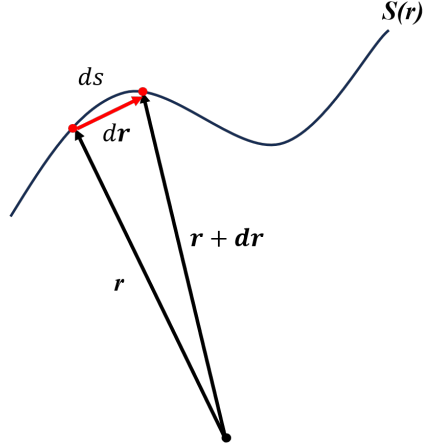


Figure B.1: A small arc on the ray trajectory.

If the GO approximations ($\lambda_0 \rightarrow 0, k_0 \rightarrow \infty$) are applied, the last term of (B.5) vanishes as a high-order small value. To have this equation equals to 0, it is equivalent to have both its real and imaginary part equal to 0. The real part is dependent on $E_0(\mathbf{r})$, which is not 0 all the time. Therefore, it can be derived that:

$$\frac{k^2}{k_0^2} - \nabla S(\mathbf{r}) \cdot \nabla S(\mathbf{r}) = 0 \quad (\text{B.6})$$

$$\Rightarrow (\nabla S(\mathbf{r}))^2 = n^2 \quad (\text{B.7})$$

This expression is called as the scalar Eikonal equation. Noting that here $S(\mathbf{r})$ is a scalar function of \mathbf{r} and $\nabla S(\mathbf{r})$ is a vector, so the square on both side can not be canceled but

$$|\nabla S(\mathbf{r})| = |n| \quad (\text{B.8})$$

is valid. With the Eikonal equation, it is possible to find the ray trace by finding S using Eikonal equation first, then force S to be constant for finding a certain equi-wavefront. The normal vector of the phase front represents the direction of ray propagation.

B.2 Ray Equation from Eikonal Equation

It is possible to derive a function that describe the ray path directly based on Eikonal equation. Considering a small arc section dS on the ray path function $S(\mathbf{r})$ (shown as Fig. B.1), $d\mathbf{r}$ is a vector tangent to dS with length approximately equals to ds . The unit vector $\boldsymbol{\tau}$ is given by:

$$\boldsymbol{\tau} = \frac{d\mathbf{r}}{ds} \quad (\text{B.9})$$

$\boldsymbol{\tau}$ is normal to the equi-phase plane so

$$\boldsymbol{\tau} \parallel \nabla S(\mathbf{r}) \quad (\text{B.10})$$

This vector stands for the direction of ray. Therefore, combining (B.8):

$$\nabla S(\mathbf{r}) = |\nabla S(\mathbf{r})| \boldsymbol{\tau} = n \frac{d\mathbf{r}}{ds} \quad (\text{B.11})$$

The differentiate along s can be written as:

$$\frac{d}{ds} = \sum_i \frac{dx_i}{ds} \frac{\partial}{\partial x_i} = \frac{d\mathbf{r}}{ds} \cdot \nabla \quad (\text{B.12})$$

Taking the derivative on (B.7):

$$2\nabla S(\mathbf{r}) \cdot \nabla \nabla S(\mathbf{r}) = 2n\nabla n \rightarrow (n \frac{d\mathbf{r}}{ds} \cdot \nabla) \nabla S(\mathbf{r}) = n\nabla n \quad (\text{B.13})$$

Substitute (B.11) into (B.13):

$$n \frac{d}{ds} (\nabla S(\mathbf{r})) = n\nabla n \quad (\text{B.14})$$

Combining (B.13) with (B.14) and cancel out the refractive index on both side:

$$\frac{d}{ds} (n \frac{d\mathbf{r}}{ds}) = \nabla n \quad (\text{B.15})$$

The explicit forms for the Eikonal equation ((B.7)) and the ray equation ((B.15)) under the Cartesian coordinate system can be found in [28]. This ordinary differential equation set with six sub-equations and six unknowns (the x, y, z positions and the tangential direction of ray trajectory in $x-, y-, z-$ directions)

Appendix C

Graphic User Interface for GRIN lens design and ray tracing simulation

A graphic user interface (GUI) based on MATLAB is designed applying the equations reported in Chap. 2. The layout of the GUI is shown in Fig. C.1.

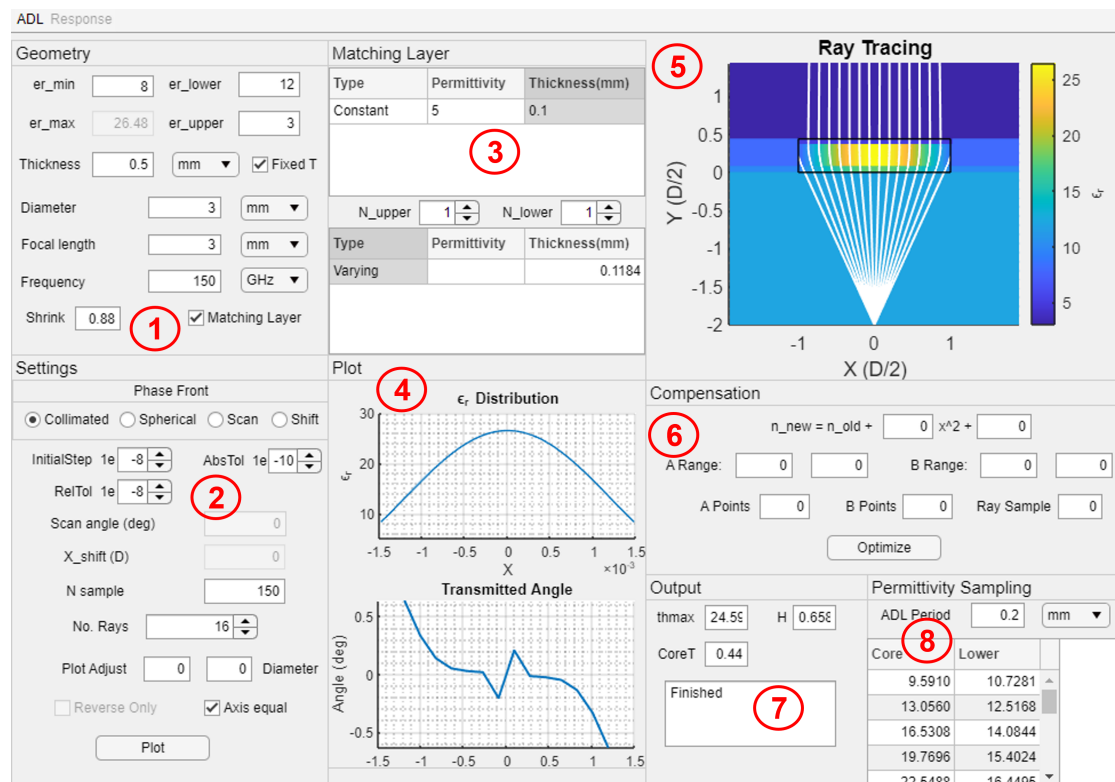


Figure C.1: Layout of the GUI

- 1. Geometry panel** The design parameters for the GRIN lens's core can be spec-

ified in this panel.

- $\epsilon_{r,\min}$ is the minimum relative permittivity of the lens.
 - $\epsilon_{r,\text{in}}$ is the relative permittivity of the medium below the lens.
 - $\epsilon_{r,\max}$ is the maximum relative permittivity of the core. This variable is not editable when **Fixed T** is checked and is calculated automatically.
 - $\epsilon_{r,\text{out}}$ is the relative permittivity of the medium above the lens.
 - **Thickness** is the thickness of the core. This value is editable if **Fixed T** is checked and can be input with the unit mm and μm .
 - **Fixed T** is the check box to enable the design following a fixed thickness.
 - **Diameter** is the diameter of the GRIN lens in either mm or μm .
 - **Focal length** is the focal length of the lens in mm or μm .
 - **Frequency** is the center frequency of the design band. This value is used to calculate the thickness of the quarter wavelength impedance transformer in the **Matching layer panel**. The frequency can be given in Hz, MHz, GHz or THz.
 - **Shrink** is the shrink factor of the core thickness. This is the parameter for optimizing the transmitted phase when the matching layers are introduced.
 - **Matching layer** is the check box to enable the **Matching layer panel**.
2. **Settings panel** In this panel, some basic settings for the GRIN lens design and ray tracing simulations can be made.
- **Phase Front** is where the scenario is chosen.
 - **InitialStep**, **AbsTol**, **RelTol** are the initial step size, absolute error tolerance and the relative error tolerance of the ode solver. More information can be found in **odeset**.
 - **Scan angle** is the scan angle for the GRIN lens under **Scan** mode in degree.
 - X_{shift} is the lateral shift of the feed on the horizontal focal plane. This parameter is normalized to the diameter.
 - **N sample** is the sample points for finding the permittivity profile.
 - **No. Rays** is the number of rays to simulate across the lens.
 - **Plot Adjust** is the extra shift on plot to avoid plotting the ray transmitted through lens' side edges.
 - **Reverse only** is the check box for plotting the reverse lines only for **spherical** mode.
 - **Axis equal** is the check box for plotting with equal axis.
 - **Plot** is the button that takes the data from the geometry panel and the setting panel to perform the ray tracing simulations.

3. **Matching layer panel** The matching layers can be designed if the **Matching Layer** check box is checked. The number of matching layers above (N_{upper}) and below (N_{lower}) the lens can be arbitrarily chosen. For the matching layer closest to the core, i.e. the first upper / lower matching layer can be defined as either **Varying** or **Constant** under **Type**. If the varying matching layer is chosen, its permittivity is given as the production of the adjacent media's refractive index. For other matching layers, only the **Constant** can be chosen and the respective permittivity and thickness of the layer can be given. If the thickness is not specified, or **NaN**, the thickness will be automatically calculated as the quarter wavelength of the slab (for varying layer, the thickness follows the quarter wavelength of the center permittivity).
4. **Plot panel** This panel is consisted of two plots. The first plot is the relative permittivity distribution versus the radial distance. The other plot is the transmitted angle in the upper medium w.r.t. the radial distance.
5. **Ray tracing panel** The ray paths and the color map for permittivity distribution are plotted on this panel.
6. **Compensation panel** This panel is designed to compensate the phase variation due to the matching layer. An extra quadratic phase can be added to the original refractive index n_{old} . The range of the second order parameters can be defined in **A Range** while the zeroth order parameter of the compensation is specified in **B Range**. The sample points for these ranges can be input in **A Points** and **B Points**. The optimization process aims to minimize the cost function, which is defined as:
$$\text{Cost} = \sum_{i=1}^N |\theta_{i,\text{out}} - \theta_{\text{scan}}|, \quad (\text{C.1})$$

where $\theta_{i,\text{out}}$ is the transmitted angle of the i -th ray and N is the number of sampled rays specified in **Ray Sample**.
7. **Output panel** The maximum incident angle θ_{max} , the total thickness of the lens H and the thickness of the core CoreT are calculated and output in this panel.
8. **Permittivity sampling panel** To have a look of the permittivity at the center of each unit cell, the permittivity for the core and varying matching layers, with an extra input **ADL Period**. Noting that the permittivity is sampled from $-D/2 + p/2$ to $D/2 - p/2$.

Bibliography

- [1] J. B. Pendry, D. Schurig, and D. R. Smith, “Controlling electromagnetic fields,” *Science*, vol. 312, no. 5781, pp. 1780–1782, 2006.
- [2] R. Luneburg, *Mathematical Theory of Optics*. University of California Press, 2021.
- [3] G. Liu, M. R. Dehghani Kodnoeih, K. T. Pham, E. M. Cruz, D. González-Ovejero, and R. Sauleau, “A millimeter-wave multibeam transparent transmitarray antenna at ka-band,” *IEEE Antennas and Wireless Propagation Letters*, vol. 18, no. 4, pp. 631–635, 2019.
- [4] M. Jiang, Z. N. Chen, Y. Zhang, W. Hong, and X. Xuan, “Metamaterial-based thin planar lens antenna for spatial beamforming and multibeam massive mimo,” *IEEE Transactions on Antennas and Propagation*, vol. 65, no. 2, pp. 464–472, 2017.
- [5] A. Jouade, M. Himdi, and O. Lafond, “Fresnel lens at millimeter-wave: Enhancement of efficiency and radiation frequency bandwidth,” *IEEE Transactions on Antennas and Propagation*, vol. 65, no. 11, pp. 5776–5786, 2017.
- [6] A. Paraskevopoulos, F. Maggiorcelli, M. Albani, and S. Maci, “Radial grin lenses based on the solution of a regularized ray congruence equation,” *IEEE Transactions on Antennas and Propagation*, vol. 70, no. 2, pp. 888–899, 2022.
- [7] N. C. Garcia and J. D. Chisum, “High-efficiency, wideband grin lenses with intrinsically matched unit cells,” *IEEE Transactions on Antennas and Propagation*, vol. 68, no. 8, pp. 5965–5977, 2020.
- [8] F. Maggiorcelli, A. Paraskevopoulos, J. C. Vardaxoglou, M. Albani, and S. Maci, “Profile inversion and closed form formulation of compact grin lenses,” *IEEE Open Journal of Antennas and Propagation*, vol. 2, pp. 315–325, 2021.
- [9] S. S. D. Jones and J. Brown, “Metallic delay lenses,” *Nature*, vol. 163, pp. 324–325, Feb 1949.
- [10] M. Li and N. Behdad, “Wideband true-time-delay microwave lenses based on metallo-dielectric and all-dielectric lowpass frequency selective surfaces,” *IEEE Transactions on Antennas and Propagation*, vol. 61, no. 8, pp. 4109–4119, 2013.

- [11] J. B. Pendry, A. Aubry, D. R. Smith, and S. A. Maier, “Transformation optics and subwavelength control of light,” *Science*, vol. 337, no. 6094, pp. 549–552, 2012.
- [12] H. Chen, C. Chan, and P. Sheng, “Transformation optics and metamaterials,” *Nature materials*, vol. 9, pp. 387–96, 05 2010.
- [13] F. Sun, B. Zheng, H. Chen, W. Jiang, S. Guo, Y. Liu, Y. Ma, and S. He, “Transformation optics: From classic theory and applications to its new branches,” *Laser & Photonics Reviews*, vol. 11, no. 6, p. 1700034, 2017.
- [14] S. Jain, M. Abdel-Mageed, and R. Mittra, “Flat-lens design using field transformation and its comparison with those based on transformation optics and ray optics,” *IEEE Antennas and Wireless Propagation Letters*, vol. 12, pp. 777–780, 2013.
- [15] S. Zhang, R. K. Arya, W. G. Whittow, D. Cadman, R. Mittra, and J. C. Vardaxoglou, “Ultra-wideband flat metamaterial grin lenses assisted with additive manufacturing technique,” *IEEE Transactions on Antennas and Propagation*, vol. 69, no. 7, pp. 3788–3799, 2021.
- [16] W. E. Kock, “Metallic delay lenses,” *The Bell System Technical Journal*, vol. 27, no. 1, pp. 58–82, 1948.
- [17] D. Cavallo, W. H. Syed, and A. Neto, “Closed-form analysis of artificial dielectric layers—part i: Properties of a single layer under plane-wave incidence,” *IEEE Transactions on Antennas and Propagation*, vol. 62, no. 12, pp. 6256–6264, 2014.
- [18] D. Cavallo, W. Syed, and A. Neto, “Closed-form analysis of artificial dielectric layers—part ii: Extension to multiple layers and arbitrary illumination,” *Antennas and Propagation, IEEE Transactions on*, vol. 62, pp. 6265–6273, 12 2014.
- [19] D. Cavallo and C. Felita, “Analytical formulas for artificial dielectrics with non-aligned layers,” *IEEE Transactions on Antennas and Propagation*, vol. 65, no. 10, pp. 5303–5311, 2017.
- [20] D. Cavallo and R. M. van Schelven, “Closed-form analysis of artificial dielectric layers with non-periodic characteristics,” in *2019 13th European Conference on Antennas and Propagation (EuCAP)*, pp. 1–5, 2019.
- [21] W. Syed, *On the Control of Surface Waves in Integrated Antennas: Analysis and Design Exploiting Artificial Dielectric Layers*. PhD thesis, Delft University of Technology, 2015.
- [22] Y. Su and Z. N. Chen, “A flat dual-polarized transformation-optics beams scanning luneburg lens antenna using pcb-stacked gradient index metamaterials,” *IEEE Transactions on Antennas and Propagation*, vol. 66, no. 10, pp. 5088–5097, 2018.
- [23] C. Mateo-Segura, A. Dyke, H. Dyke, S. Haq, and Y. Hao, “Flat luneburg lens via transformation optics for directive antenna applications,” *IEEE Transactions on Antennas and Propagation*, vol. 62, no. 4, pp. 1945–1953, 2014.

- [24] Q.-W. Lin, Y.-S. To, and H. Wong, “A dual-polarized lens antenna using gradient refractive index (grin) metasurface,” in *2020 IEEE Asia-Pacific Microwave Conference (APMC)*, pp. 1063–1065, 2020.
- [25] S. M. A. M. H. Abadi and N. Behdad, “Design of wideband, fss-based multibeam antennas using the effective medium approach,” *IEEE Transactions on Antennas and Propagation*, vol. 62, no. 11, pp. 5557–5564, 2014.
- [26] E. Erfani, M. Niroom-Jazi, and S. Tatu, “A high-gain broadband gradient refractive index metasurface lens antenna,” *IEEE Transactions on Antennas and Propagation*, vol. 64, no. 5, pp. 1968–1973, 2016.
- [27] B. Bleaney and B. Bleaney, *Electricity and Magnetism, Volume 1: Third Edition*. Electricity and Magnetism, OUP Oxford, 2013.
- [28] C. Coco Martin, “Wideband flat lenses based on artificial dielectric layers,” 2022.
- [29] H. D. Hristov and J. M. Rodriguez, “Design equation for multidielectric fresnel zone plate lens,” *IEEE Microwave and Wireless Components Letters*, vol. 22, no. 11, pp. 574–576, 2012.
- [30] A. Jouadé, J. Bor, O. Lafond, and M. Himdi, “Millimeter-wave fresnel zone plate lens based on foam gradient index technological process,” in *2016 10th European Conference on Antennas and Propagation (EuCAP)*, pp. 1–4, 2016.
- [31] R. Corporation, “Ro4000[®] laminates ro4003c and ro4350b - data sheet.” <https://www.rogerscorp.com/advanced-electronics-solutions/ro4000-series-laminates/ro4003c-laminates>.
- [32] N. Kundtz and D. Smith, “Extreme-angle broadband metamaterial lens,” *Nature materials*, vol. 9, pp. 129–32, 12 2009.
- [33] X. Chen, L. Huang, H. Mühlenbernd, G. Li, B. Bai, Q. Tan, G. Jin, C.-W. Qiu, S. Zhang, and T. Zentgraf, “Dual-polarity plasmonic metalens for visible light,” *Nature communications*, vol. 3, p. 1198, 11 2012.
- [34] S. Zhang, Y. Vardaxoglou, W. Whittow, and R. Mittra, “3d-printed graded index lens for rf applications,” in *2016 International Symposium on Antennas and Propagation (ISAP)*, pp. 90–91, 2016.
- [35] K. Karkkainen, A. Sihvola, and K. Nikoskinen, “Effective permittivity of mixtures: numerical validation by the fdtd method,” *IEEE Transactions on Geoscience and Remote Sensing*, vol. 38, no. 3, pp. 1303–1308, 2000.
- [36] A. Sihvola, “Self-consistency aspects of dielectric mixing theories,” *IEEE Transactions on Geoscience and Remote Sensing*, vol. 27, no. 4, pp. 403–415, 1989.

- [37] H. Karimian-Sarakhs and M. H. Neshati, “Comparative analysis of the effective permittivity of aligned cylindrical perforated substrate,” in *2020 28th Iranian Conference on Electrical Engineering (ICEE)*, pp. 1–4, 2020.
- [38] A. Sihvola and J. Kong, “Effective permittivity of dielectric mixtures,” *IEEE Transactions on Geoscience and Remote Sensing*, vol. 26, no. 4, pp. 420–429, 1988.
- [39] C. Kittel and P. McEuen, *Introduction to Solid State Physics*. Wiley, 2018.
- [40] M. Mrnka and Z. Raida, “An effective permittivity tensor of cylindrically perforated dielectrics,” *IEEE Antennas and Wireless Propagation Letters*, vol. 17, no. 1, pp. 66–69, 2018.
- [41] R. Corporation, “Ro4450f[®] and ro4460g2[®] bondply - data sheet.” <https://www.rogerscorp.com/advanced-electronics-solutions/ro4000-series-laminates/ro4400-series-bondply>.
- [42] J. Ruze, “Lateral-feed displacement in a paraboloid,” *IEEE Transactions on Antennas and Propagation*, vol. 13, no. 5, pp. 660–665, 1965.
- [43] L. Baggen, C. Jeronimus, and M. Herben, “The scan performance of the fresnel-zone plate antenna: A comparison with the parabolic reflector antenna,” *Microwave and Optical Technology Letters*, vol. 6, pp. 769–774, jan 1993.
- [44] C. A. Balanis, *Antenna theory: analysis and design*. Wiley-Interscience, 2005.
- [45] D. Cavallo and A. Neto, “A connected array of slots supporting broadband leaky waves,” *IEEE Transactions on Antennas and Propagation*, vol. 61, no. 4, pp. 1986–1994, 2013.
- [46] N. v. Rooijen, M. A. delPino, M. Spirito, and N. Llombart, “Core-shell leaky-wave lens antenna for 150ghz fly’s eye communication systems,” in *2022 47th International Conference on Infrared, Millimeter and Terahertz Waves (IRMMW-THz)*, pp. 1–2, 2022.
- [47] H. Zhang, S. O. Dabironezare, G. Carluccio, A. Neto, and N. Llombart, “A go/fo tool for analyzing quasi-optical systems in reception,” in *2019 44th International Conference on Infrared, Millimeter, and Terahertz Waves (IRMMW-THz)*, pp. 1–2, 2019.
- [48] I. Wolff, “Design and technology of microwave and millimeterwave ltcc circuits and systems,” in *2007 International Symposium on Signals, Systems and Electronics*, pp. 505–512, 2007.
- [49] “Dupont[™] greentape[™] 951 product selector guide.” <https://www.dupont.com/content/dam/dupont/amer/us/en/mobility/public/documents/en/GreenTape-951-Product-Selector-Guide.pdf>.

- [50] S. Manshari, S. Koziel, and L. Leifsson, “A wideband corrugated ridged horn antenna with enhanced gain and stable phase center for x- and ku-band applications,” *IEEE Antennas and Wireless Propagation Letters*, vol. 18, no. 5, pp. 1031–1035, 2019.
- [51] M. Ignatenko, B. Simakauskas, M. Notaros, and D. S. Filipovic, “A phase center-stabilized k/ka/v-band linearly polarized horn for luneburg lenses,” *IEEE Antennas and Wireless Propagation Letters*, vol. 16, pp. 2726–2729, 2017.
- [52] O. Yurduseven, D. Cavallo, and A. Neto, “Wideband dielectric lens antenna with stable radiation patterns fed by coherent array of connected leaky slots,” *IEEE Transactions on Antennas and Propagation*, vol. 62, no. 4, pp. 1895–1902, 2014.
- [53] M. Alonso-delPino, N. van Rooijen, S. Bosma, and N. Llombart, “A wideband corrugated leaky-wave feed with low cross-pol for high efficiency lens illumination,” in *15th European Conference on Antennas and Propagation (EuCAP)*, (Düsseldorf, Germany), Mar. 22-26 2021.
- [54] D. Pozar, *Microwave Engineering, 4th Edition*. Wiley, 2011.